Uncertainty evaluation of semi-active load redistribution in a mechanical load-bearing structure

vom Fachbereich Maschinenbau
der Technischen Universität Darmstadt

zur Erlangung des Grades
Doktor-Ingenieur (Dr.-Ing.)

Dissertation
von Christopher Maximilian Gehb

Erstgutachter:	Prof. Dr.-Ing. Tobias Melz
Zweitgutachter:	Prof. Dr.-Ing. Eckhard Kirchner

Darmstadt 2019

Gehb, Christopher Maximilian:
Uncertainty evaluation of semi-active load redistribution in a mechanical load-bearing structure

Bewertung der Unsicherheit von semi-aktiver Lastumverteilung in einer mechanischen lasttragenden Struktur

Darmstadt, Technische Universität Darmstadt,
Jahr der Veröffentlichung der Dissertation auf TUprints: 2019
Tag der mündlichen Prüfung: 09.07.2019

It's so easy to condemn,
so hard to create!

H. J. SIMPSON

Vorwort

Die vorliegende Arbeit entstand während meiner Tätigkeit als wissenschaftlicher Mitarbeiter am Fachgebiet Systemzuverlässigkeit, Adaptronik und Maschinenakustik SAM an der Technischen Universität Darmstadt und am Fraunhofer-Institut für Betriebsfestigkeit und Systemzuverlässigkeit LBF. Der Deutschen Forschungsgemeinschaft (DFG) danke ich für die finanzielle Förderung meiner Arbeit im Rahmen des Sonderforschungsbereichs (SFB) 805 „Beherrschung von Unsicherheit in lasttragenden Systemen des Maschinenbaus“.

Mein herzlicher Dank gilt meinem Doktorvater, Herrn Prof. Tobias Melz, für die Ermöglichung und Betreuung dieser Arbeit sowie das mir entgegengebrachte Vertauen. Herrn Prof. Eckhard Kirchner, Leiter des Fachgebiets Produktentwicklung und Maschinenelemente pmd, danke ich für die freundliche Übernahme des Korreferats und das Interesse an meiner Forschungsarbeit. Ein großer Dank gilt Herrn Dr.-Ing. Roland Platz für die intensiven fachlichen Gespräche sowie seine wertvollen Anregungen und Ratschläge zu meiner Arbeit.

Zudem danke ich meinen Kollegen im SFB 805 und am Fraunhofer LBF für die auf fachlicher und persönlicher Ebene ausgezeichnete Zusammenarbeit. Insbesondere gilt dieser Dank meinen Freunden und Kollegen Dr.-Ing. Maximilian Schäffner und Dr.-Ing. Benedict Götz für die unzähligen fachlichen Diskussionen und die vielen gemeinsamen Erlebnisse, an die ich mich gerne erinnere. Auch bei meinen Studenten und Hilfswissenschaftlern, die meine Forschung mit großer Motivation und Tatkraft unterstützt haben, möchte ich mich bedanken.

Meiner Familie und meinen Freunden danke ich für ihre Ermutigungen, Ablenkung und Treue in fordernden Zeiten. Ohne meinen Vater Dieter, meiner viel zu früh von uns gegangenen Mutter Christa und meiner Schwester Magdalena wäre ich nicht da, wo ich heute bin. Mein ganz besonderer Dank gilt meiner lieben Kathrin für ihre unerschöpfliche Geduld sowie die liebevolle und beständige Unterstützung in allen Lebenslagen, ohne die diese Arbeit sonst nicht möglich gewesen wäre. Schließlich danke ich meiner wundervollen Tochter Elenora Luise für eine Horizonterweiterung, die ich nicht für möglich gehalten hätte.

Darmstadt, im Dezember 2019 Christopher Gehb

Abstract

Load-bearing structures in mechanical engineering applications typically face the challenge of withstanding and transmitting external loads. In most cases, the load path through the load-bearing structure is predetermined by the design. However, if parts of the load-bearing structure become weak or suffer damage, e.g. due to deterioration or overload, the load capacity becomes uncertain. In this thesis, the semi-active load redistribution to bypass a portion of the loading away from damaged parts of the structure is used in order to prevent the structure from failure or malfunction. So far, studies on semi-active or active measures to adapt or manipulate the dynamic behavior of a structure have primarily investigated damping or vibration control and not load redistribution. The proposed semi-active load redistribution provides a technological possibility to influence the load path during operation via augmenting already existing parts of the load-bearing structure with actuators. Furthermore, for accurate numerical predictions of the load redistribution capability, an adequate mathematical model is needed. Therefore, the accuracy of the load-bearing structure's mathematical model predictions is evaluated and increased methodologically by model parameter uncertainty quantification and reduction.

The structure to numerically and experimentally investigate load redistribution in this thesis is based on a load-bearing structure developed within the SFB 805 and consists of a translational moving mass connected to a beam by a spring-damper system and two newly developed semi-active augmented guidance elements for load redistribution. The beam is supported at its ends by two supports. The stiffness characteristic of the supports can be adjusted to simulate structural damage. The structural damage, in turn, causes misalignment of the beam, which is defined as malfunction. A mathematical model of the load-bearing structure is derived for numerical investigations of the load redistribution capability and for controller design. A BAYESIAN inference based calibration procedure is applied to reduce and simultaneously quantify the model parameter uncertainty. Thus, the model is adjusted to the present conditions and the model prediction accuracy is increased. Clipped-optimal LQR and PID controllers are introduced for the semi-active load redistribution and designed based on the calibrated model.

With the presented procedure, the model prediction variation due to parameter uncertainty is reduced by up to 85%. Comparing the passive and semi-active

load-bearing structure, the malfunction is reduced by up to 53% numerically and by up to 51% experimentally. The evaluation of the load paths shows that a redistribution of the load between the two supports is achieved by means of the semi-active guidance elements. The results of this thesis contribute to the methodological parameter uncertainty quantification and reduction as well as the technological application of semi-active load redistribution.

Kurzfassung

Lasttragende Strukturen im Maschinenbau stehen typischerweise vor der Herausforderung, äußeren Belastungen standzuhalten und diese über einen Lastpfad zu übertragen. In den meisten Fällen ist der Lastpfad durch die lasttragende Struktur konstruktionsbedingt vorgegeben. Wenn jedoch Teile der lasttragenden Struktur geschwächt oder geschädigt werden, z. B. aufgrund von Verschleiß oder Überlastung, wird ihre Tragfähigkeit unsicher. In dieser Arbeit wird die semi-aktive Lastumverteilung verwendet, um einen Teil der Last um geschädigte Teile der Struktur herumzuleiten und so ein Versagen oder eine Fehlfunktion der Struktur zu verhindern. Bisherige Studien zu semi-aktiven oder aktiven Maßnahmen zur Anpassung oder Beeinflussung des dynamischen Verhaltens einer Struktur untersuchten hauptsächlich die Regelung von Dämpfungseigenschaften oder die Schwingungskontrolle und adressierten nicht die Lastumverteilung. Die vorgeschlagene semi-aktive Last-umverteilung bietet eine technologische Möglichkeit, den Lastpfad während des Betriebs anzupassen indem bereits vorhandene Teile der lasttragenden Struktur mit Aktuatoren erweitert werden. Darüber hinaus ist für genaue numerische Vorhersagen des Lastumverteilungsvermögens ein geeignetes mathematisches Modell erforderlich. Dafür wird die Genauigkeit der Vorhersage des abgeleiteten mathematischen Modells bewertet und methodisch durch die Quantifizierung und Reduktion der Parameterunsicherheit erhöht.

Die Struktur zur numerischen und experimentellen Untersuchung der Lastumverteilung in dieser Arbeit basiert auf einer im SFB 805 entwickelten lasttragenden Struktur und besteht aus einer translatorisch beweglichen Masse, die über ein Feder-Dämpfer-System mit einem Balken verbunden ist, und zwei neuentwickelte, semi-aktive Gelenkmodule für die Lastumverteilung. Der Balken ist beidseitig näherungsweise gelenkig gelagert. Die Steifigkeitscharakteristik der Lager kann angepasst werden, um strukturelle Schäden zu simulieren. Die strukturelle Beschädigung verursacht wiederum eine Schrägstellung des Balkens, die als Fehlfunktion definiert wird. Für numerische Untersuchungen des Lastumverteilungsvermögens und des Reglerentwurfs wird ein mathematisches Modell der lasttragenden Struktur gebildet. Ein auf Bayes'scher Statistik basierendes Kalibrierungsverfahren wird angewendet, um die Modellparameterunsicherheit zu verringern und gleichzeitig zu quantifizieren. Dadurch wird das Modell an die gegenwärtigen Bedingungen angepasst und die Modellvorhersage-genauigkeit erhöht.

Auf Basis des kalibrierten Modells werden für die Lastumverteilung ein clipped-optimal LQR- und ein PID-Regler entworfen.

Mit dem vorgeschlagenen Verfahren wird die Variation der Modellvorhersage aufgrund von Parameterunsicherheit um bis zu 85 % reduziert. Im Vergleich der passiven und semi-aktiven lasttragenden Struktur lässt sich die definierte Fehlfunktion numerisch um bis zu 53 % und experimentell um bis zu 51 % reduzieren. Die Auswertung der Lastpfade über die Lagerkräfte zeigt, dass mittels der semi-aktiven Gelenkmodule eine Umverteilung der Last zwischen den beiden Lagern erreicht wird. Zusammenfassend tragen die Ergebnisse dieser Arbeit zur methodischen Quantifizierung und Reduktion der Parameterunsicherheit sowie zur technologischen Anwendung der Lastumverteilung bei.

Contents

1 Introduction

Commonly, the load path in load-bearing structures is predetermined in the design phase according to required specifications. In case of customary passive load-bearing structures, the load path is typically not subjected to any intentional changes during operational usage. Uncertainty, e.g. due to manufacturing tolerances and aging may lead to unbalanced or inappropriate loads in the supports or other parts of the load-bearing structure. Malfunction or damages can be the consequence. The semi-active load redistribution approach proposed in this thesis provides a technological possibility to influence the load path during operation and to mitigate the effects of uncertainty on the dynamic behavior of load-bearing structures. Furthermore, uncertainty related to the need of more complex mathematical models to credibly predict system behavior is addressed methodologically by model parameter uncertainty quantification and reduction. In this thesis, an exemplary load-bearing structure with defined kinematic behavior, such as an airplane landing gear, is investigated and its load redistribution capability to relieve damaged structural components is evaluated. For that, guidance elements, as kinematic parts of the load-bearing structure, are augmented with electromagnetic actuators that operate as friction brakes. The controlled semi-active moments induced by the friction brakes generate an alternative load path within the load-bearing structure in order to redistribute the load and adapt to the load-bearing structure's current health conditions represented by the supports stiffness. A numerical quantification and reduction of parameter uncertainty is performed to increase the model prediction accuracy. This is done to numerically compare and evaluate the passive and semi-active load-bearing structure regarding load redistribution capability. Finally, the numerical results are validated with experimental data.

1.1 Research motivation

In mechanical engineering applications, transmitting and withstanding loads are often key objectives of mechanical structures. In most cases, the load is transmitted through structural components via a load path that is predetermined by design. Additionally and if moving components are involved, defined kinematics are often an important part of the functional performance in the load-bearing structure

with a specified trajectory of structural components. An example for a load-bearing structure with defined kinematics is a landing gear or suspension strut in airplanes or vehicles. An airplane landing gear mainly consists of spring-damper suspension, torque links and supports at the fuselage, figure 1.1. The spring-damper suspension determines the main kinetic properties, such as impact forces and damping. The desired compression stroke trajectory is enabled by kinematic guidance elements, such as torque links or other suspension links, that connect two or more parts of a load-bearing structure and block non-essential degrees of freedom. The amount of load that is distributed to the structural components is predetermined by the design and, mostly, is not subject to any intentional changes during the structure's lifetime. However, if system properties, e.g. damping and stiffness of the components, are uncertain or vary over time, load path redistribution to bypass a portion of the load away from potentially weakened structural components with reduced stiffness is an option to prevent the structure from failure or reduced comfort. Uncertainty, e.g. due to manufacturing tolerances, aging or overloads, may result in weakened structural components with reduced stiffness. Accordingly, it may be useful to change the load path and redistribute the load towards the stronger structural components with appropriate stiffness.

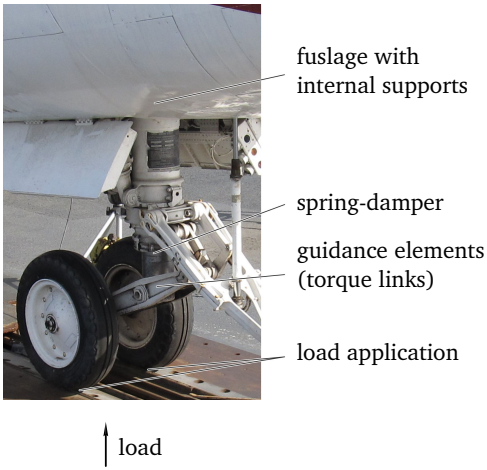

Figure 1.1: An airplane landing gear as an example of load-bearing structures with applied load due to a landing impact

In the research framework of the Collaborative Research Center (German acronym SFB) 805 "Control of Uncertainty in Load-Carrying Structures in Mechanical Engineering" at the Technische Universität Darmstadt, a truss structure with

defined kinematics, comparable to an aircraft landing gear, is represented by the Modular Active Spring Damper System (German acronym MAFDS) in figure 1.2.

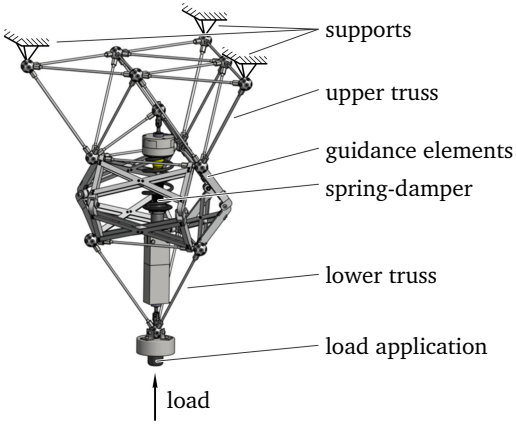

Figure 1.2: Modular Active Spring Damper System (MAFDS) developed at the SFB 805, [33], as an example of load-bearing structures with applied load due to a drop test impact

The MAFDS mainly consists of the upper and lower truss structure, the spring-damper suspension system, and kinematic guidance elements. The upper truss is used to transfer and distribute the loads into the three supports. The spring-damper system mainly defines the dynamic behavior of the MAFDS. The kinematic guidance elements are necessary to realize a defined compression stroke trajectory between the upper and lower truss and to bear lateral loads if necessary, [44]. Loads can be applied statically by adding weights onto the upper truss or dynamically by performing drop tests. The research program of the SFB 805 focuses on a holistic approach to control uncertainty along the product life stages: from product development to production to usage. In this context, the SFB-Demonstrator serves as a platform within the SFB 805 to test the developed methods and technologies for reducing or compensating uncertainty on real load-bearing systems to increase the stability, attenuate vibrations and redistribute loads, see section 3.1 and [33, 47, 75, 101]. Depending on the load case and structural health conditions, such as reduced support stiffness, inappropriate load distribution may occur and the need for in-operation load redistribution to change the predetermined load path arises. This is also known as Structural Health Control (SHC), [81].

SHC combines structural health monitoring, assessing the structural condition and an adequate intervention to load or relieve load-bearing components. Load redistribution, as proposed in this thesis, can be used specifically to load or relieve supports of a load-bearing structure according to their state of health represented by the support stiffness, whereas decreasing stiffness indicates deterioration or nascent damage.

Conventionally, an optimal design for the load path in a structural dynamic system, such as a truss with known loading conditions, is achieved by optimizing the parameters of the system. Typical optimization parameters are specific material and geometric properties, e.g. Young's modulus, cross-sectional areas of truss members and the topology of trusses, [12, 34]. Optimizing trusses with respect to damage tolerance leads to truss structures that are resistant to collapse despite suffering initial damage, [77]. These approaches improve the dynamic structural behavior by utilizing design measures and are based mainly on passive solutions without any additional energy that is fed into the structure for adaptive purposes. When additional external energy is introduced into a structure, e.g. via force generating actuators that stabilize equilibrium conditions or attenuate vibrations, a structure becomes semi-active or active. The required energy for the actuators and the system complexity typically increase from semi-active to active, compare section 2.1 for a more detailed classification of passive, semi-active of active approaches. In general, semi-active and active approaches augment the possibilities of structure manipulation since they can change or adapt structure properties during operation, e.g. by providing additional forces. Mostly, the aim is to enhance the load capacity, [31, 69, 102, 109], or to manipulate the dynamic behavior of a system via vibration or damping control to increase the comfort and safety, [22, 39, 112]. The possibility of load redistribution during operation with semi-active measures as a part of SHC is not considered so far.

When using semi-active or active approaches and an appropriate control for structure manipulation, the demands regarding reduction of model prediction uncertainty increase since model predictions are used for controller tuning and system design, [56, 108]. Uncertainty quantification and uncertainty reduction in model predictions contribute to the achievement of reliable and adequate model predictions. Reducing the model prediction uncertainty is achieved i.a. via calibrating model parameters, [50, 72, 83, 113]. Thus, the mathematical model is adjusted to the experimentally observed dynamic behavior. The model prediction uncertainty, however, needs to be quantified to assess the model accuracy, [7, 50, 63, 106]. The uncertainty quantification can be achieved via forward propagation and inverse assessment of the uncertainty, see section 2.2.2. To the author's knowledge, parameter uncertainty quantification and reduction for the model of a load-bearing

structure with semi-active guidance elements for load redistribution is not investigated so far.

1.2 Research objectives and contributions

The findings of the previous section emphasize two fields of research requirements: firstly, using semi-active technology in form of friction brakes in guidance elements for load redistribution and, secondly, quantifying and reducing the uncertainty of model predictions for the numerical model of the semi-active approach. In the context of this thesis, the semi-active load redistribution in a load-bearing structure is investigated numerically and experimentally and parameter uncertainty quantification and reduction is performed using statistical calibration measures.

The exemplary load-bearing structure consists of a translational moving mass connected to a rigid beam by a spring and two kinematic guidance elements. Two supports at the ends of the beam are equipped with adjustable stiffnesses to simulate weakened structural components, figure 1.3. The semi-active load redistribution can be used to relieve the weak structural components. A weakened or damaged structural component is assumed to be one of the two supports and is represented by a reduced support stiffness and, hence, reduced load capacity.

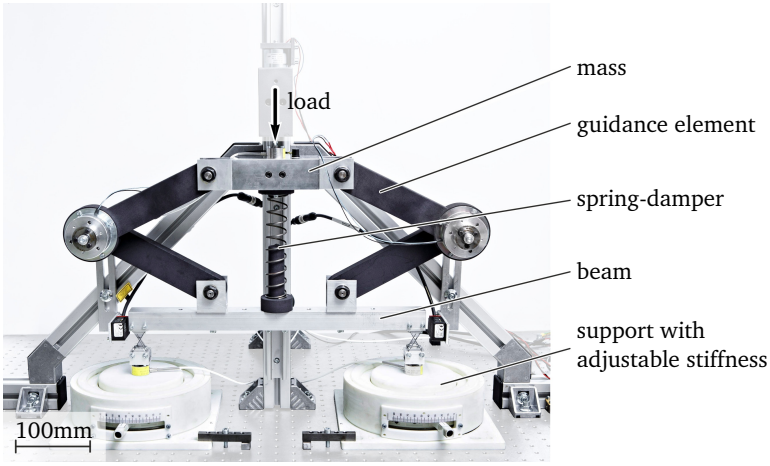

Figure 1.3: Exemplary load-bearing structure with semi-active guidance elements for load redistribution and adjustable supports to simulate weak or damaged support conditions

Varying support stiffnesses represent weakness or damage and, hence, uncertainty in the structural health conditions. The uncertainty may result in inappropriate load paths with possibly exceeded load-bearing capability for the actual load conditions. This manifestation of uncertainty is counteracted by the semi-active load redistribution. Therefore, controllable joints with electromagnetic friction brakes in the kinematic guidance elements are used to provide alternative load paths through the kinematic guidance elements. In case of a weak support, the basic idea is to redistribute loads that normally go through the spring to an alternative path through the kinematic guidance elements to unload the weak support while shifting load to the undamaged support. A controller is implemented to operate the friction brakes and to redistribute the loads within the structure. The capability of the semi-active load path redistribution is demonstrated by an experimental test-setup and via numerical model prediction. Since numerical model prediction results and experimental results do not necessarily and automatically match, the numerical model has to be calibrated adequately to predict the dynamic behavior as well as the remaining prediction uncertainty. In particular, simplifications in damping behavior, simplified physics and friction models constitute an important part of model and parameter uncertainty.

The main research objectives of this thesis consequently result in:

- Design and realization of a semi-active load redistribution control to adapt the load path of a load-bearing structure to the structure's actual health conditions as part of SHC by joints with electromagnetic friction brakes in the kinematic guidance elements – **technological solution**.
- Uncertainty quantification and reduction for model parameters of the load-bearing structure's mathematical model to achieve an adequate prediction accuracy and to obtain the associated uncertainty intervals to evaluate the model fidelity – **methodological solution**.

1.3 Content and outline

The outline of this thesis resembles the two main research objectives that are, on the one hand, to technologically reduce uncertainty with semi-active guidance elements as part of SHC and, on the other hand, to methodologically increase the fidelity of the model predictions regarding the load redistribution capability by uncertainty quantification and parameter calibration. The underlaying research motivation and objectives are presented in **Chapter 1**.

Chapter 2 provides the engineering background and state of research for passive, semi-active and active systems related to load redistribution. Furthermore, a classification of uncertainty for the context of this thesis is given and approaches for uncertainty quantification and reduction in model predictions are presented.

Chapter 3 introduces the investigated load-bearing structure and describes the inherited properties from the SFB Demonstrator. Afterwards, the basic concept of load redistribution is presented. Moreover, the dynamic model of the investigated load-bearing structure is derived for numerical analysis of the load redistribution behavior. For that, the load-bearing structure is first divided into sub-models and finally reassemble to a state space model.

Chapter 4 presents the experimental setup of the investigated load-bearing structure with semi-active guidance elements. The experimental setup is used to measure the load-bearing structure's dynamic behavior with and without semi-active guidance elements in order to experimentally evaluate the load redistribution capability.

Chapter 5 presents the statistical calibration procedure and shows the calibration of the load-bearing structure's mathematical model derived in chapter 3. The calibration is divided into two parts, one for the parameters related to the load-bearing structure itself and one for parameters related to the chosen LuGre-friction model. The resulting calibrated models are used for the controller tuning in chapter 6 and for load redistribution predictions incorporating the quantified parameter uncertainty in chapter 7.

Chapter 6 introduces the proposed load redistribution control strategies. It is distinguished between the reduction of misalignment in the load-bearing structure and the achievement of a defined load ration between the two supports of the load-bearing structure. Therefore, clipped-optimal LQR and PID controllers are tuned and their implementation for the experimental test setup is described.

Chapter 7 presents the numerical and experimental results of the semi-active load redistribution in the load-bearing structure introduced in chapters 3 and 4. The load redistribution capability is analyzed by means of a case study. Additionally, the numerical and experimental results are compared and the model prediction accuracy is evaluated.

Chapter 8 finally summarizes the results of this thesis and provides an outlook on future research objectives.

2 Background and state of research

Load-bearing structures like an airplane landing gear are designed to transmit loads, e.g. caused by impacts, static and dynamic payload, disturbing forces etc., along a predetermined load path. However, damage and unforeseen events such as overloads, can lead to an inappropriate load path, malfunction or even collapse of the load-bearing structure. Concurrently, increasing demands for reliable and efficient performance of mechanical engineering systems like load-bearing structures justify the need of optimized passive systems and the application of semi-active or active approaches for adaptive measures, such as load redistribution for SHC, [58, 81]. Furthermore, the quantification and reduction of parameter uncertainty for accurate mathematical modeling, especially regarding critical model parts such as friction, is important to properly predetermine the load path and to design structural dimensions or to tune the controller for semi-active and active systems, [56, 108].

This chapter outlines the background of passive, semi-active and active approaches for load redistribution within load-bearing structures, classifies uncertainty and gives an overview of uncertainty consideration for calibration and model prediction. First, passive approaches for the design optimization of load-bearing structures are introduced and semi-active and active structure manipulation measures related to load redistribution are outlined. Second, uncertainty is classified with respect to the SFB 805 and separated into categories for identification and evaluation. Furthermore, uncertainty quantification and reduction approaches are discussed and, finally, the chapter closes with conclusions and the distinction between the state of research and the work presented in this thesis.

2.1 Load redistribution in load-bearing structures

Any load applied to a load-bearing structure is distributed through a predetermined load path that is, mostly, not subject to any intentional changes during the structure's lifetime. However, the need for redistributing loads within a load-bearing structure may arise, if parts of the load-bearing structure should be relieved and protected, e.g. against overload. Weakened structural components can be bypassed

to prevent the structure from failure or malfunction. Load redistribution can be achieved by passive, semi-active or active approaches, as explained in this section. The classification into passive, semi-active and active technologies result from the amount of additional energy that is fed into the structure and whether sensors and actuators are needed, [96, 114]. Semi-active and active technologies typically allow for adaptivity, that is, the ability of a structure to adapt to changing conditions, e.g. damaged components. In the following, the load path design in general and passive, semi-active and active approaches for structure manipulation with emphasis on load redistribution within load-bearing structures are discussed.

2.1.1 Load path design and passive load redistribution

Loads applied to a load-bearing structure need to be transmitted through the structural components on an efficient and reliable load path that guarantees the structure's load-bearing capacity. During the design process, the load path is typically predetermined according to guidelines and design principles, [15, 90]. Figure 2.1 depicts exemplary different design possibilities for transmitting load through a load-bearing structure and illustrates the importance of the choice of an appropriate load path with respect to the efficient use of material. To remain below a defined limit of stress, the required amount of material increases with decreasing efficiency from a favorable design I to an unfavorable design in III.

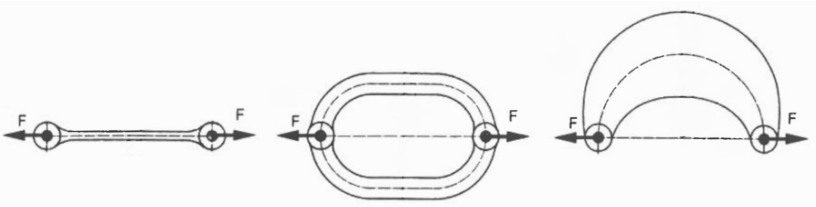

Figure 2.1: Examples for different load path possibilities from favorable in I to unfavorable in III with respect to efficient use of material, compare [15]

Passive load-bearing structures are rather limited in their ability to react to changing operation conditions, deterioration or damage. However, a passive load-bearing structure is operated without actuators and sensors and, hence, without additional energy for adaptation purpose via the actuators. Therefore, the load path and possible changes in the load path need to be considered in advance and a suitable design approach needs to be selected carefully, [36, 90]. Optimization and

robust design approaches are used to match the load path with the loading or to achieve a predefined load redistribution in case of damaged structure components, [12, 34, 77, 97].

An optimal design for the load path, e.g. regarding load capacity, material efficiency and durability, in a structural dynamic system such as a truss with known loading conditions has been investigated thoroughly in literature, e.g. in [12] and [97]. In general, typical optimization parameters are specific material and geometry properties such as Young's modulus, cross sectional areas of truss members and the topology of trusses, [34]. Another approach for optimal truss design is possible via damage tolerance that might lead to a predefined load redistribution during operation, [77]. Damage tolerance defines the ability of a structure to remain functional even in case a damage occurred. In this particular approach, a simple 18-bar truss structure is designed to be resistant to collapse despite suffering initial damage. The load is redistributed in a predefined way if parts of the structure break during operation. Any damage, however, must be considered in advance in the design process.

2.1.2 Semi-active and active load redistribution

When additional energy for actuators and sensors is introduced into a structure and used to change or control mechanical properties of the structure, such as stiffness or damping, a structure becomes semi-active, [3]. An adjustable damper with magnetorheological fluids is an example for a semi-active technology, [26]. The required additional energy for semi-active structures is typically less compared to an active approach, [41]. When additional energy is introduced into a structure, for example with force generating actuators that stabilize equilibrium conditions or attenuate vibrations, a structure becomes active, [3]. Active buckling control with piezo-elastic supports is an example for an active technology, [32, 102].

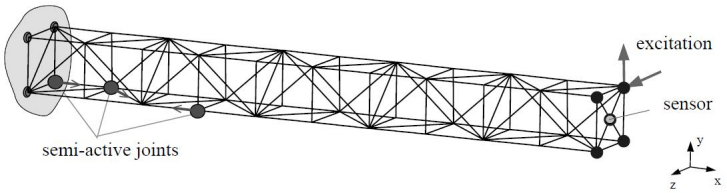

Figure 2.2: Cantilever truss structure with semi-active joints for semi-active friction damping, [38]

Semi-active and active technologies found in literature mostly aim for an improvement regarding the dynamic behavior of truss members via vibration or damping control. For example in [39], [38] and [41], the authors use semi-active joints with piezoelectric washers and stack actuators to improve the damping of two connected beams and a cantilever truss structure, figure 2.2. The concept of semi-active friction force by utilizing controlled varying normal force is also considered in [5]. In systems with free to move but guided structural components within a defined trajectory like landing gears or car-suspension, (semi-)active systems are typically used for vibration control, [22, 112]. A summary of semi-active control strategies for vibration suppression and damping can be found in [60]. Load path adaption or redistribution is not explicitly addressed.

However, some research was conducted for enhanced load path distribution or change with active technologies in trusses. Studies to enhance the load capacity that could lead to load path redistribution are made in [61] for a simple 9-bar truss with hydraulic jacks to apply internal forces and neuronal network controller to react to unexpected high static load. In other studies, several beams of truss structures are substituted with idealized actuators in an academic way to enhance the load capacity by modifying the load path and to react to unknown loads, [69, 109]. Both approaches use actuators which change their axial length and, hence, the bending stiffness of the examined truss to create a fully stressed state of all the beams in the truss. Additionally, local load path redistribution that occurs within one structural component is conducted in [95] to reduce crack propagation from an initial notch by inducing active compression forces near the crack tip, figure 2.3. By this approach, the stress intensity at the crack tip can be reduced significantly to achieve a 20% reduction of the crack propagation rate. Further approaches for crack propagation reduction are summarized in [119].

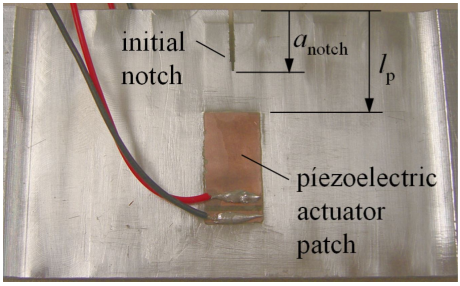

Figure 2.3: Sample with initial notch as crack starting point and piezoelectric patch actuator for local load redistribution, [95]

In an active engine mount presented in [66], the local load path is redistribution to separate relatively high (quasi-)static loads and relatively small dynamic loads, figure 2.4. Piezoelectric actuators are almost solely loaded with the dynamic loads and used for vibration isolation. The (quasi-)static loads are beared by stronger elastic coupling elements. Therefore, sizing of the piezoelectric actuators can be more specific for vibration isolation and is independent of (quasi-)static loads. However, the local approaches in [95, 119] and [66] did not investigate the redistribution of load paths through a whole structure with several components neither the redistribution of loads between several supports to prevent damage or reduce the damage's impact.

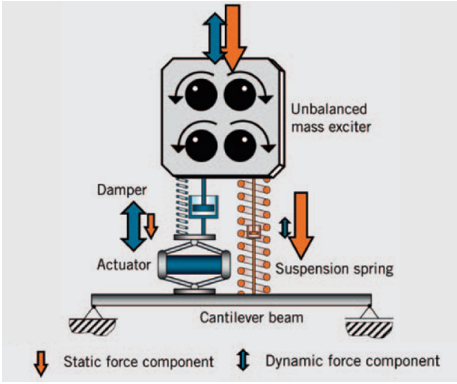

Figure 2.4: Topology of the active engine mount with almost separated load paths for (quasi-)static and dynamic loads, [66]

The load redistribution concept investigated by earlier own studies is used to avoid locking in a two-mass-oscillator representing a quarter-car-model, [43]. In case of overloading, active guidance elements provide an additional load path to bear parts of the loading. Load redistribution by shifting loads from a weaker support to a stronger support of a load-bearing structure is investigated numerically in [42, 44] and also experimentally in [45]. In case of weaker supports, the undesired misalignment of structural components like a beam can be compensated or reduced due to semi-active guidance elements.

Summing up, semi-active and active approaches can provide the ability for a load-bearing structure to adapt to changing conditions or events, e.g. damaged components, and are superior to passive structures to that effect. Furthermore, semi-active approaches possess a reasonable cost-benefit ratio, typically operate

using low power and are less complex compared to active approaches, [26, 38, 39], and predestines a semi-active technology for retrofitting into existing structural components. So far, studies on semi-active or active approaches to adapt the dynamic behavior of a structure have primarily investigated damping or vibration control and not load redistribution. This thesis focuses on a solution for semi-active load redistribution in a mechanical load-bearing structure in use, section 3.1.

2.2 Uncertainty

In general, uncertainty describes a lack of knowledge that leads to unknown or only partially known system or model behavior caused by varying system properties and operating conditions as well as disregarded or simplified physics, [21, 36, 68, 87]. Consequently, uncertainty may result in model prediction inadequacies of numerical simulations or, during operation of a physical system, unforeseen or at least varying system properties and system behavior, [88, 106]. In the working hypothesis of the SFB 805 according to [52] and [70],

> *uncertainty occurs when process properties of a system can not, or only partially be determined.*

In load-bearing structures, the load is transmitted from the load application through a predetermined load path to the structures' supports, compare figure 1.1 and 1.2. However, if system properties, e.g. damping and stiffness or strength of the supports, are uncertain and vary over time caused by damage or degradation, the predetermined load path might become inappropriate since its load-bearing capability is uncertain. An inappropriate load path is characterized by loads that exceed the load-bearing capacity or excitation frequencies that cause comfort restrictions.

The SFB 805 suggests the following steps to control uncertainty: Identification and evaluation of uncertainty and, eventually, applying methodical approaches and technological solutions to compensate or reduce uncertainty, [29, 52]. To identify uncertainty, a classification of uncertainty is introduced in section 2.2.1. The methodical quantification of uncertainty is part of the evaluation step and discussed in section 2.2.2 in conjunction with methodical approaches and technological solutions for uncertainty reduction in model predictions and the application of physical load-bearing structures.

2.2.1 Uncertainty classification

Uncertainty is a widely but colloquially imprecisely used terminology. For a meaningful usage, a classification is needed. According to the SFB 805, uncertainty in load-bearing structures occurs within the three phases of the product life, from development via production to usage, [30, 31, 47, 52]. The SFB 805 classification, that is also in line with other classifications found in [63] and [65], distinguishes data and model uncertainty:

- **Data uncertainty** summarizes uncertainty that can be allocated to system parameters and states. It occurs if quantities cannot be stated deterministically and therefore are subjected to variations, which is mostly the case. Possible sources are manufacturing tolerances, wear or deterioration, measurement uncertainty and changing ambient conditions among others. System parameters that may be affected by these sources are quantities such as geometry, material properties, initial conditions or boundary conditions and system loads. These parameters are regarded as *known unknowns*, [8]. Data uncertainty results in numerical simulation prediction inadequacies, if interpreted as computer model input or in system behavior variations if referred to a structure in operation. Data uncertainy may be divided into the following three categories according to the SFB 805, [70]:

  - **Probabilistic uncertainty** is given if a known or assumed probability distribution functions are used to describe a non-deterministic value of an arbitrary parameter.

  - **Non-probabilistic uncertainty** is given if known or assumed membership function or intervals are used to describe a non-deterministic value of an arbitrary parameter. Lower and upper limits can be specified for each parameter but the variability itself is uncertain.

  - **Disregarded uncertainty** is given if the value of a parameter or state is considered deterministic. No declaration regarding any uncertainty is made.

- **Model uncertainty** arises from simplifications, assumptions, conceptualizations, abstractions, approximations, and mathematical formulations on which the model relies as well as model coupling, [106]. Due to these sources of model uncertainty, a model only partly represents the relevant reality, [54]. Model uncertainty results in numerical simulation prediction

inadequacies,which are regarded as *unknown unknowns*, [8, 63]. Model uncertainty still remains even after parameter calibration as the discrepancy between model predictions and the relevant reality.

A further classification of uncertainty is the distinction in aleatoric and epistemic uncertainty, [19, 74, 106]. The random based **Aleatoric uncertainty** is inevitable since it is inherent to the problem or system. Even by gaining additional knowledge, it is irreducible. In contrast, the knowledge based **Epistemic uncertainty** results basically from lack of knowledge and, hence, can be reduced by gaining additional knowledge, e.g. adding former missing physics to models. A clear distinction between aleatoric and epistemic uncertainty is mostly not given, [68, 106].

In the scope of this thesis, data uncertainty is addressed to quantify parameter uncertainty and the resulting model prediction variability. Simultaneously, the model prediction accuracy is improved by reducing the parameter uncertainty and fitting the numerical simulation results to experimental data, see chapter 5. Additionally, parameter uncertainty in the system condition, such as the support stiffness, of a real load-bearing structure are compensated by means of semi-active guidance elements and changing the load path in operation, see chapter 7.

2.2.2 Uncertainty quantification and reduction

On the way to control uncertainty according to the holistic SFB 805 approach, section 2.2, the quantification of uncertainty and, eventually, the reduction of uncertainty are steps to be conducted. This section introduces how uncertainty can be quantified and reduced applying methodological approaches incorporating statistic measures for model predictions and technological solutions for the application of physical systems.

Uncertainty quantification

Uncertainty quantification is an interdisciplinary field to methodologically investigate the inevitable discrepancy between model predictions and observations of the reality resulting in probabilistic statements regarding the confidence of the model prediction and model parameters. In order to increase the confidence in model predictions, it is essential to quantify the uncertainty. The uncertainty in model predictions arise from several sources as classified in the previous section 2.2.1. Comprehensive literature concerning uncertainty quantification frameworks is available, see e.g. [6, 28, 76, 99, 106, 107]. Uncertainty quantification comprises, among others, the fields of statistics, probability theory and numerical

analysis and topics like parameter selection, sensitivity analysis as well as model calibration and validation, [76, 106]. In the following, the approaches for quantification and visualization of data uncertainty used in the scope of this thesis are introduced.

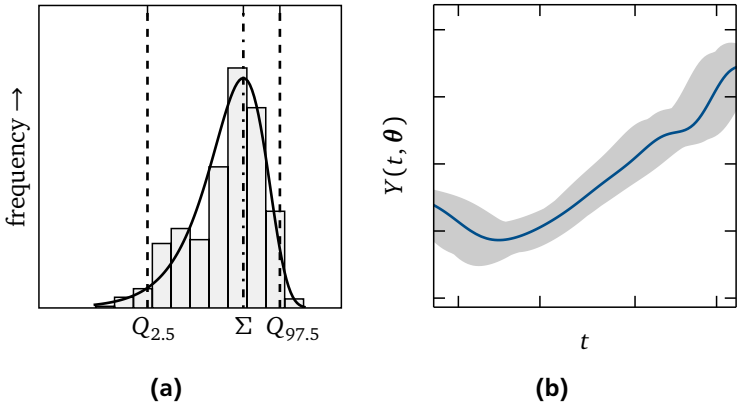

Figure 2.5: Exemplary uncertainty quantification, **(a)** histogram of empirical sample for random variable X with probabilistic measures mode Σ, the $Q_{2.5}$ and $Q_{97.5}$ percentiles, and the continuous probability distribution (——), **(b)** MONTE CARLO simulation results of an arbitrary function $Y(t, \boldsymbol{\theta})$ for varying parameters $\boldsymbol{\theta}$ (▬) and mode values (——)

Data uncertainty of an arbitrary property, represented by the variation of the random variable X that is given by an empirical sample, can be quantified and visualized graphically by histograms, [19, 106]. An empirical sample is a particular set of realizations of the random variable X. Histograms show the frequencies of observations or events in a specified range of values (bins). From the sample data, probabilistic measures, e.g. arithmetic means, modes or interpercentiles, can be derived and used to characterize the central tendency and the dispersion of the sample. Figure 2.5(a) depicts an exemplary histogram of an empirical sample and the approximation by a previously selected continuous probability distribution. The mode Σ represents the most likely value and the $Q_{2.5}$ and $Q_{97.5}$ percentiles contain 2.5% and 97.5% of the parameter space. The variability of a random variable X, e.g. the distribution of a uncertain model parameter, can be quantified by the interpercentile range

$$R_{95} = Q_{97.5} - Q_{2.5}, \tag{2.1}$$

that contains 95% of all observations or possible parameter values, respectively.

The distributions of uncertain model parameters can be obtained on several ways. Manufacturer information, e.g. tolerances of a bore diameter, can be used to quantify the uncertainty of a model parameter. Via forward parameter calibration it is also possible to derive distributions of uncertain model parameters for uncertainty quantification, [47, 101]. Forward calibration describes multiple calibration iterations for each model parameter to be calibrated with varying system configurations leading to a distributions of the parameter values. Inverse approaches for parameter calibration and uncertainty quantification like the BAYESIAN inference statistically calibrate the model parameters to experimental data and result in distributions for the model parameters to be calibrated, [7, 20, 50, 106]. The distributions, in turn, can be visualized in histograms or continuous probability distributions. Probabilistic measures like modes or interpercentiles (2.1) can be applied to quantify the data uncertainty of model parameters.

MONTE CARLO (MC) simulation techniques are used for forward uncertainty propagation of uncertain model parameters to quantify the variation of the model predictions, [35, 49, 98]. Figure 2.5(b) depicts an exemplary MC simulation result for an arbitrary function $Y(t, \boldsymbol{\theta})$ representing the model predictions with uncertain and thus varying parameters $\boldsymbol{\theta}$ and an independent variable t, e.g. the time. The solid blue curve represents a single simulation result with the modes of the parameters and the shaded area represents the R_{95} bounds for multiple MC simulation runs with arbitrary parameter combinations with former determined parameter distributions, e.g. via BAYESIAN inference.

Uncertainty reduction

For uncertainty reduction, technological solutions and methodological approaches can be applied to adapt the system behavior or increase the model prediction accuracy. In literature, semi-active and active technological solutions are known to adapt system behavior to changing conditions or to augment the usability of systems, [58]. This is mostly done by augmenting the former passive system with new technologies via adding actuators, sensors, data acquisition including the control and the necessary energy to operate these components.

Typical technological solutions aim to reduce undesired vibrations, e.g. in lightweight structure or vehicle suspension, [22, 41, 48, 60, 110], or to increase the bearable load of load-bearing structures from single beams through to complete trusses, [31, 61, 101] and compare also section 2.1.2. Variation in the desired system behavior, e.g. bearable load, can be reduced and, hence, uncertainty is reduced with technological solutions. Figure 2.6 exemplarily illustrates a beam-column support with integrated piezoelectric transducers as a technological

solutions for vibration attenuation and buckling control that reduces the dispersion of the desired system behavior and, hence, the uncertainty during operation of the system, [32, 47, 101]. Further examples for vibration attenuation in rotating machinery are magnetic bearings, [16, 79, 94], or active rolling bearings augmented by piezoelectric actuators, [10, 91], that also aim to reduce the uncertainty during operation and thereby enlarge the operating range and increase the efficiency.

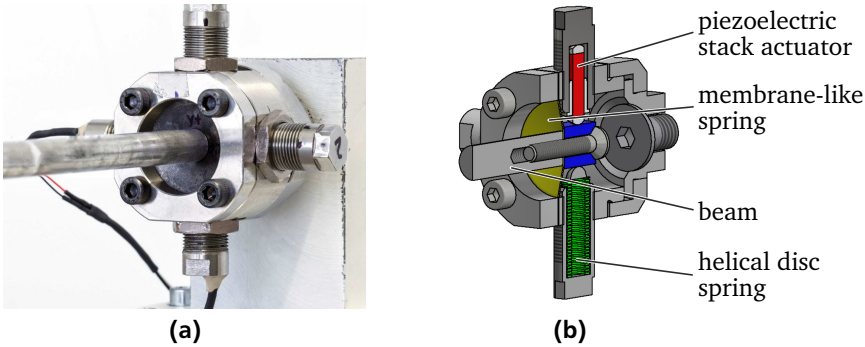

Figure 2.6: Example for technological uncertainty reduction: Piezo-elastic support for vibration attenuation and active buckling control, [32, 47, 101], **(a)** realization and **(b)** CAD section view with labeled characteristic components

Uncertainty in model-based predictions of system behavior and properties results mainly from data or parameter uncertainty and model uncertainty or discrepancy, [8, 20, 106], see section 2.2.1. This thesis focuses on methodological uncertainty reduction via model parameter calibration. The challenge to adequately calibrate model parameters arises since parameters can be unmeasurable and the exact parameter values remain uncertain, e.g. the internal state of a friction model, see section 3.2.2. Parameter uncertainty might also be caused by model uncertainty, e.g. due to model simplifications such as linearization and discrete masses. Model simplifications, in turn, may lead to uncertain model parameters, e.g. if system components are assumed to be free of mass and the disregarded mass is added to an adjacent degree of freedom, compare section 3.2.2 and section 5.2.2. Therefore, special attention needs to be drawn to model parameters that arise from model simplifications as well as to model parameters that strongly dependent on the case of application with widely varying values, e.g. in friction models, [13, 18].

Two principle approaches for model parameter calibration are distinguished in literature:

- **Deterministic** parameter calibration is commonly done by solving an optimization problem to find specific values for each model parameter to be calibrated that best fit the calibration criteria. Deterministic optimization approaches, e.g. [38, 72, 116, 117], are searching for the best-fitting parameter values and then treating the parameters as known and fixed. This leads to neglected but still existing parameter uncertainty after calibration. For example in [116], the friction model parameters are identified with the Novel Evolutionary Algorithm optimization. A similar procedure with a genetic optimization algorithm and a particle swarm optimization algorithm can be found in [72] and [117] for mechanical servo systems. In [17], a non-linear numerical optimization to identify and calibrate friction model parameters is performed. In these studies, deterministic values for the calibrated model parameters are stated but remaining parameter uncertainty in disregarded.
- **Non-deterministic** calibration approaches aim to achieve statistical consistency between model output and experimental data by solving an inverse problem, [63, 85, 106]. For example in [7], the FE model parameters of a historic masonry monument are statistically calibrated. The same procedure is used in [83] and [113] to calibrate a wind turbine blade FE model. It is possible to find a simplified but still credible model by reducing the prediction uncertainty applying verification and validation methods. In [50], BAYESIAN inference is successfully used to calibrate parameters for several friction models and, hence, reducing parameter uncertainty. The calibrated parameters are stated as distributions representing the remaining uncertainty.

The mentioned examples can only provide a selected overview of the wide variety of deterministic and non-deterministic calibration applications in literature.

To exemplarily demonstrate the effect of non-deterministic calibration, figure 2.7 illustrates simulation predictions with uncalibrated parameters in (a) and simulation predictions with non-deterministic calibrated parameters in (b) for an arbitrary function or model $Y(t, \theta)$ with the model parameters θ and an independent variable t, compare figure 2.5.

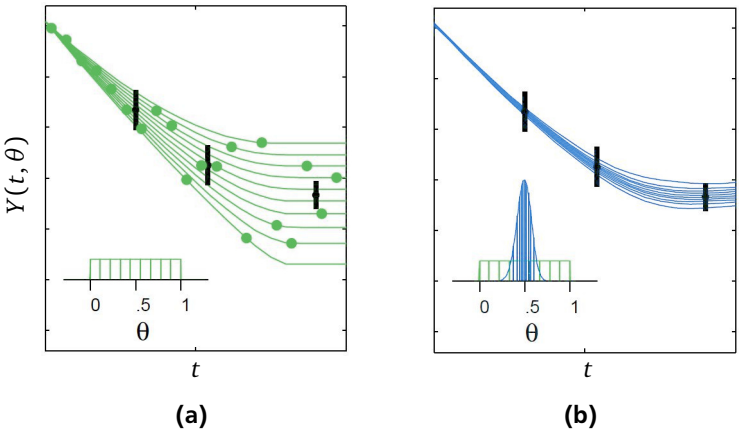

Figure 2.7: Example for methodological uncertainty reduction via non-deterministic parameter calibration, **(a)** predictions of model $Y(t,\theta)$ with uncalibrated uncertain parameter θ that is equal distributed in the parameter range 0 to 1, and **(b)** with calibrated uncertain parameter θ with obliviously reduced likely parameter range, compare [57]

Summing up, the BAYSIAN inference as a non-deterministic parameter calibration approach is utilized in the scope of this thesis since it enables to quantify and reduce model parameter uncertainty concurrently, chapter 5. The model prediction accuracy with the statistically calibrated model parameters is eventually evaluated with MC simulations to obtain uncertainty bounds for the model predictions, section 7.2.

2.3 Conclusions and distinction

The reliable and efficient design of the load path in passive load-bearing structures is investigated thoroughly in literature, [12, 15, 34, 90, 97], but in-use load redistribution is inherently not addressed. Previous studies investigating semi-active or active system adaption mostly focus on enhancing vibration behavior, [11, 22, 112], or increasing load-bearing capacity in general, [31, 61, 103]. So far, load redistribution to relieve weak or damaged parts of load-bearing structures for SHC is not addressed in these studies. Consequently, it is investigated in the scope of this thesis:

- In order to technologically reduce uncertainty arising from an inappropriate load path, section 2.2, semi-active guidance elements to redistribute load for SHC are proposed. Therefore, already existing components of a load-bearing structure, the guidance elements, are enhanced by electromagnetic actuators, section 4.2, to influence the load-bearing structure's load path according to the actual structure health conditions, section 3.1. A semi-active technological solution is preferred since it possess a good compromise between additional components, complexity and load redistribution capability, section 2.1.

Uncertainty quantification and reduction in model predictions can be achieved via statistical measures for parameter calibration, [63, 106]. In particular, the BAYESIAN inference is applied among others in [50, 55, 71, 83, 113, 118] to evaluate the model parameter uncertainty and has proven its eligibility for methodological uncertainty quantification and reduction. Parameter uncertainty quantification and reduction for the mathematical model of a load-bearing structure with semi-active guidance elements in combination with the experimental investigation of the structure is not yet presented in literature. Consequently, it is investigated in the scope of this thesis:

- In order to methodologically quantify and reduce the data uncertainty, the BAYESIAN inference parameter calibration is applied, chapter 5. This non-deterministic calibration approach is preferred to a deterministic calibration approach since the BAYESIAN inference statistically correlate the model predictions with the measurements by solving an inverse problem, [85]. It enables to calibrate the model parameters and simultaneously quantify their uncertainty.

The aforementioned two manifestations of technologically and methodologically uncertainty evaluation also emerge from section 1.2 as research objectives for this thesis.

3 Load-bearing structure for load redistribution

In order to investigate the potential of load redistribution in a load-bearing structure in the context of SHC, section 1.1, an adequate system is needed to demonstrate the potential uncertainty in the required load path in a passive system and compare it to a system with semi-active measures for load redistribution. This chapter presents the simplified load-bearing structure used for the investigation of semi-active load redistribution in this thesis and how the simplified load-bearing structure is derived from the MAFDS, figure 1.2. Also, the basic concept and objectives of load redistribution are introduced. Afterwards, the mathematical model of the simplified load-bearing structure is derived including all sub-models like friction and the electromagnetic brake and finally formulated in state space representation.

3.1 Exemplary load-bearing structure and load redistribution concept

The MAFDS is a full-size spatial load-bearing structure from which the simplified planar load-bearing structure investigated in this thesis is derived, compare section 1.1. In this context, spatial means that the load is distributed to three or more supports whereas planar means that the load is distributed to two supports.

The spatial structure of the MAFDS in figure 3.1(a) is simplified and downscaled to a planar load-bearing structure in figure 3.1(b) to facilitate the investigation of load redistribution by means of semi-active guidance elements. By that, the structure's complexity and dimensionality are reduced with the following assumptions:

- The upper truss is downsized and approximated by a rigid beam.
- The lower truss is downsized and approximated by a single mass.
- The two guidance elements in the planar load-bearing structure simulate the three guidance elements in the spatial MAFDS and a similar defined

kinematic with a specified relative displacement of structural components is achieved.

- For practical use, the simplified load-bearing structure in figure 3.1(b) is rotated around 180 degrees.

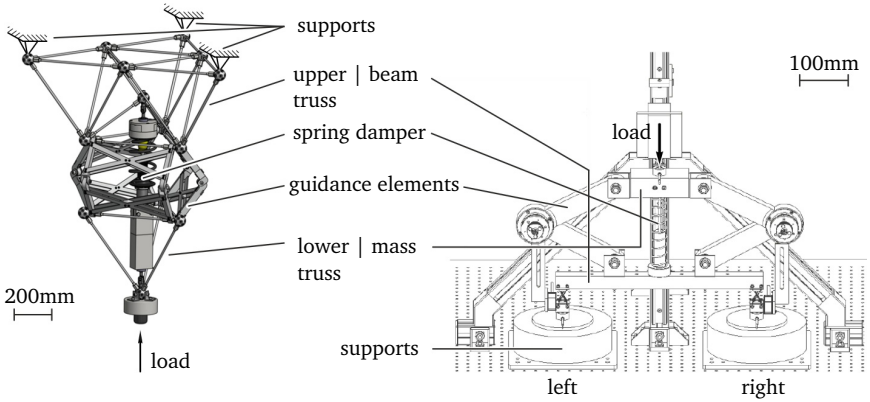

Figure 3.1: MAFDS and simplified load-bearing structure for load redistribution investigations, comparison of similar components

The load-bearing structure in figure 3.1(b) is a reduced surrogate model of the MAFDS in figure 3.1(a) to reduce the experimental effort and the number of potential load path. The mass is connected to the rigid beam by a spring-damper system and the two guidance elements. The rigid beam is supported at its ends by two supports. To change the load path via load redistribution, the kinematic guidance elements are augmented by semi-active kinetic functions with controlled friction forces in the middle joints applied by an electromagnetic actuator, compare figure 4.4.

The concept of load redistribution for SHC, as used throughout this thesis, means shifting load between the two supports during operation according to current or anticipated damage, compare section 1.2. A damaged or weakened support can be relieved by using the semi-active guidance elements as an additional load path to the spring-damper, so that parts of the load can be bypassed through the guidance elements. The basic idea is to shift loads that originally only go through the spring-damper in a way to also go through the semi-active guidance elements. For that, two different control strategies are investigated, chapter 6,

- to reduce the beam's misalignment φ, figure 3.4(a), that is defined as malfunction in the scope of this thesis and

- to achieve a defined load ratio between the left and right support, figure 3.1(b).

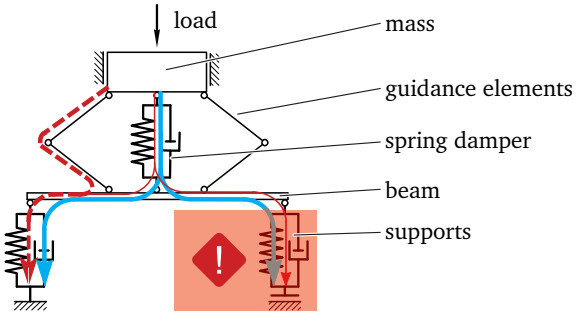

Figure 3.2: Concept of load redistribution illustrated for the mechanical model of the simplified load-bearing structure from figure 3.1 with predetermined load path (——), additional load path through the left guidance element (– –) and remaining less exhausted load path (——) with the right support ( ) assumed to be damaged, indicated by the exclamation point

Figure 3.2 illustrates an example of load redistribution in the load-bearing structure investigated in this thesis. If no reason for load redistribution occurs, such as damage or deterioration of the supports, the load is equally distributed to both supports resulting in the predetermined load path for the load-bearing structure (thick blue line). For example, in case of deteriorated load capacity of the right support, it can be relieved by using the left semi-active guidance element as an additional load path to the spring-damper. Portions of the load are transfered through the guidance element directly to the undamaged left support. The additional load path is highlighted by a dashed red line passing through the left guidance element compared to a thin red line representing a less exhausted load path through the spring damper.

3.2 Mathematical model of the load-bearing structure with semi-active guidance elements

The mathematical model of the semi-active load-bearing structure for load redistribution is divided into two main parts, a linear part representing the **load-bearing structure** and a nonlinear part representing the **semi-active guidance elements**

with friction phenomena and the electromagnetic actuator to operate the friction brake. The mathematical model of the load-bearing structure is introduced in section 3.2.1. The mathematical model of the semi-active guidance elements is introduced in section 3.2.2, separated into paragraphs accounting for the guidance elements' kinematic and kinetic characteristics, the friction model and the electromagnetic actuator. Finally, the individual mathematical models are assembled and transferred into the state space representation in section 3.2.3. Figure 3.3 provides a graphical overview of the sub-models and their interactions that are explained in details in the related sections.

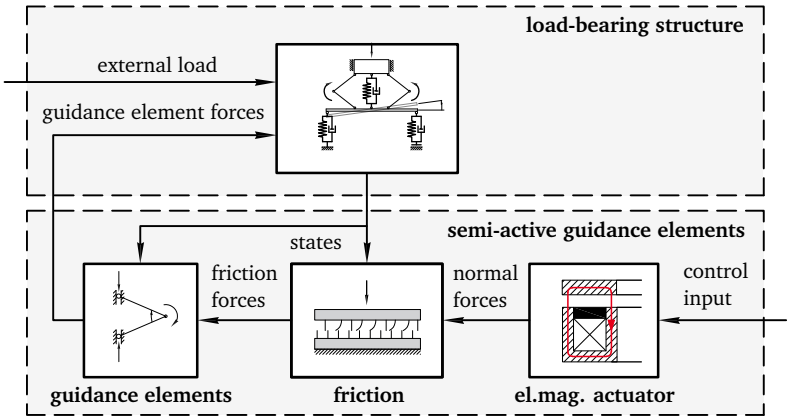

Figure 3.3: Model overview and organization of section 3.2

In this thesis, the derived mathematical model is used to predict and evaluate the dynamic behavior and the load path of the load-bearing structure with and without semi-active guidance elements. The validity of the NEWTONIAN mechanic is assumed for all models, [51]. The BAYESIAN inference is performed to calibrate uncertain model parameters and simultaneously quantify the parameter uncertainty, see chapter 5. Furthermore, the calibrated model is used to numerically tune the controllers for the different load redistribution strategies in simulation and experiment, see chapter 6 and to evaluate the load redistribution capability, see. chapter 7.

3.2.1 Load-bearing structure model

Figure 3.4 depicts the mathematical model with the related model parameters of the load-bearing structure and the free body diagram. The load-bearing struc-

ture is approximated by three independent degrees of freedom (DOF) that are the vertical displacements in z_A- and z_B-direction and the rotation in φ-direction, figure 3.4(a). The mathematical model consists of a movable mass m_A, a rigid beam mass m_B with moment of inertia Θ_B in x-z-plane and length l_B, and the associated time-dependent DOF $z_A(t) \hat{=} z_A$, $z_B(t) \hat{=} z_B$ and $\varphi(t) \hat{=} \varphi$. Once introduced, the time dependency (t) is omitted in the following for the purpose of readability. The masses m_A and m_B are symmetrically connected with each other by two semi-active guidance elements, one on each side of the beam. The semi-active guidance elements, see section 3.2.2, are connected to the beam at the contact points $x = a$ and $x = l_B - a$. A spring-damper system with stiffness and damping coefficients k_S and b_S is connected to the beam at $x = l_B/2$. The beam is connected to the ground at $x = 0$ and $x = l_B$ via two elastic supports L and R, represented by two springs and two viscous dampers with stiffnesses k_L and k_R and damping coefficients b_L and b_R, [45].

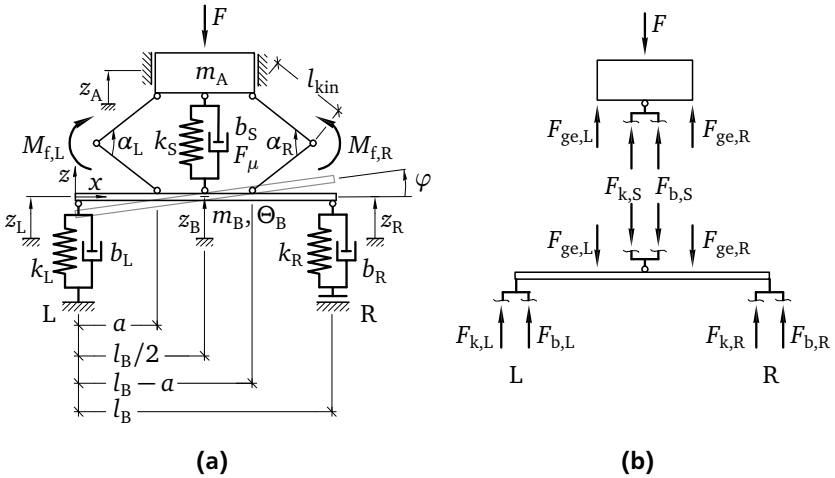

Figure 3.4: Mechanical model of the load-bearing structure, **(a)** degrees of freedom and relevant model parameters and **(b)** free body diagram with internal and external forces

The derived model underlies the following specific model simplifications:

- Undesired friction occurring in joints, parallel guidance rails and supports is simplified and summarized to a single dissipative force F_δ in equation (3.4). The resulting uncertainty appears in the related parameter F_μ as parame-

ter uncertainty that is reduced due to model parameter calibration in section 5.2.

- The assumption of lumped masses and rigid bodies leads to neglected structural elasticities of the components. The structural elasticities of the components are significantly larger than the considered elasticities of the spring and supports and, hence, do not contribute to the relevant dynamic behavior for load redistribution.
- Although the simplified load-bearing structure is assumed to be planar, the experimental test setup, compare section 4, is inevitable spatial. However, this has only little to no effect for the relevant z-direction.
- The spring-damper system and the guidance elements are assumed to be free of mass. Their mass contributions are allocated to the masses m_A and m_B and are considered as parameter uncertainty in section 5.2.

The model simplifications might lead to model uncertainty according to section 2.2.1 and can also manifest in uncertain model parameters resulting from the simplifications. Model uncertainty is not explicitly addressed in the scope of this thesis. Nevertheless, the parameter uncertainty resulting from model simplifications is considered in chapter 5 via parameter calibration.

The linear time-dependent support displacements $z_\mathrm{L}(t) \triangleq z_\mathrm{L}$ and $z_\mathrm{R}(t) \triangleq z_\mathrm{R}$ in figure 3.4(a)

$$z_\mathrm{L} = -\varphi \, \frac{l_\mathrm{B}}{2} + z_\mathrm{B} \qquad \text{and} \qquad z_\mathrm{R} = \varphi \, \frac{l_\mathrm{B}}{2} + z_\mathrm{B} \tag{3.1}$$

result from the two DOF z_B and φ related to the beam assuming small beam angles φ with $\sin\varphi \approx \varphi$. The support displacement difference $z_\mathrm{R} - z_\mathrm{L}$ represents the beam's misalignment, which is defined as malfunction with the intention of being reduced by control, see section 6.1.1. With $z_\mathrm{ge,L}(t) \triangleq z_\mathrm{ge,L}$ and $z_\mathrm{ge,R}(t) \triangleq z_\mathrm{ge,R}$, the linear time-dependent displacements

$$z_\mathrm{ge,L} = -\varphi \left(\frac{l_\mathrm{B}}{2} - a \right) + z_\mathrm{B} \qquad \text{and} \qquad z_\mathrm{ge,R} = \varphi \left(\frac{l_\mathrm{B}}{2} + a \right) + z_\mathrm{B} \tag{3.2}$$

are the beam displacement at the semi-active guidance element connection points again assuming small beam angles φ with $\sin\varphi \approx \varphi$. According to figure 3.4b, the internal spring and damping forces of the spring-damper system are

$$F_\mathrm{k,S} = k_\mathrm{S} \left(z_\mathrm{B} - z_\mathrm{A} \right), \tag{3.3a}$$

$$F_\mathrm{b,S} = b_\mathrm{S} \left(\dot{z}_\mathrm{B} - \dot{z}_\mathrm{A} \right) + F_\delta \tag{3.3b}$$

with the dissipative force caused by inherent friction

$$F_{\delta} = F_{\mu} \tanh\left(\frac{(\dot{z}_{\mathrm{B}} - \dot{z}_{\mathrm{A}})}{v_0}\right). \tag{3.4}$$

The tanh-function causes a constant change of the friction induced force F_{μ} at the zero-crossing of $(\dot{z}_{\mathrm{B}} - \dot{z}_{\mathrm{A}})$ to yield the dissipative force F_{δ} and avoids numerical issues associated with COULOMB friction such as model discontinuity, [67]. The constant velocity v_0 defines the slope of the tanh-function and is arbitrary except for $v_0 < v_S$ smaller than STRIBECK velocity, see section 3.2.2.

The internal spring and damping forces of the supports L and R are

$$F_{\mathrm{k,L}} = -k_{\mathrm{L}} z_{\mathrm{L}} \quad \text{and} \quad F_{\mathrm{b,L}} = -b_{\mathrm{L}} \dot{z}_{\mathrm{L}} \tag{3.5a}$$

$$F_{\mathrm{k,R}} = -k_{\mathrm{R}} z_{\mathrm{R}} \quad \text{and} \quad F_{\mathrm{b,R}} = -b_{\mathrm{R}} \dot{z}_{\mathrm{R}}. \tag{3.5b}$$

The combined support reaction and spring-damper system forces are

$$F_{\mathrm{L}} = F_{\mathrm{k,L}} + F_{\mathrm{b,L}}, \tag{3.6a}$$

$$F_{\mathrm{R}} = F_{\mathrm{k,R}} + F_{\mathrm{b,R}}, \tag{3.6b}$$

$$F_{\mathrm{S}} = F_{\mathrm{k,S}} + F_{\mathrm{b,S}}. \tag{3.6c}$$

The support reaction forces F_{L} and F_{R} are used to evaluate the load path of the load-bearing structure and as control variables, see section 6.1.2. The external excitation force $F(t) \triangleq F$

$$F = \begin{cases} 0 & \text{for } t < t_{\mathrm{exc}}, \\ \widehat{F} & \text{for } t \geq t_{\mathrm{exc}} \end{cases} \tag{3.7}$$

is assumed as a step-function with the time of excitation t_{exc}. When assuming the load-bearing structure to be passive, the guidance elements only have a kinematic function. When assuming the load-bearing structure to be semi-active with load redistribution, the kinematic guidance elements provide additional moments $M_{\mathrm{f,L}}$ and $M_{\mathrm{f,R}}$, figure 3.4(a), resulting in additional kinetic functions. $M_{\mathrm{f,L}}$ and $M_{\mathrm{f,R}}$ result in vertical guidance element forces $F_{\mathrm{ge,L}}$ and $F_{\mathrm{ge,R}}$ that directly act on mass m_{A} and the connection points at $x = a$ and $x = l_{\mathrm{B}} - a$ on the beam and are responsible for the load redistribution, figure 3.4(b). They are derived in the following section 3.2.2.

According to the direction of internal forces in equations (3.3) and (3.5) and figure 3.4(b), the linear equation of motion for the mass m_A becomes

$$m_A\ddot{z}_A - b_S(\dot{z}_B - \dot{z}_A) - k_S(z_B - z_A) = -F + F_\delta + F_{ge,L} + F_{ge,R} \tag{3.8}$$

and for the beam m_B and Θ_B

$$\begin{aligned} m_B\ddot{z}_B + b_S(\dot{z}_B - \dot{z}_A) + k_S(z_B - z_A) + k_L\left(-\varphi\,\frac{l_B}{2} + z_B\right) + b_L\left(-\dot{\varphi}\,\frac{l_B}{2} + \dot{z}_B\right)\ldots \\ + k_R\left(\varphi\,\frac{l_B}{2} + z_B\right) + b_R\left(\dot{\varphi}\,\frac{l_B}{2} + \dot{z}_B\right) = -F_\delta - F_{ge,L} - F_{ge,R} \end{aligned} \tag{3.9a}$$

$$\begin{aligned} \Theta_B\ddot{\varphi} - k_L\,\frac{l_B}{2}\left(-\varphi\,\frac{l_B}{2} + z_B\right) - b_L\,\frac{l_B}{2}\left(-\dot{\varphi}\,\frac{l_B}{2} + \dot{z}_B\right) + k_R\,\frac{l_B}{2}\left(\varphi\,\frac{l_B}{2} + z_B\right)\ldots \\ + b_R\,\frac{l_B}{2}\left(\dot{\varphi}\,\frac{l_B}{2} + \dot{z}_B\right) = \left(\frac{l_B}{2} - a\right)F_{ge,L} - \left(\frac{l_B}{2} - a\right)F_{ge,R} \end{aligned} \tag{3.9b}$$

for translational z_A- and z_B-directions as well as for rotational φ-direction. Equations (3.8) and (3.9) merge to a linear equation of motion system of the structure to become

$$\underbrace{\begin{bmatrix} m_A & 0 & 0 \\ 0 & m_B & 0 \\ 0 & 0 & \Theta_B \end{bmatrix}}_{\boldsymbol{M}} \underbrace{\begin{bmatrix} \ddot{z}_A \\ \ddot{z}_B \\ \ddot{\varphi} \end{bmatrix}}_{\ddot{\boldsymbol{r}}} + \underbrace{\begin{bmatrix} b_S & -b_S & 0 \\ -b_S & b_S + b_L + b_R & -\frac{l_B}{2}b_L + \frac{l_B}{2}b_R \\ 0 & -\frac{l_B}{2}b_L + \frac{l_B}{2}b_R & \frac{l_B^2}{4}b_L + \frac{l_B^2}{4}b_R \end{bmatrix}}_{\boldsymbol{D}} \underbrace{\begin{bmatrix} \dot{z}_A \\ \dot{z}_B \\ \dot{\varphi} \end{bmatrix}}_{\dot{\boldsymbol{r}}} + \ldots$$

$$\underbrace{\begin{bmatrix} k_S & -k_S & 0 \\ -k_S & k_S + k_L + k_R & -\frac{l_B}{2}k_L + \frac{l_B}{2}k_R \\ 0 & -\frac{l_B}{2}k_L + \frac{l_B}{2}k_R & \frac{l_B^2}{4}k_L + \frac{l_B^2}{4}k_R \end{bmatrix}}_{\boldsymbol{K}} \underbrace{\begin{bmatrix} z_A \\ z_B \\ \varphi \end{bmatrix}}_{\boldsymbol{r}} = \underbrace{\begin{bmatrix} -F + F_\delta + F_{ge,L} + F_{ge,R} \\ -F_\delta - F_{ge,L} - F_{ge,R} \\ (\frac{l_B}{2} - a)F_{ge,L} - (\frac{l_B}{2} - a)F_{ge,R} \end{bmatrix}}_{\boldsymbol{F}}. \tag{3.10}$$

In equation (3.10), $\boldsymbol{M}$, $\boldsymbol{D}$ and $\boldsymbol{K}$ are the [3×3] mass, damping and stiffness matrices, and $\ddot{\boldsymbol{r}}$, $\dot{\boldsymbol{r}}$ and $\boldsymbol{r}$ are the [3×1] translational and angular acceleration, velocity and displacement vectors. The [3×1] force vector $\boldsymbol{F}$ in equation (3.10) contains

the external excitation force F (3.7), the dissipative force F_δ (3.4) as well as the forces $F_{\mathrm{ge,L}}$ and $F_{\mathrm{ge,R}}$ according to equation (3.15) and provided by the semi-active guidance elements in figure 3.4(b).

The mathematical model of the load-bearing structure is derived to capture the load path through the structure and the effects of uncertain boundary conditions represented by varying support stiffnesses. In particular, the mathematical model includes the misalignment of the beam φ that is defined as malfunction, see section 1.1, and the support reaction forces F_{R} and F_{L} as measures for the load path. The model is derived analytically and is later solved numerically to predict and assess the load redistribution capability.

3.2.2 Semi-active guidance elements model

The semi-active guidance elements connect the mass m_{A} and the beam to enable a defined up-and-down displacement trajectory. The semi-active approach for load redistribution is based on controlled friction brakes to enable an additional load path to the structure. This section 3.2.2 describes the modeling of the guidance elements' kinematics and kinetics, the friction model and the model of the electromagnetic actuator to operate the friction brakes. Later in chapter 6, these components are linked via the proposed load redistribution control.

The semi-active guidance elements provide the forces $F_{\mathrm{ge,L/R}}$ in figure 3.4(b), that change the dynamic behavior of the system and lead to load redistribution. The semi-active guidance element forces $F_{\mathrm{ge,L/R}}$ are applied to the mass m_{A} and the beam in (3.10) and are induced by the friction forces $F_{\mathrm{f,L/R}}$ in (3.16) and friction moments $M_{\mathrm{f,L/R}}$ in (3.20), respectively. For the purpose of readability, the subscript L/R indicating left and right is omitted in the following.

Guidance elements' kinematics and kinetics

Figure 3.5(a) depicts one guidance element that is cut free from the load-bearing structure in figure 3.4. Figure 3.5(b) depicts the derived conceptual model that is used to formulate the mathematical model. The related free-body diagram is shown in figure 3.5(c). The guidance element angle $\alpha(t) \triangleq \alpha$ as rotational DOF is transformed to the translational DOF

$$z_\alpha = 2 \sin\left(\frac{\alpha}{2}\right) l_{\mathrm{kin}} \tag{3.11}$$

and the relative displacements between the connection points z_{ge} and the mass m_A with z_A in figure 3.5(a) can be substituted by the relative displacement

$$\Delta z_{ge} = z_{ge} - z_A \tag{3.12}$$

in figure 3.5(b) and 3.5(c).

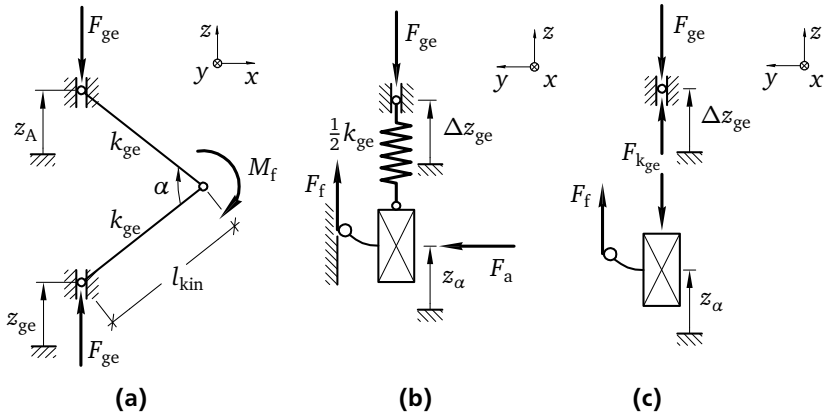

Figure 3.5: Semi-active guidance element, **(a)** mechanical concept **(b)** simplified conceptual model for mathematical modeling and **(c)** free body diagram, compare figure 3.7

The two guidance element stiffnesses k_{ge} in figure 3.5(a) can be summarized to the resulting stiffness

$$\frac{1}{2}k_{ge} = \left(\frac{1}{k_{ge}} + \frac{1}{k_{ge}}\right)^{-1} \tag{3.13}$$

in figure 3.5(b). The guidance elements' elastic deformation force in figure 3.5(c) is

$$F_{k_{ge}} = (\Delta z_{ge} - z_\alpha)\frac{1}{2}k_{ge}. \tag{3.14}$$

Assuming the guidance elements to be free of mass, compare section 5.2.2, according to the free-body diagram in figure 3.5(c) the sums of forces are

$$0 = \quad F_f - F_{k_{ge}} \tag{3.15a}$$

$$0 = -F_{ge} + F_{k_{ge}} \tag{3.15b}$$

with the guidance element force F_{ge} as input for the load-bearing structure. The vertical friction force F_f in z-direction results from the friction moment M_f in equation (3.20) as the basis for the semi-active approach for load redistribution. The friction force and moments are coupled by the kinematic transmission

$$F_f = \frac{1}{l_{kin}\cos(\alpha/2)} M_f \tag{3.16}$$

with the length l_{kin} of each link and the guidance element angle α, see figure 3.5. The friction moment M_f are controlled via the brake forces F_a according to equation (3.32) and are induced by an electromagnetic actuators, see paragraph *Electromagnetic actuator*. Eventually, the friction moments M_f augment the guidance elements with the ability to affect the load path of the load-bearing structure for the semi-active approach of load redistribution. The relation between friction moments M_f and the brake forces F_a is derived in the next paragraph introducing the *Friction model*.

Friction model

Mechanical engineering applications are often equipped with joints, bearings, connection points or energy dissipating elements that are all subjected to friction. The dynamic behavior of such systems can be mainly influenced by one or more different friction phenomena. To study and predict the dynamic behavior of a system with underlying friction, adequate models are needed. In friction brakes, a suitable friction model is essential to predict the resulting friction force in an adequate way. Depending on which friction phenomena need to be addressed, various models are found in literature.

Basically, friction models describe the relation between a normal force applied onto interacting surfaces and a consequent orthogonal friction force. These models are typically split into two classes, [40, 89, 93]. Static models like the classical Coulomb law are quite simple to model but neglect friction phenomena, such as stick-slip, presliding and hysteretic effects. Also, numerical problems due to discontinuity might lead to trouble while using static friction models, [64, 82]. Therefore, the class of dynamic friction models expand the amount of predictable friction phenomena.

Figure 3.6 exemplarily and qualitatively illustrates the friction force versus relative velocity of two surfaces in contact for the static Coulomb and the dynamic LuGre friction models. The Coulomb friction model exhibits discontinuity for relative velocity sign change and no distinction is made for the friction coefficients

of static friction (zero relative velocity) and dynamic friction (relative velocity $\neq$ zero), see figure 3.6(a). In contrast, the LuGre friction model is continuous over the relative velocity and exhibits hysteresis behavior around sign change of the relative velocity. Also, the static friction and dynamic friction coefficients differ resulting in a relative velocity dependent friction force and the Stribeck effect is captured, see figure 3.6(b).

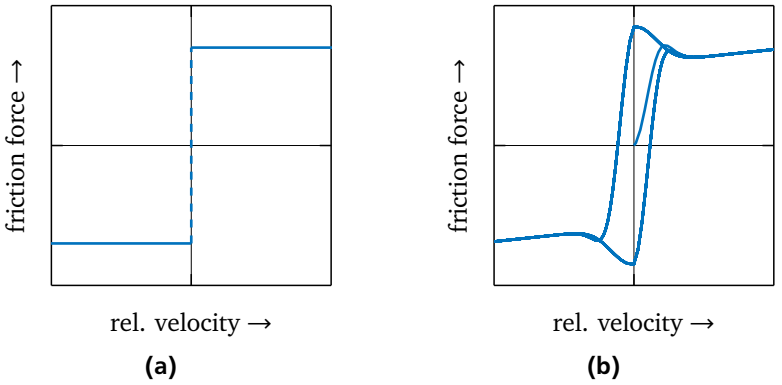

Figure 3.6: Friction force versus relative velocity of two surfaces, qualitative for **(a)** the static Coulomb friction model and **(b)** the dynamic LuGre friction model

In the context of control applications, the LuGre friction model in figure 3.7 is frequently used and well established and, hence, is used in the scope of this thesis to formulate the relation between the applied electromagnetic brake force F_a and the guidance element friction moment M_f (3.20). The dynamic LuGre friction model is capable of predicting the relevant friction effects, such as stick-slip and presliding, is mathematically stable and thereby predicting the non-linear force generation of the electromagnetic friction brake in the guidance elements' middle joints in a plausible and applicable way. For the LuGre friction model, the contact dynamics of the interacting surfaces are derived by assuming contact by bristles, [3, 13, 18]. The model assumption is illustrated in figure 3.7(a) showing the surface roughness and the bristle simplification in figure 3.7(b). The deflection of the bristles are finally condensed to an average lateral deflection of one bristle as part of the LuGre model, figure 3.7(c).

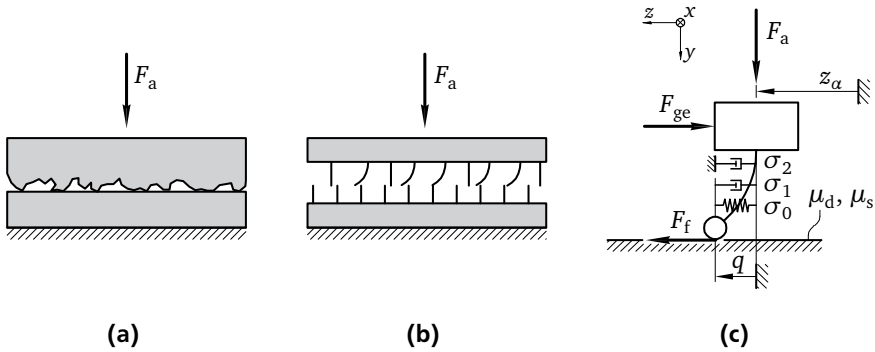

Figure 3.7: LuGre model assumptions, **(a)** surface contact roughness, **(b)** idealized surface contact by bristles and **(c)** average bristle deflection according to [18]

The averaged lateral deflection of one bristle is represented by a time dependent state variable $q(t) \hat{=} q$, which is governed by a first-order differential equation

$$\dot{q} = \dot{z}_\alpha - \frac{|\dot{z}_\alpha|}{g(\dot{z}_\alpha)} q \tag{3.17}$$

with the relative velocity $\dot{z}_\alpha$ at the friction surfaces, see equation (3.11). The function $g(\dot{z}_\alpha)$ considers different coefficients for static and dynamic friction μ_s, and μ_d, and contains information about the dependency of the relative velocity $\dot{z}_\alpha$ for the resulting friction force F_f and moment M_f in (3.20). A reasonable choice of $g(\dot{z}_\alpha)$ proposed in [18] leads to

$$g(\dot{z}_\alpha) = \frac{1}{\sigma_0} \left(\mu_d + (\mu_s - \mu_d) e^{-(\dot{z}_\alpha / v_S)^2} \right) \tag{3.18}$$

with the characteristic bristle stiffness σ_0 and the Stribeck velocity v_S, which defines the transition between stick and slip, [23]. Finally, the state dependent friction coefficient $\mu(q, \dot{q}, \dot{z}_\alpha)$ according to [18] is stated as

$$\mu(q, \dot{q}, \dot{z}_\alpha) = \sigma_0 q + \sigma_1 \dot{q} + \sigma_2 \dot{z}_\alpha \tag{3.19}$$

with the bristle damping coefficient σ_1 and viscous friction σ_2. The list of the LuGre parameters, their meaning and dimensions are given in table 3.1.

Table 3.1: LuGre friction model parameters, compare figure 3.7(c)

description	parameter	unit
bristle stiffness	σ_0	m^{-1}
bristle damping	σ_1	s/m
viscous damping	σ_2	s/m
static friction coefficient	μ_s	–
dynamic friction coefficient	μ_d	–
Stribeck velocity	v_S	m/s

The semi-active friction moment in the guidance element joints finally results from

$$M_\mathrm{f} = \mu(q, \dot{q}, \dot{z}_\alpha)\, F_\mathrm{a}\, r_\mathrm{brake} \tag{3.20}$$

with an average brake disk radius r_brake, compare figure 3.8. The controlled brake force F_a (3.32) is the contact normal force and induces the friction moment M_f via the state dependent friction coefficient $\mu(q, \dot{q}, \dot{z}_\alpha)$ (3.19). The controlled brake force F_a is provided by an electromagnetic actuator and is derived in the next paragraph.

Electromagnetic actuator

The friction brakes in the guidance element's middle joints, see figure 4.4, are operated by electromagnetic actuators. Figure 3.8 depicts a simplified magnetic circuit of the electromagnetic actuator.

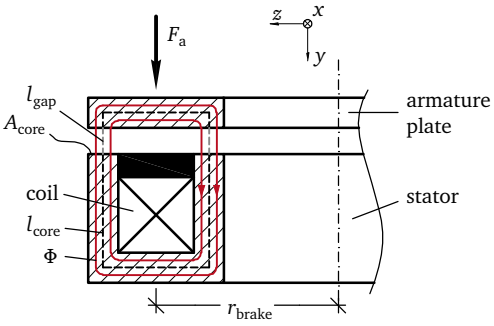

Figure 3.8: Simplified magnetic circuit of the electromagnetic actuators of the friction brakes in the guidance element's middle joints

Characteristic parameters regarding the magnetic field in figure 3.8 are the air gap l_{gap} between the armature plate and the stator, l_{core} as the length of the magnetic field path in the core material, the core cross-section area A_{core} and the magnetic flux Φ. The electromagnetic actuators provide the controlled brake forces F_{a} acting on the brake linings, see figure 4.4, and finally induce the friction forces F_{f} and moments M_{f} needed for load redistribution. The average brake disk radius r_{brake} links the controlled brake forces F_{a} and the friction moment M_{f} in equation (3.20).

The controlled brake forces F_{a} in figure 3.8 as well as in figures 3.5(b) and 3.7(c), which is a magnetic pull force, can be derived by means of an energy analysis and is given by

$$F_{\mathrm{a}} = \frac{\mathrm{d}W_{\mathrm{mag}}}{\mathrm{d}l_{\mathrm{gap}}} \tag{3.21}$$

where l_{gap} is the air gap and the magnetic field energy is

$$W_{\mathrm{mag}} = \int_V \int_B H \,\mathrm{d}B \,\mathrm{d}V, \tag{3.22}$$

[59, 62]. In equation (3.22), the magnetic field strength H is integrated over the magnetic flux density B and the volume V of the magnetic components the magnetic flux Φ is passing through. Magnetic flux leakage is neglected. Separating the magnetic field energy stored in the air gap and in the core material, equation (3.22) is written as

$$W_{\mathrm{mag}} = \int_{V_{\mathrm{gap}}} \frac{1}{2} H_{\mathrm{gap}} B_{\mathrm{gap}} \mathrm{d}V_{\mathrm{gap}} + \int_{V_{\mathrm{core}}} \frac{1}{2} H_{\mathrm{core}} B_{\mathrm{core}} \mathrm{d}V_{\mathrm{core}} \tag{3.23}$$

and evaluated over the volumes as

$$W_{\mathrm{mag}} = \frac{1}{2} \frac{B_{\mathrm{gap}}^2}{\mu_0} A_{\mathrm{gap}} \, 2 \, l_{\mathrm{gap}} + \frac{1}{2} \frac{B_{\mathrm{core}}^2}{\mu_{\mathrm{core}}} A_{\mathrm{core}} \, l_{\mathrm{core}} \tag{3.24}$$

with the magnetic permeability of free space μ_0 and the core material magnetic permeability μ_{core}. The relation between the magnetic flux density B and the magnetic field strength H is

$$B = \mu H \tag{3.25}$$

and is assumed to be linear until the magnetic flux density B reaches the saturation maximum B_{sat}, see equation (3.31), [92, 104].

The magnetic flux

$$\Phi = \int_A B \, \mathrm{d}A \tag{3.26}$$

simplifies to $\Phi = A \cdot B$ for constant cross section areas. For the closed magnetic circuit, the magnetic flux is constant $\Phi = \Phi_{\mathrm{gap}} = \Phi_{\mathrm{core}}$ and with constant cross section areas $A = A_{\mathrm{gap}} = A_{\mathrm{core}}$ follows $B_{\mathrm{gap}} = B_{\mathrm{core}}$ which simplifies equation (3.24) to

$$W_{\mathrm{mag}} = \frac{1}{2} B^2 A \left(\frac{2\, l_{\mathrm{gap}}}{\mu_0} + \frac{l_{\mathrm{core}}}{\mu_{\mathrm{core}}} \right) \tag{3.27}$$

and with equation (3.21) the controlled brake force finally results in

$$F_{\mathrm{a}} = \frac{\mathrm{d}W_{\mathrm{mag}}}{\mathrm{d}l_{\mathrm{gap}}} = \frac{B^2 A}{\mu_0}. \tag{3.28}$$

The magnetic flux density B for an electromagnet with a coil with N_{c} windings and an applied current I can be calculated using the AMPÈRE'S circuital law

$$\Theta = I N_{\mathrm{c}} = \oint H \, \mathrm{d}l_{\mathrm{mag}} = H_{\mathrm{gap}} \, 2\, l_{\mathrm{gap}} + H_{\mathrm{core}} \, l_{\mathrm{core}} \tag{3.29}$$

with the magnetomotive force Θ and the closed integral over the magnetic field strength H along the closed path l_{mag} with piecewise constant magnetic field strength H_{gap} and H_{core}. With the relation from equation (3.25), the magnetomotive force simplifies to

$$I N_{\mathrm{c}} = B \left(\frac{2\, l_{\mathrm{gap}}}{\mu_0} + \frac{l_{\mathrm{core}}}{\mu_{\mathrm{core}}} \right), \tag{3.30}$$

which is rearranged to

$$B = \begin{cases} \dfrac{N_{\mathrm{c}} \, \mu_0 \, \mu_{\mathrm{core}}}{2\, l_{\mathrm{gap}} \mu_{\mathrm{core}} + l_{\mathrm{core}} \, \mu_0} \, I & \text{for } B < B_{\mathrm{sat}}, \\ B_{\mathrm{sat}} & \text{for } B \geq B_{\mathrm{sat}} \end{cases} \tag{3.31}$$

with the case analysis to incorporate the saturation behavior of the core material, [14, 104].

According to equation (3.28), the controlled brake forces can finally be stated as

$$F_{\mathrm{a}} = \frac{N_{\mathrm{c}}^2\,\mu_0\,\mu_{\mathrm{core}}^2 A}{\left(2\,l_{\mathrm{gap}}\mu_{\mathrm{core}} + l_{\mathrm{core}}\,\mu_0\right)^2}\,I^2. \tag{3.32}$$

The derived controlled brake force F_{a} is essentially responsible for the resulting friction force F_{f}, see equations (3.20) and (3.16), and is controlled by the applied current I and, hence, the control input voltage u_{a}, section 6.2.

3.2.3 Full model assembly

The previously introduced sub-models, i.e. the load-bearing structure in section 3.2.1 and the guidance elements, the friction model and the electromagnetic actuator in section 3.2.2, are assembled to a full system model, [56]. On the one hand, numerical simulations of the full system model are used to prove the concept of semi-active load redistribution. On the other hand, they are the basis to design an appropriate controller, chapter 6.

The state-space representation is an adequate formulation to mathematically connect different sub-models via their in- and outputs. A model can be represented in the state-space by transforming the model's nth-order differential equations into a first-order differential equation system with n equations, [86]. The model of the load-bearing structure is transformed into the state-space representation and equation (3.10) becomes

$$\dot{\boldsymbol{x}} = \underbrace{\begin{bmatrix} \mathbf{0} & \mathbf{I} \\ -\boldsymbol{M}^{-1}\boldsymbol{K} & -\boldsymbol{M}^{-1}\boldsymbol{D} \end{bmatrix}}_{\boldsymbol{A}\ [6\times6]}\boldsymbol{x} + \underbrace{\begin{bmatrix} \mathbf{0} \\ \boldsymbol{M}^{-1}\boldsymbol{B}_{\mathrm{a},0} \end{bmatrix}}_{\boldsymbol{B}_{\mathrm{a}}\ [6\times2]}\boldsymbol{u} + \underbrace{\begin{bmatrix} \mathbf{0} \\ \boldsymbol{M}^{-1}\boldsymbol{b}_{\mathrm{ext},0} \end{bmatrix}}_{\boldsymbol{b}_{\mathrm{ext}}\ [6\times1]}F. \tag{3.33}$$

The matrix dimensions are given in brackets. The matrix $\boldsymbol{A}$ is the $[6\times6]$ system matrix and $\boldsymbol{x}(t) \triangleq \boldsymbol{x} = [\boldsymbol{r}, \dot{\boldsymbol{r}}]^T$ is the $[6\times1]$ state vector with translational and angular displacement and velocity vectors as well as the $[2\times1]$ controlled input vector $\boldsymbol{u}(t) \triangleq \boldsymbol{u}$ according to (3.34). The zero and identity matrices $\mathbf{0}$ and $\mathbf{I}$ are of appropriate dimensions.

The guidance element forces $F_{\mathrm{ge,L}}$ and $F_{\mathrm{ge,R}}$ enable the load redistribution and result from equation (3.32), (3.20), and (3.16). They are summarized in the control input vector

$$\boldsymbol{u} = \begin{bmatrix} F_{\mathrm{ge,L}} \\ F_{\mathrm{ge,R}} \end{bmatrix}. \tag{3.34}$$

The controlled input vector $\boldsymbol{u}$ and the external excitation force F in equation (3.10) are allocated to the system by the [3×2] control input matrix and the [3×1] excitation input vector

$$\boldsymbol{B}_{\mathrm{a},0} = \begin{bmatrix} 1 & 1 \\ -1 & -1 \\ \frac{l_\mathrm{B}}{2} - a & -\frac{l_\mathrm{B}}{2} + a \end{bmatrix} \quad \text{and} \quad \boldsymbol{b}_{\mathrm{ext},0} = \begin{bmatrix} 1 \\ 0 \\ 0 \end{bmatrix}. \tag{3.35}$$

The output vector is defined as

$$\boldsymbol{y} = \underbrace{\begin{bmatrix} 0 & 0 & -\frac{l_\mathrm{B}}{2} + a & 0 & 0 & 0 \\ 0 & 0 & \frac{l_\mathrm{B}}{2} + a & 0 & 0 & 0 \\ 0 & 0 & 0 & 0 & 0 & -\frac{l_\mathrm{B}}{2} + a \\ 0 & 0 & 0 & 0 & 0 & \frac{l_\mathrm{B}}{2} + a \\ 0 & -1 & \frac{l_\mathrm{B}}{2} & 0 & 0 & 0 \\ 0 & 1 & \frac{l_\mathrm{B}}{2} & 0 & 0 & 0 \\ 0 & -k_\mathrm{L} & \frac{l_\mathrm{B}}{2} k_\mathrm{L} & 0 & -b_\mathrm{L} & \frac{l_\mathrm{B}}{2} b_\mathrm{L} \\ 0 & -k_\mathrm{R} & -\frac{l_\mathrm{B}}{2} k_\mathrm{R} & 0 & -b_\mathrm{R} & -\frac{l_\mathrm{B}}{2} b_\mathrm{R} \end{bmatrix}}_{\boldsymbol{C}\ [8\times6]} \boldsymbol{x} = \begin{bmatrix} z_{\Delta\mathrm{ge,L}} \\ z_{\Delta\mathrm{ge,R}} \\ \dot{z}_{\Delta\mathrm{ge,L}} \\ \dot{z}_{\Delta\mathrm{ge,R}} \\ z_\mathrm{L} \\ z_\mathrm{R} \\ F_\mathrm{L} \\ F_\mathrm{R} \end{bmatrix} \tag{3.36}$$

with the [8×6] output matrix $\boldsymbol{C}$. The output vector $\boldsymbol{y}$ contains the quantities that serve as input for the other sub-models, compare figure 3.9. The relative displacements $z_{\Delta\mathrm{ge,L/R}}$ and velocities $\dot{z}_{\Delta\mathrm{ge,L/R}}$ serve as input for equations (3.19) and (3.14), respectively. In short form, equations (3.33) and (3.36) become

$$\begin{aligned} \dot{\boldsymbol{x}} &= \boldsymbol{A}\,\boldsymbol{x} + \boldsymbol{B}_\mathrm{a}\,\boldsymbol{u} + \boldsymbol{b}_\mathrm{ext}\,F \\ \boldsymbol{y} &= \boldsymbol{C}\,\boldsymbol{x} \end{aligned} \tag{3.37}$$

representing the state space formulation of the open loop mathematical model for the load-bearing structure with the three degrees of freedom z_A, z_B and φ,

figure 3.4(a), and the guidance element forces $F_{\mathrm{ge,L/R}}$ based an the friction forces $F_{\mathrm{f,L/R}}$ (3.16) as well as the excitation force F (3.7).

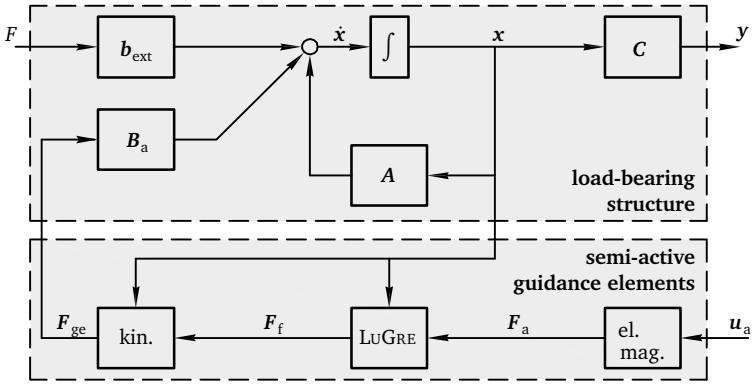

Figure 3.9: System overview block diagram combining all sub-models to the full open loop model, time dependence and L/R indication are omitted for readability

Figure 3.9 depicts the block diagram of the connected sub-models and their interaction for the open loop system without control. The upper gray box contains the physics representing the load-bearing structure consisting of two supports and the beam m_{B}, Θ_{B} and the mass m_{A} connected by the spring-damper. The lower gray box comprises the sub-models related to the semi-active guidance elements and provides the guidance element forces $F_{\mathrm{ge,L}}$ and $F_{\mathrm{ge,R}}$ to the load-bearing structure for the purpose of load redistribution when assumed to be operated in closed loop. By modeling the nonlinear guidance element forces $F_{\mathrm{ge,L}}$ and $F_{\mathrm{ge,R}}$ as inputs, the linear load-bearing structure's state space model and the nonlinear friction force calculation can be separated and the system is modular with advantages such as consecutive calibration of uncertain model parameters, see chapter 5.

The full model is used to predict the dynamic behavior of the load-bearing structure with emphasis on the beam's misalignment and the load path. The misalignment of the beam is represented by the angle φ or the displacement different of the supports $z_{\mathrm{R}} - z_{\mathrm{L}}$ according to equation (3.1). The load path of the load-bearing structure is represented by the support reaction forces F_{L} and F_{R} according to equation (3.6). Hence, the output vector $\boldsymbol{y}$ in equation (3.36) also contains the quantities z_{R}, z_{L}, F_{L} and F_{R}. In chapter 5, the uncertain model parameters are calibrated and the parameter uncertainty is quantified simultaneously. Subsequently,

the model is used to numerically tune the controllers for the different load redistribution strategies in simulation and experiment, see chapter 6, and to evaluate the load redistribution capability, see. chapter 7.

4 Experimental test setup

This chapter presents the experimental test setup of the simplified load-bearing structure from section 3.1 derived from the MAFDS introduced in figure 1.2. The physical load-bearing structure is presented in section 4.1. The semi-active guidance elements and the adjustable support are described in sections 4.2 and 4.3. Finally, section 4.4 presents the electrical components for signal processing and the measurement setup as well as the power amplifier for the electromagnetic actuators. The test setup is used for the experimental investigation of semi-active load redistribution for SHC with deliberate insertion of uncertainty in terms of changing support stiffness conditions in section 7.3.

4.1 Load-bearing structure

The experimental test setup of the load-bearing structure with semi-active guidance elements to investigate the ability of load redistribution with a semi-active approach is depicted in figure 4.1. The experimental test setup represents a simplification of the complex load-bearing system MAFDS, see section 3.1 and figure 3.1, but retains the main dynamic properties. These are the load transmission and distribution from one point of load application to multiple supports and a specified displacement trajectory of structural components, compare section 1.1 and figure 1.2. A spring-damper system determines the main kinetic properties. The specified displacement trajectory is enabled by kinematic guidance elements like torque links or other suspension links as an auxiliary structure that links two parts of a load-bearing structure for stability or guidance reasons.

For the experimental test setup of the load-bearing structure with semi-active guidance elements in figure 4.1, the mass (6) simplifies the lower truss of the MAFDS, compare figure 3.1, serves as point of load application and is connected to the beam (3) via the spring-damper (7) and the two semi-active guidance elements (8L) and (8R). Additionally, the mass (6) is guided by a rail mounted on the frame (11) and, thus, is enabled to move relative to the beam (3) in z-direction. The beam (3) with rectangular cross-section simplifies the upper truss of the MAFDS, compare figure 3.1. A step-like excitation force can be applied by releasing the

load mass ⑩ via an electromagnet ⑫ onto the mass ⑥. The load mass ⑩ is also guided by a rail mounted on the frame ⑪ and remains on the mass ⑥ after being released.

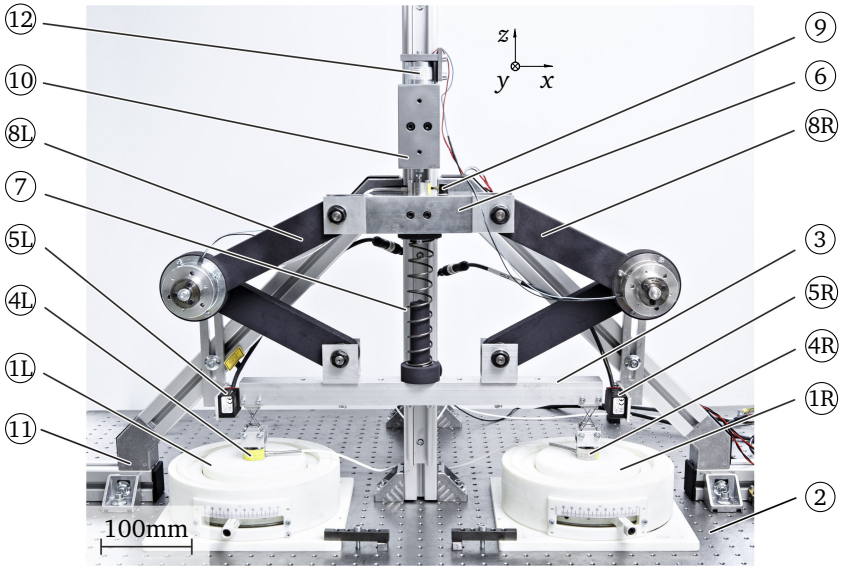

Figure 4.1: Experimental test setup with semi-active guidance elements for load redistribution and adjustable supports to simulate weak or damaged support conditions

The beam ③ is connected to two elastic supports ①L and ①R on the left and right side, that are mounted on a baseplate ②. The stiffness of the elastic supports can be varied to simulate structural damage or weakness and therewith to introduce uncertainty deliberately. For that, the flexible length of an elastic ring within the adjustable supports can be adjusted by turning a lever, see section 4.3 for details.

The acceleration $\ddot{z}_A$ of the mass ⑥ is measured by an accelerometer ⑨. Force and displacement sensors ④L, ④R and ⑤L, ⑤R measure the support reaction forces F_L and F_R and the displacements of the beam's ends z_L and z_R, compare figure 3.4(a) and equations (3.6) and (3.1). Both, the reaction forces and the displacements are used to evaluate the semi-active load redistribution capability in chapter 7 as introduced in section 3.1.

In case of normal, undamaged conditions and without semi-active means, the load path goes from the point of application at the mass (6) through the spring-damper (7) directly to the mid point of the beam (3). The beam (3) distributes the load to the elastic supports. In order not to influence the structure's load path, the beam's lateral bending stiffness in yz-plane is at least one order of magnitude higher than the support stiffness. Hence, the beam is assumed to be rigid. The semi-active guidance elements (8L) and (8R) fulfill only kinematic functions and enable a defined up-and-down trajectory of the connected structure parts beam (3) and mass (6). In this case, the load is equally distributed to both elastic supports (1L) and (1R) resulting in the predetermined load path (13), figure 4.2.

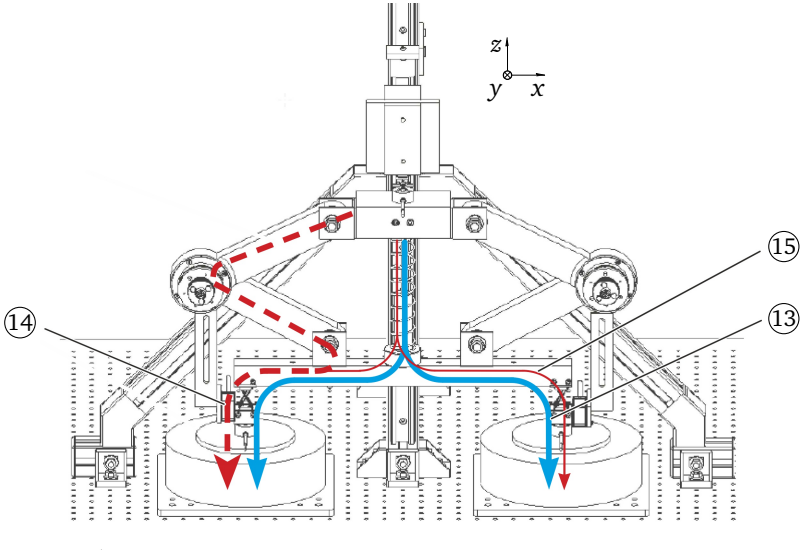

Figure 4.2: Schematic representation of the experimental test setup with semi-active guidance elements for load redistribution with predetermined and equally distributed load path (——), redistributed portion of the load path through the right guidance element (– –) and remaining portion of load path (——), compare figure 3.2

The load redistribution according to [42, 44, 45] and section 3.1 entails the redistribution of loads between the elastic supports (1L) and (1R) to change the predetermined load path (13). In this case, the semi-active guidance elements bear loads via an electromagnetic friction brake on the left or right side. In the scope of

this thesis, the deliberate reduction of the supports' stiffness simulates weakened or damaged supports, section 3.1. As example in figure 4.2, a damaged or weak support (1R) is relieved by using the semi-active guidance element (8L) as an additional load path (14) to the remaining load path (15) through the spring-damper (7). Proportions of the load can be bypassed through the guidance element (8L) directly to the undamaged support (1L). Table 4.1 lists the relevant specifications and mechanical components of the test setup.

Table 4.1: Specifications and mechanical components of the test setup

no.	qty.	description	type / material
(1L), (1R)	2	adjustable supports	Fraunhofer LBF, [53]
(2)	1	baseplate	Thorlabs® – B90120A
(3)	1	beam	aluminum EN AW-6060, square tube 30x30x2 mm
(4L), (4R)	2	load cell	Burster Typ 8435
(5L), (5R)	2	laser distance sensors	Micro-epsilon® – ILD 1420-50
(6)	1	mass	steel 1.4305
(7)	1	coil spring	Alb Federn Lothar Müller GmbH – spring 1881
(8L), (8R)	2	guidance element	see table 4.2
(9)	1	accelerometer	ids innomic® – KS95B.100
(10)	1	load mass	steel 1.4305
(11)	1	stiff frame structure with parallel guidance	Rexroth® – strut profiles and KWD-035
(12)	1	electromagnet	Magna-C® – 80055

4.2 Semi-active guidance element

Already existing components of the load-bearing structure, i.e. guidance elements, are augmented with electromagnetic friction brakes to a semi-active approach, section 2.1.2, for adapting the structure's load path via the friction moment M_f (3.20). Figure 4.3 depicts the semi-active guidance element used in the load-bearing structure of the test setup. The semi-active guidance element consists of two kinematic links (17)a and (17)b connected by a middle joint which is equipped with an electromagnetic friction brake (18). Ball bearings at the connection points (16)a and (16)b as

well as in the middle joint, see figure 4.4 (24), are reducing the uncontrolled friction and enable the desired displacement of the mass (6) relative to the beam (3), figure 4.1.

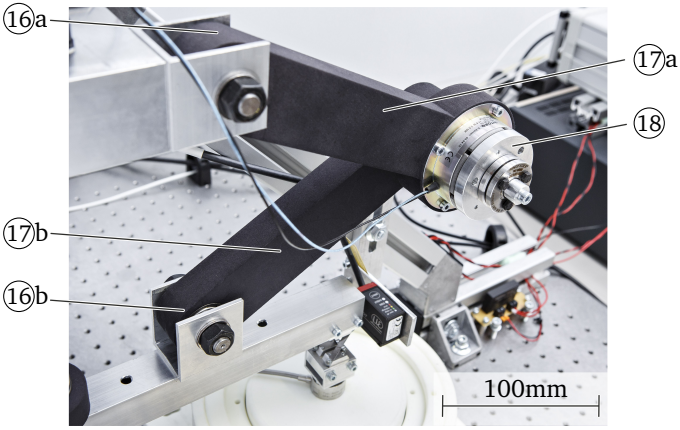

Figure 4.3: Semi-active guidance element (8R) used in the load-bearing structure

A detailed view to the inside of the middle joint including the electromagnetic friction brake is illustrated in figure 4.4. Basically, the electromagnetic friction brake provides a controllable friction force F_f (3.16) between the two kinematic links (17)a and (17)b.

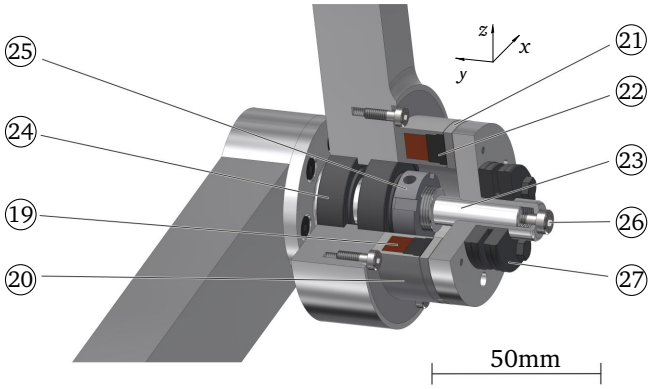

Figure 4.4: CAD section view of the semi-active guidance element with electromagnetic friction brake

In figure 4.4, the brake's coil (19) for inducing the electromagnetic force F_a, equation (3.32), and its housing, the stator (20), are mounted to the kinematic link (17)a. The brake lining (22) is mounted to the armature plate (21). The armature plate (21) is, in turn, mounted to the kinematic link (17)b by means of a shrink disc (27). The air gab between the stator (20) and the friction lining (22) is adjusted via the adjustment screw (26). Within the friction brake, the coil (19) induces the normal force onto the armature plate (21) comprising the friction lining (22) and, hence, the friction moment M_f (3.20) is generated. Table 4.2 lists the mechanical components of the semi-active guidance elements.

Table 4.2: Mechanical components of the semi-active guidance elements, the quantities are valid for two guidance elements

no.	qty.	description	type / material
(17)a	2	guidance element link male	polyamide PA2200
(17)b	2	guidance element link female	polyamide PA2200
(18)	2	electromagnetic friction brake incl. (19),(20),(21),(22)	INTORQ 14.115.06.1.2
(19)	2	coil	–
(20)	2	stator	–
(21)	2	armature plate	–
(22)	2	friction lining	–
(23)	2	axle	aluminum EN AW-7075
(24)	12	ball bearing	FAG 6003-2RSR
(25)	2	groove nut	DIN 981 KMK2, M15x1
(26)	2	air gab adjustment	DIN 6912 M5x16 screw and DIN 17222 disk springs
(27)	2	shrink disc	norelem 23380 type A

For the semi-active approach, the controlled force F_a (3.32), compare figure 3.8, acting on the friction lining can change the load transmitting properties of the semi-active guidance element by increasing or decreasing the friction moment M_f (3.20) in the joint. The semi-active guidance element partially take on load-bearing function when they generate friction forces or moments in the middle joints. In this case, they provide an additional load path, see figure 4.2, and load redistribution is possible.

4.3 Adjustable beam support to simulate damage

In the scope of this thesis, two adjustable supports (1L) and (1R) connect the load-bearing structure to the baseplate, figure 4.1. Typically, the support stiffness is predetermined and influences the structural dynamic behavior and the load path of the connected load-bearing structure substantially. In order to repeatable and measurable simulate structural damage or weakness of the supports, the support stiffness needs to be adjustable. This is the basis to experimentally investigate and evaluate the load redistribution capability in section 7.3. Therefore, adjustable supports (1L) and (1R) for the beam (3) as presented in [53] are used.

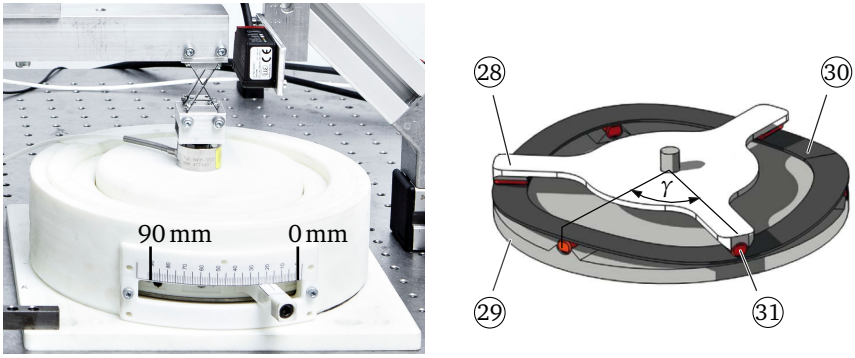

(a) **(b)**

Figure 4.5: Adjustable support (1R), **(a)** mounted to the test setup, scale in mm above lever to adjust stiffness according to table 4.3 and **(b)** concept of rotationally symmetric adjustable stiffness according to [53]

Figure 4.5(a) depicts one of the two adjustable supports used in the experimental test setup, section 4.1. The stiffness is adjusted via the lever position between 90 mm to 0 mm and varies between 70 N/mm to 5 N/mm, compare figure 4.6(a). Figure 4.5(b) depicts a schematic insight to the support and the principle concept to adjust the stiffness, [53]. The lower part of the adjustable support (29) is connected to the baseplate (2) and the upper part (28) is connected the beam (2). Between the two parts (28) and (29), there is an elastic ring (30). Basically, the elastic ring (30) represents a rotationally symmetric beam with adjustable flexible length. The flexible length is physically adjusted by changing the angle γ by means of the lever at (31) and the stiffness of the adjustable support results according to figure 4.6(a).

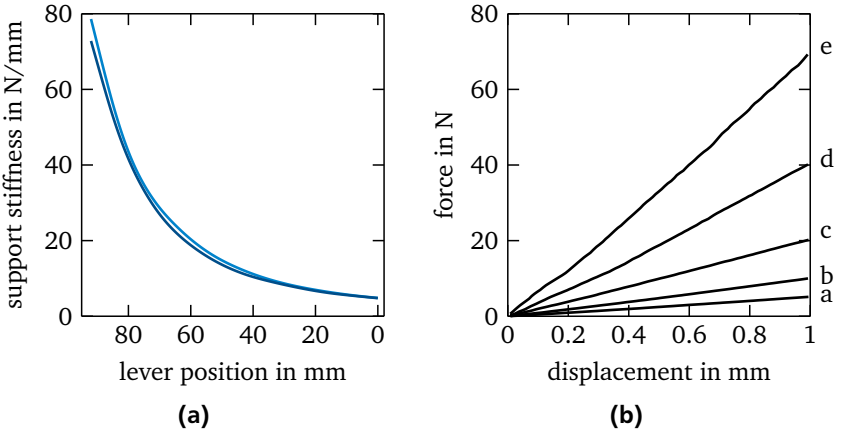

Figure 4.6: Adjustable support stiffness characteristic, **(a)** lever position, compare figure 4.5, and related stiffness of the adjustable supports (1L) (——) and (1R) (——), **(b)** quasi-linear force over displacement curves for selected lever positions with a = 5 N/mm, b = 10 N/mm, c = 20 N/mm, d = 40 N/mm, e = 70 N/mm

Figure 4.6(a) depicts the resulting stiffness of the adjustable support versus the lever position. The two adjustable supports (1L) and (1R) are characterized individually on a universal testing machine with measurable force and displacement, needed to calculate the stiffness. Figure 4.6(b) depicts the measured force over the stroke for several adjusted lever position and related stiffnesses. The relation between lever position and support stiffness is quadratic, figure 4.6(a), due to the principle concept to adjust the stiffness, see figure 4.5(b). Once a specific lever position with related support stiffness is set, the stiffness behavior itself is quasi-linear as designed, figure 4.6(b).

Table 4.3: Lever positions of the adjustable supports for selected stiffnesses according to the case study in section 7.1

	lever position in mm	
stiffness in N/mm	left (1L)	right (1R)
40	78.2	79.1
20	59.5	61.8
10	35.8	38.3

Table 4.3 lists three lever positions of the adjustable supports for selected stiffnesses according to the load redistribution case study in section 7.1. The selected stiffnesses represent an undamaged support with 40 N/mm, moderate damage with 50 % reduced stiffness and severe damage with 75 % reduced stiffness.

4.4 Data acquisition, signal processing and semi-active force induction

In this section, the electrical components for the data acquisition, the signal processing and the semi-active force induction to drive the electromagnetic brakes to realize semi-active load redistribution are presented. Figure 4.7 illustrates the signal processing from the data acquisition to the force induction for the investigated load-bearing structure, figure 4.1, with semi-active load redistribution for SHC.

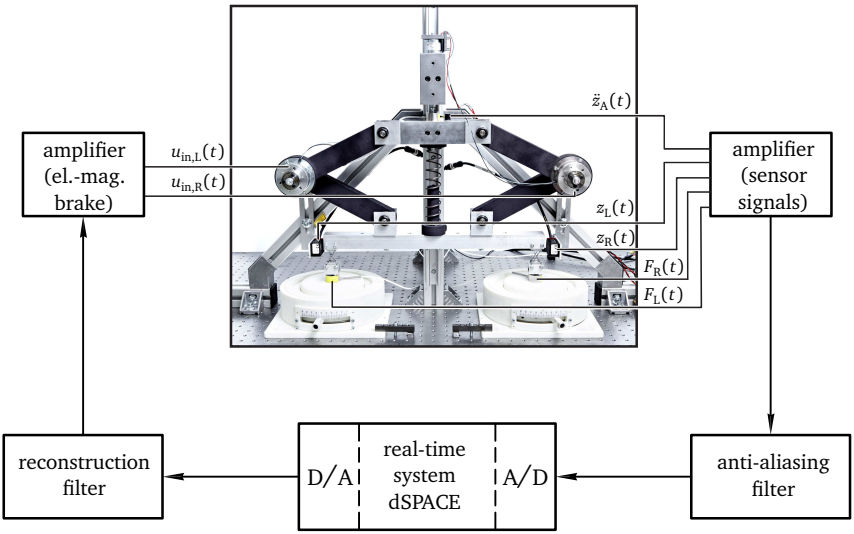

Figure 4.7: Signal processing and data aquisition in the load-bearing structure for semi-active load redistribution

The amplified voltages $u_{\mathrm{in,L/R}}$ that are applied to the electromagnetic brakes of the guidance elements (8L) and (8R) in figure 4.1 are used to control the load path through the load-bearing structure. The load path is represented by the support reaction forces $F_{\mathrm{L/R}}$ (3.6), compare section 3.1, measured by the two load cells (4L) and (4R) and the support displacements $z_{\mathrm{L/R}}$ (3.1) measured by the two laser sensors

(5L) and (5R). The acceleration $\ddot{z}_A$ of the mass (6) is measured via the accelerometer (9) to capture the motion of the mass (6) according to equation (3.8). The data acquisition and signal processing components are summarized in table 4.4.

Table 4.4: Electrical components of the experimental test setup

no.	qty.	description	type / material
–	1	real-time system	dSPACE® – DS1104
–	5	anit-aliasing filter	KEMO®BenchMaster 21M, 6 pole Elliptic type filter
–	2	reconstruction filter	KEMO®BenchMaster 21M, 6 pole Elliptic type filter
–	1	power amplifier for the el. mag. brakes	two channels frequency modulation based amplifier (proprietary development)
–	1	load cell amplifier	PEEKEL instruments PICAS

The data acquisition and the controller implementation are performed with the dSPACE® real-time system with a sampling frequency $f = 5\,000\,\text{Hz}$. For semi-active load redistribution control, the controllers from chapter 6 run on the real-time system with processing the measured sensor signals. The sensor signals $F_{L/R}$ from the load cells (4L) and (4R), $\ddot{z}_A$ from the accelerometer (9) and $z_{L/R}$ from the laser sensors (5L) and (5R) are amplified and filtered prior to the analog-digital conversion (A/D) and processing in the real-time system. All sensor signals are lowpass filtered by KEMO®BenchMaster 6th-order elliptic filters and a cutoff frequency $f_{cut} = 1\,500\,\text{Hz}$ for anti-aliasing. After digital-analog conversion (D/A), the real-time system output voltages are again lowpass filtered and smoothed by KEMO® BenchMaster 6th-order elliptic filters and a cutoff frequency $f_{cut} = 30\,000\,\text{Hz}$ as reconstruction filters. Finally, the outputs of the reconstruction filters are amplified by the power amplifiers before being applied to the electromagnetic friction brake in the guidance elements as $u_{in,L/R}$.

The power amplifier to operate the friction brakes is illustrated in figure 4.8, where figure 4.8(a) depicts the amplifier's components and figure 4.8(b) depicts the block diagram of its simplified electronic layout. The power amplifier provides two independent channels. The output voltage signals are modulated using pulse width modulation (PWM), [59]. PWM based power amplifiers can be used for

power delivery control, e.g. for DC-motors or as in the scope of this thesis for electromagnetic actuators used in the semi-active guidance elements.

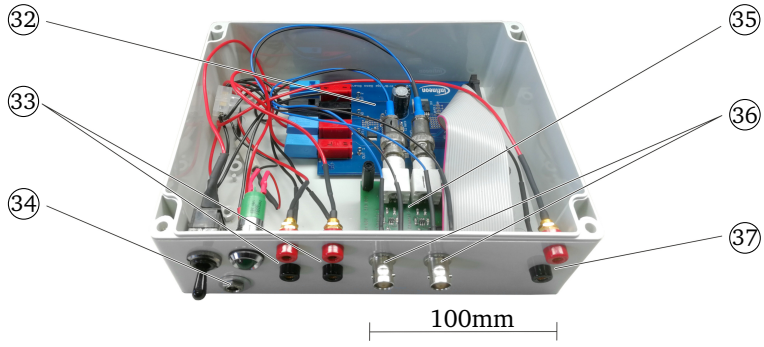

(a)

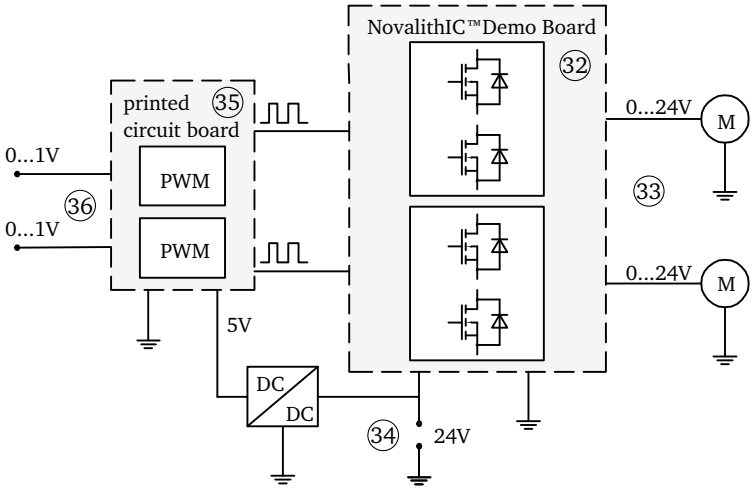

(b)

Figure 4.8: Two channel PWM based amplifier with analog voltage input and power output for the semi-active friction brake, **(a)** components of the amplifier and **(b)** simplified block diagram of the electronic layout

The power amplifier consists of metal-oxide-semiconductor field-effect transistor (MOSFET) amplifiers mounted on a Infineon Technologies NovalithIC™ Demo Board (32) that is connected to a printed circuit board (PCB) with two Linear Technology LTC6992-1 PWM integrated circuit modules (35). The two analog voltage inputs (36) for the two independent channels of the amplifier are connected to the dSPACE® real-time system with input signals in the range of 0 V to 1 V. These analog voltage inputs are transformed into two PWM signals via the two LTC6992-1 PWM integrated circuit modules on the PCB (35).

The PWM duty cycles are linearly based on the analog voltage input levels; 0 V results in 0 % duty cycle and 1 V results in 100 % duty cycle. The duty cycle defines the proportion of *on* time within a period of the PWM where the period is equal to $1/f_{\mathrm{PWM}}$ with the modulation frequency $f_{\mathrm{PWM}} = 20\,\mathrm{kHz}$, [59].

The PWM signals are fed into two MOSFET half-brights on the NovalithIC™Demo Board (32). The two power outputs (33) between 0 V to 24 V increase with increasing duty cycles of the PWM signals. Thus, the delivered power to the connected electrical loads M in figure 4.8(b), that represent the electromagnetic actuator of the friction brakes in the semi-active guidance elements, is controlled. Additionally, the electromagnet (12) to release the load mass (10) in figure 4.1 is connected to socket (37). The power is provided by a 50W AC/DC 24V power supply via the socket (34).

5 Model calibration

In this chapter, the mathematical model of the load-bearing structure with semi-active guidance elements from section 3.2 is calibrated. The non-deterministic model parameter calibration procedure to quantify and reduce model parameter uncertainty, compare section 2.2.1, is generally introduced in section 5.1. Since the dynamic behavior of the load-bearing structure with semi-active guidance elements is represented by the two model parts **load-bearing structure** and **semi-active guidance elements** in section 3.2, the following model parameter calibration is also separated into two parts. First, the load-bearing structure, section 5.2, and afterwards the semi-active guidance elements with the LuGre friction model are calibrated, section 5.3, utilizing the introduced model parameter calibration procedure.

5.1 Model calibration procedure

Mathematical models in engineering applications are typically used to predict the dynamic behavior of a structure or system in the time- or frequency domain. Once the model is derived and simplifications are made, values of model parameters are sometimes unknown or they cannot be defined in advance and, hence, represent data uncertainty according to section 2.2.1. Missing physics in a mathematical model such as the unknown existence of model parameters or unknown functional relations in the mathematical model represents model uncertainty, section 2.2.1, and is not considered in the scope of this thesis. Calibrating model parameters utilizing experimental data is necessary to adjust the mathematical model to the experimentally observed dynamic behavior and to achieve a reliable and adequate model prediction.

Figure 5.1 presents the procedure of statistic-based parameter inference applied in this thesis in a work flow diagram according to [7, 55]. Data uncertainty is quantified and reduced by applying this procedure, see section 2.2.2. Starting from a given mathematical model and an appropriate experimental setup at the top level, the calibration procedure is **initialized** by selecting the sub-models to be calibrated (or the whole model) and by assuming prior distributions for the

model parameters representing the model parameters' uncertainty. Subsequently, the calibration candidate parameters are **selected** based on their uncertainty and their sensitivity on the model prediction. Therefore, the comparative features that are the specific output responses used to compare the mathematical model predictions Y^{M} and the experimental results Y^{E}, need to be defined individually for each (sub-)model, e.g. in equations (5.9), (5.10) and (5.11). The comparative features represent the relevant outputs of the mathematical model or unambiguous physical properties and states to which the model is calibrate to, [7, 111]. Model parameters with negligible uncertainty or sensitivity will not be calibrated to reduce the computational effort. With the resulting reduced number of model parameters to be calibrated, the BAYESIAN inference is performed as the selected **calibration** approach according to section 2.3. BAYESIAN inference is a method to update a prior parameter distribution with new knowledge obtained from experimental data to a **posterior distribution** using the BAYES' THEOREM, [9, 106] and see paragraph BAYESIAN *inference parameter calibration*.

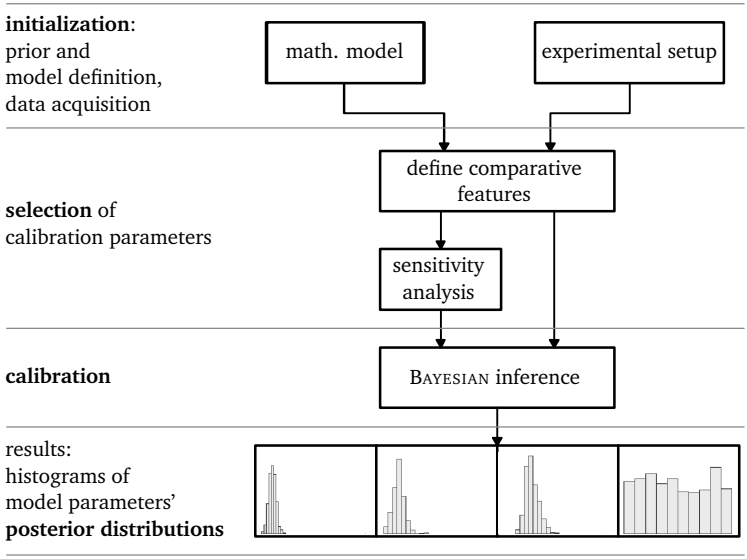

Figure 5.1: Flowchart of the model parameter calibration procedure

The following paragraphs describe the sensitivity analysis to identify the most influential model parameters and the calibration process of the identified model

parameters via BAYESIAN inference using the MARCOV CHAIN MONTE CARLO (MCMC) sampling algorithm to calculate the posterior distributions of these model parameters.

Sensitivity analysis with the coefficient of determination

The sensitivity of the mathematical model predictions on parameter variations is assessed by calculating the statistical significance of parameter variations on the model prediction variation. Thus, the influence of the model parameters with respect to the comparative features Y^{M} is identified. The assessment of the statistical significance is carried out with an analysis of variance (ANOVA) using the coefficient of determination R^2, [7, 100]. For that, a design of experiments (DOE) with L factor levels for P calibration candidate parameters θ_p with $p = 1, ..., P$ is utilized. The calibration candidate parameters θ_p are model parameters that are uncertain and probably contribute to the model prediction variation. In the scope of this thesis, the specific calibration candidate parameters of the load-bearing structure are defined in section 5.2.2 and of the semi-active guidance elements in section 5.3.2.

The coefficient of determination R^2 calculates the proportion of model output variability that can be ascribed to each calibration candidate parameter θ_p variation, the subscript p is omitted for better readability:

$$\mathrm{R}^2_\theta = 1 - \frac{\mathrm{SSE}_\theta}{\mathrm{SST}}. \tag{5.1}$$

The results for each calibration candidate parameter θ are $0 \leq \mathrm{R}^2_\theta \leq 1$. High R^2 values are used to identify the most influential model parameters. To obtain the coefficient of determination R^2_θ for each calibration candidate parameter θ, the total model variability, also called *sum of squares total* (SST)

$$\mathrm{SST} = \sum_{k=1}^{L^P} \left(Y_k^{\mathrm{M}} - \overline{Y}^{\mathrm{M}} \right)^2 \tag{5.2}$$

is calculated with the overall model output mean value $\overline{Y}^{\mathrm{M}}$ and sums up the variability of all P calibration candidate parameters θ in the L^P simulation evalua-

tions Y_k^{M}. The unexplained model variability of the calibration candidate parameter θ for which the R^2 value is calculated, also called *sum of squares error* (SSE)

$$\mathrm{SSE}_\theta = \sum_{l=1}^{L} \left(\sum_{j=1}^{L^{(P-1)}} \left(Y_{lj}^{\mathrm{M}} - \widehat{Y}_l^{\mathrm{M}} \right)^2 \right) \tag{5.3}$$

is calculated with the mean value $\widehat{Y}_l^{\mathrm{M}}$ and the $L^{(P-1)}$ simulation evaluations Y_{lj}^{M} with fixed level $l = \{1, \ldots, L\}$ of the calibration candidate parameter θ for which the R^2 value is calculated, [24].

For the calculation of the R_θ^2 values in sections 5.2 and 5.3, a two-level DOE with $L = 2$ is utilized with the lower and upper bounds of the parameters' prior distributions serving as factor levels, [7, 113]. The results are typically summarized in tables and a threshold is chosen that defines the minimum coefficient of determination R^2 value for being a calibration candidate, compare tables 5.2, 5.6 and 5.7.

By first using the sensitivity analysis, ill-conditioning can be prevented and computational burden reduced if only the most influential parameters are selected to be calibrated, [7]. If different experiments for the same mathematical model are available, it is also possible to allocate the experiments to the model parameters that can be calibrated with the measured data of the experiments as it is the case for the semi-active guidance elements, compare section 5.3.

BAYESIAN inference parameter calibration

In the scope of this thesis, the BAYESIAN inference based parameter calibration is applied to calibrate uncertain model parameters, [57, 63, 106]. The relation between measurements and simulations is given by

$$Y^{\mathrm{E}}(\boldsymbol{X}_n) = Y^{\mathrm{M}}(\boldsymbol{X}_n, \boldsymbol{\theta}) + \varepsilon(\boldsymbol{X}_n),\ n = 1, ..., N \tag{5.4}$$

where $Y^{\mathrm{E}}(\boldsymbol{X}_n)$ represents the nth experimentally measured comparative feature and N is the total number of measurements. The corresponding numerical simulation outputs of the mathematical model are represented by the comparative feature $Y^{\mathrm{M}}(\boldsymbol{X}_n, \boldsymbol{\theta})$ and supplemented by the measurement error $\varepsilon(\boldsymbol{X}_n) \sim \mathcal{N}(0, \sigma^2)$, that is assumed to be independent and identically distributed (iid) and normally distributed with zero mean and standard deviation σ, [106]. The controlled input $\boldsymbol{X}_n$ with the controlled parameters $X_{1,n}$, $X_{2,n}$ and $X_{3,n}$, see section 5.3, represent the nth measurement settings. The parameter vector $\boldsymbol{\theta}$ contains the model parameters

selected as calibration candidate parameters θ_p, see for the load-bearing structure section 5.2.2 and for the semi-active guidance elements section 5.3.2. The BAYESIAN inference approach statistically connects the simulation outputs Y^{M} as hypothesis and the measurement outputs Y^{E} by taking into account the hypothesis and measurement probability to adequately calibrate varied model parameters. Current knowledge of the system and its parameters is updated with new information obtained from experimental tests. Thus, the parameter uncertainty is quantified and reduced by systematic inference of the posterior distribution, [63, 106]. Using the BAYES' THEOREM, the posterior parameter distribution given the experimental results can be stated as

$$P(\boldsymbol{\theta}, Y^{\mathrm{M}}|Y^{\mathrm{E}}) = \frac{L(Y^{\mathrm{E}}|\boldsymbol{\theta}, Y^{\mathrm{M}}) \times P(\boldsymbol{\theta})}{P(Y^{\mathrm{E}})} \tag{5.5}$$

with the likelihood function

$$L(Y^{\mathrm{E}}|\boldsymbol{\theta}, Y^{\mathrm{M}}) = \prod_{n=1}^{N} \frac{1}{\sigma\sqrt{2\,\pi}} \exp\left(\frac{E_n(\boldsymbol{\theta})}{2\,\sigma^2}\right) \tag{5.6}$$

representing the probability of experimental outputs Y^{E} given a set of parameters $\boldsymbol{\theta}$ for the mathematical model output Y^{M}. The standard deviation σ is related to the measurement error $\varepsilon(\boldsymbol{X}_n)$ that is assumed to be normal distributed. In equation (5.6), the error function

$$E_n(\boldsymbol{\theta}) = \left(Y^{\mathrm{E}}(\boldsymbol{X}_n) - Y_n^{\mathrm{M}}(\boldsymbol{X}_n, \boldsymbol{\theta})\right)^2 \tag{5.7}$$

is chosen to be the square error between measurement and model output, [106]. If no further information regarding the prior distributions $P(\boldsymbol{\theta})$ in equation (5.5) is available, uniform distributions between certain upper and lower bounds are assumed, [7, 50].

The total probability or evidence $P(Y^{\mathrm{E}})$ in equation (5.5) is typically not computable with reasonable effort and is only normalizing the result anyway, [50]. Therefore, it is more practical to sample from a proportional relationship of the posterior parameter distribution

$$P(\boldsymbol{\theta}, Y^{\mathrm{M}}|Y^{\mathrm{E}}) \propto L(Y^{\mathrm{E}}|\boldsymbol{\theta}, Y^{\mathrm{M}}) \times P(\boldsymbol{\theta}). \tag{5.8}$$

In this thesis, the parameter space is explored with MCMC sampling to approximate the posterior parameter distributions $P(\boldsymbol{\theta}, Y^{\mathrm{M}}|Y^{\mathrm{E}})$ by drawing multiple samples

from these posterior parameter distributions. That is, the histograms of the calibration candidate parameters $\boldsymbol{\theta}$ of all random samples produce the approximated posterior parameter distributions $P(\boldsymbol{\theta}, Y^{\mathrm{M}}|Y^{\mathrm{E}})$, [80, 106].

Employing MCMC sampling, it is possible to eliminate the denominator $P(Y^{\mathrm{E}})$ in equation (5.5) and, thus, to enable a mathematical efficient application of BAYESIAN inference, [106]. The evolution of the MARKOV CHAIN represents the collections of samples from the calibration candidate parameter space containing the set of possible calibration candidate parameter values. A following chain element only depends on the current element and a proposal probability distribution that defines how the following chain element will be sampled based on the current element, see step 2 below. Each chain element represents a calibration candidate parameters realization. The MARKOV CHAIN has no memory and, hence, past elements are irrelevant to determine new elements from the parameter space. The MCMC sampling according to the METROPOLIS algorithm, [106], can be summarized in 6 steps:

1. Initialize parameters $\boldsymbol{\theta}_0$ to set chain start point

For $m = 1, ..., M$

2. Generate proposed parameters: $\boldsymbol{\theta}^* \sim \mathcal{N}(\boldsymbol{\theta}_{m-1}, \Delta\theta)$
3. Compute acceptance probability:

$$\alpha = \min\left(1, \frac{L(Y^{\mathrm{E}}|\boldsymbol{\theta}^*, Y^{\mathrm{M}}) \times P(\boldsymbol{\theta}^*)}{L(Y^{\mathrm{E}}|\boldsymbol{\theta}_{m-1}, Y^{\mathrm{M}}) \times P(\boldsymbol{\theta}_{m-1})}\right)$$

4. Sample from uniform distribution: $u_\alpha \sim \mathcal{U}(0, 1)$
5. Accept/Reject decision:

   if $u_\alpha < \alpha$: $\theta_m = \theta^*$

   else: $\theta_m = \theta_{m-1}$

End slope

6. Result: samples from the posterior $\boldsymbol{\theta}_0, ..., \boldsymbol{\theta}_M$

The number of chain elements is M and steps 2 to 5 iteratively recur M times. The proposal distribution $\mathcal{N}(\boldsymbol{\theta}_{m-1}, \Delta\theta)$ in step 2 is the probability of moving to a point in the parameter space and chosen to be GAUSSIAN with mean centered

at the current parameters $\boldsymbol{\theta}_{m-1}$ and variance given by $\Delta\theta$. The variance $\Delta\theta$ defines the dispersion and thereby the likely range of the proposal parameter. Hence, the variance $\Delta\theta$ defines how far the proposal parameters move from the current parameters. The acceptance probability is calculated in step 3 by dividing the posterior probability given the proposed parameters $\boldsymbol{\theta}^*$ with the posterior probability given the current parameters $\boldsymbol{\theta}_{m-1}$. Steps 4 and 5 provide the decision, if the proposed parameters $\boldsymbol{\theta}^*$ are accepted or the current parameters $\boldsymbol{\theta}_{m-1}$ are kept. Each result in step 6 is a sample of the posterior distributions and the histograms of the calibration candidate parameters for all samples represent the approximated posterior distributions, figure 5.1.

In this thesis, the mode, which is the most frequent sampled parameter value, is used as best estimate for parameter calibration. Additionally, the 95% interpercentile R_{95} of the posterior distribution, see section 2.2.2, is utilized to quantify the parameter uncertainty. The presented procedure with steps 1 to 6 is applied to the load-bearing structure in section 5.2.3 and the semi-active guidance elements in section 5.3.3.

5.2 Load-bearing structure

This section presents the model parameter calibration according to section 5.1 for the load-bearing structure in figure 3.4(a). Following the flowchart in figure 5.1, first the experimental data used for the calibration of the load-bearing structure are introduced. Then, the most influential model parameters are selected according to their sensitivity on the comparative features and finally used for BAYESIAN inference parameter calibration.

5.2.1 Experimental data for calibration purpose

The experimental and numerical outputs of interest for the model parameter calibration of the load-bearing structure and to derive the comparative features, see equation (5.9), are the support reaction forces F_{L} and F_{R} according to equation (3.36) representing the load path through the load-bearing structure. The measured support reaction forces F_{L} and F_{R} to calibrate the model parameters of the load-bearing structure are obtained from the experimental test setup introduced in chapter 4. The experimental test setup is operated in passive configuration without using the semi-active guidance elements for load redistribution. However, the electromagnetic friction brakes are mounted to the structure. Additionally, the system is assumed to be undamaged with equal support stiffnesses.

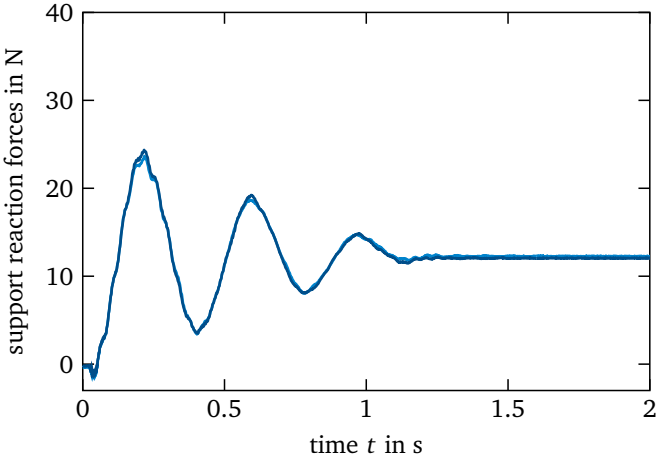

Figure 5.2: Measurements of the support reaction forces F_L(——) left and F_R(——) right representing the structures' load path to calibrate the load-bearing structure for a step-like excitation with $F = 25\,\mathrm{N}$

Figure 5.2 depicts the measured support reaction forces F_L and F_R average for 10 measurement repetitions. The structure is excited by a step load of $F = 25\,\mathrm{N}$ introduced by the load mass, see figure 4.1. Both support reaction forces F_L and F_R are approximately equal and, hence, the load path is evenly split to the supports as expected.

5.2.2 Parameter selection for calibration

The model parameters that need to be calibrated must be selected based upon both their uncertainty and sensitivity, see section 5.1. The parameter uncertainty might result from missing manufacturer information, non-measurable model parameters resulting from simplifications or empirical models with non-physical parameters. With knowledge regarding the previously described uncertainty sources and a subsequent sensitivity analysis, the most influential calibration parameters are selected following the procedure of the flow chart in figure 5.1.

Table 5.1 introduces all model parameters to simulate the dynamic behavior of the load-bearing structure in passive configuration. The model parameters related to the adjustable supports are not calibrated because they are investigated

separately in section 4.3 and can be measured. The beam length l_B can also be measured and the stiffness coefficient k_S is given by the manufacturer. Therefore, these model parameters are kept constant and are not subject for parameter calibration since their uncertainty is assumed to be small compared to the calibration candidate parameters in table 5.1. The beam's moment of inertia Θ_B directly results from the beam's cross section geometry and its mass m_B and, therefore, is no individual calibration candidate.

Table 5.1: Model parameters of the load-bearing structure, parameters with stated values are not subject for calibration, calibration candidate parameters are referenced to table 5.2 and table 5.3

property	symbol	value	unit
support properties			
stiffness support left	k_L	30,000	N/m
stiffness support right	k_R	30,000	N/m
structure properties			
mass	m_A	table 5.3	kg
beam mass	m_B	table 5.2	kg
beam moment of inertia	Θ_B	0.0417	$\mathrm{kg\,m^2}$
viscous damping coefficient	b_S	table 5.3	Ns/m
friction damping	F_μ	table 5.3	N
stiffness coefficient	k_S	1440	N/m
beam length	l_B	0.4	m

The damping related model parameters F_μ and b_S are typically uncertain parameters and not to determine without experiments, [78]. Technically, the masses m_A and m_B are measurable. Since the guidance elements are assumed to be free of mass, it is reasonable to allot their amount of mass to the masses m_A and m_B. However, the quantitative allocation to the masses m_A and m_B is uncertain. Therefore, the parameters F_μ, b_S, m_A and m_B become calibration candidates. The sensitivity of these parameters, all related to the structure properties, is calculated according to section 5.1 using comparative features. In the following, the comparative feature to calibrate the load-bearing structure is

$$Y^{M/E}(t, \boldsymbol{\theta}) = \frac{1}{2}\left(F_L(t) + F_R(t)\right), \tag{5.9}$$

representing the time-history of the average support reaction force. In case of equal support stiffness of the left and right support, the numerically calculated support reaction forces are equal, as the experimental results, see figure 5.2. Hence, there is no need to calibrate both sides individually and the average support reaction force is chosen as comparative feature (5.9).

The R^2 sensitivity analysis results according to equation (5.1) are listed in table 5.2 for each calibration candidate parameter, averaged over simulation time $t = 0\,\mathrm{s}$ to $t = 2\,\mathrm{s}$ since the comparative feature $Y^{\mathrm{M}}(t, \boldsymbol{\theta})$ (5.9) is time dependent. The lower bounds for the mass m_{A} and the beam mass m_{B} results from their measured weights. The upper bounds are chosen with additional 2 kg considering the potential mass of the assumed to be free mass guidance elements, see section 3.2. The upper and lower bounds for b_{S} and F_{μ} are best guesses, which result from preliminary numerical tests. The model parameters m_{A}, m_{B}, b_{S} and F_{μ} are assumed to be equal distributed between their lower and upper bounds. A significant proportion of variability of Y^{M} according to equation (5.9) with 73.04% is explained by the mass m_{A}. Another 7.68% and 19.20% of variability are explained by the viscous damping coefficient b_{S} and the friction damping F_{μ}. Thus, these parameters are calibrated with experimental data. The beam mass m_{B} contributes less than 1% to the variability of Y^{M} and is not calibrated with experimental data.

Table 5.2: R^2 statistics for the calibration candidate parameters and the parameter bounds for the sensitivity analysis of the load-bearing structure, R^2 values are scaled to 100 %

parameter	lower bound	upper bound	R^2	calibrate?
m_{A}	1.4 kg	3.4 kg	73.04 %	Yes
m_{B}	0.25 kg	2.25 kg	0.17 %	No
b_{S}	$5.0\,\mathrm{N\,s\,m^{-1}}$	$10.0\,\mathrm{N\,s\,m^{-1}}$	7.68 %	Yes
F_{μ}	0.8 N	1.6 N	19.20 %	Yes

Only parameter with significant influence on the output variability ($R^2 > 1\%$) are taken into account for the following calibration process. The calibration parameters are summarized in the calibration parameter vector $\boldsymbol{\theta} = \left[m_{\mathrm{A}}, b_{\mathrm{S}}, F_{\mu}\right]$ and are reduced from 9 model parameters in table 5.1 to 3 calibration parameters to be calibrated via BAYESIAN inference with MCMC.

5.2.3 BAYESIAN parameter inference and uncertainty quantification

In the previous section 5.2.2, the sensitive and relevant parameters of the load-bearing structure for calibration were identified based on foreknowledge and sensitivity analysis. The BAYESIAN inference according to equation (5.4) to (5.8) with MCMC according to the 6 steps on page 60 is applied to these parameters for calibration and uncertainty quantification purpose, section 5.1 and figure 5.1. The prior distributions $P(\boldsymbol{\theta})$ for each parameter in $\boldsymbol{\theta}$ are assumed to be uniform between lower and upper bounds according to table 5.2. This is common in case no further information is available, [7]. The posterior distribution $P(\boldsymbol{\theta}, Y^{\mathrm{M}}|Y^{\mathrm{E}})$ is formulated according to equation (5.8) and sampled with $M = 25\,000$ MCMC runs. The results are depicted in figure 5.3.

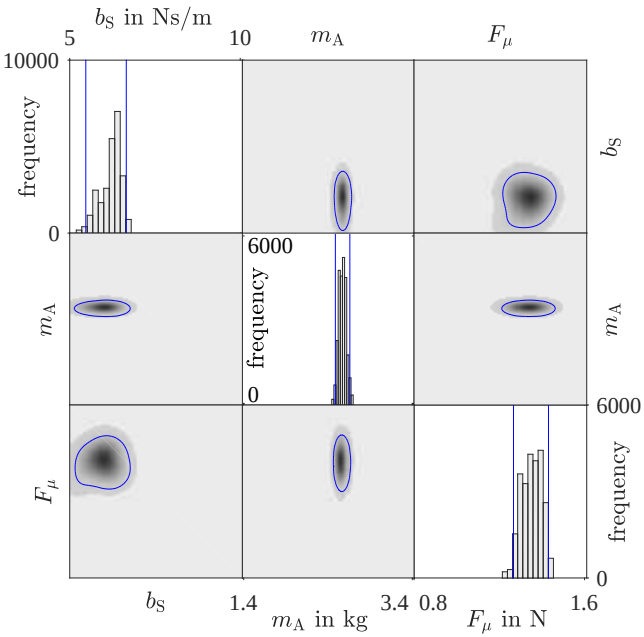

Figure 5.3: Posterior distribution with 95% interpercentile intervals (——) on the diagonals and bivariate joint distributions with 95% contour (⬭) on the off-diagonals for the viscous damping b_{S}, the mass m_{A} and the friction induced force F_{μ}; calculated with code based on [37, 84]

In figure 5.3 on the diagonal, the parameter distributions are shown as histograms representing the posterior approximations by the MCMC samples with indicated 95% interpercentile intervals. The abscissas' limits are given by the model parameters' prior bounds. The off-diagonals depict distribution contour plots for the bivariate joint probability distribution pairs of the parameters indicating interactions between each pair of parameters. Furthermore, the narrow histograms on the diagonal graphically depict the knowledge gain and the uncertainty reduction for the parameter ranges when comparing the prior parameter bounds and the posterior 95% interpercentile ranges. The parameter ranges covering the 95% interpercentile and indicating the parameter uncertainty can be reduced about 88% for the mass m_A, about 83% for the viscous damping b_S and about 84% for the dissipative force F_μ compared to the prior bounds. The modes, see section 2.2.2, of the calibrated parameters are $m_A = 2.6\,\mathrm{kg}$, $b_S = 6.1\,\mathrm{N\,s\,m^{-1}}$ and $F_\mu = 1.35\,\mathrm{N}$. Table 5.3 summarizes the prior and posterior uncertainty in form of bounds and 95% interpercentiles.

Table 5.3: Prior and posterior uncertainty in form of bounds and 95 % interpercentiles of the calibration parameters

	prior bounds		posterior 95 % interpercentile	
parameter	lower bound	upper bound	lower bound	upper bound
m_A	$1.4\,\mathrm{kg}$	$3.4\,\mathrm{kg}$	$2.51\,\mathrm{kg}$	$2.73\,\mathrm{kg}$
b_S	$5.0\,\mathrm{N\,s\,m^{-1}}$	$10.0\,\mathrm{N\,s\,m^{-1}}$	$5.47\,\mathrm{N\,s\,m^{-1}}$	$6.35\,\mathrm{N\,s\,m^{-1}}$
F_μ	$0.8\,\mathrm{N}$	$1.6\,\mathrm{N}$	$1.26\,\mathrm{N}$	$1.39\,\mathrm{N}$

The effect of the calibrated parameters on the model prediction accuracy is exemplarily shown in figure 5.4 for a step load excitation $F = 25\,\mathrm{N}$ (3.7) applied to the load-bearing structure in figure 3.4 and figure 4.1, respectively. The envelopes of each 300 MC simulation runs for non-calibrated ( ) and calibrated ( ) parameter ranges are conducted and compared to the related support reaction force measurements F_L (——) and F_R (——) from figure 5.2. The quantity of 300 MC simulation runs is enough to emphasize the difference between model predictions with non-calibrated and calibrated model parameters. As assumed for the parameter selection in section 5.2.2, the non-calibrated model parameter ranges are equal distributed between the lower and upper prior bounds in table 5.2. The calibrated

model parameter ranges are distributed according to the histograms on the diagonal in figure 5.4 with the 95% interpercentiles in table 5.3. For the MC simulations in figure 5.4, the values of the model parameters, which are not selected for calibration, are assumed to be deterministic and chosen as the mean value of the upper and lower bounds in table 5.3 or according to table 5.1. The simulations using calibrated model parameters tend to be closer to the measurement with smaller envelopes. Even though the envelopes of calibrated and non-calibrated simulations widely encompass the measurements for both supports, the envelope area of the calibrated MC simulations is significantly reduced by 75% compared to the envelope area of the non-calibrated MC simulations.

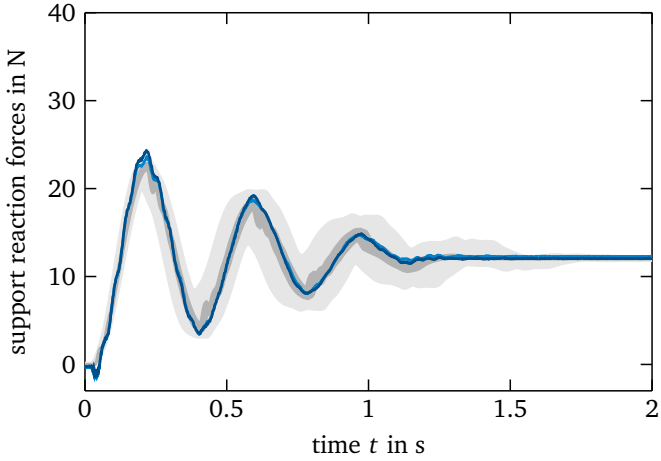

Figure 5.4: Measured support reaction force F_L (—) and F_R (—) vs. time t and model predictions non-calibrated ( ) and calibrated ( )

5.3 Semi-active guidance elements

This section presents the model parameter calibration according to section 5.1 for the semi-active guidance elements in figure 3.5(a). Following the flowchart in figure 5.1, first the experimental data used for the model parameter calibration of the semi-active guidance elements are introduced for two cases with different experiments to capture the different friction regimes, see section 3.2.2. Then, the most influential model parameters are selected according to their sensitivity on the two comparative features for each case and finally used for BAYESIAN parameter calibration.

5.3.1 Experimental data acquisition for model calibration

The experimental and numerical outputs of interest for the model parameter calibration of the semi-active guidance elements and to derive the comparative features in equation (5.10) and (5.11) are the guidance element force F_{ge} and the machine displacement Δz_{ge} according to equations (3.15) and (3.12). The measured guidance element force F_{ge} and machine displacement Δz_{ge} to calibrate the model parameters of the semi-active guidance elements are obtained by means of an universal testing machine (UTM). The UTM applies a controlled force or displacement at a predefined velocity to the mounted semi-active guidance elements, [46].

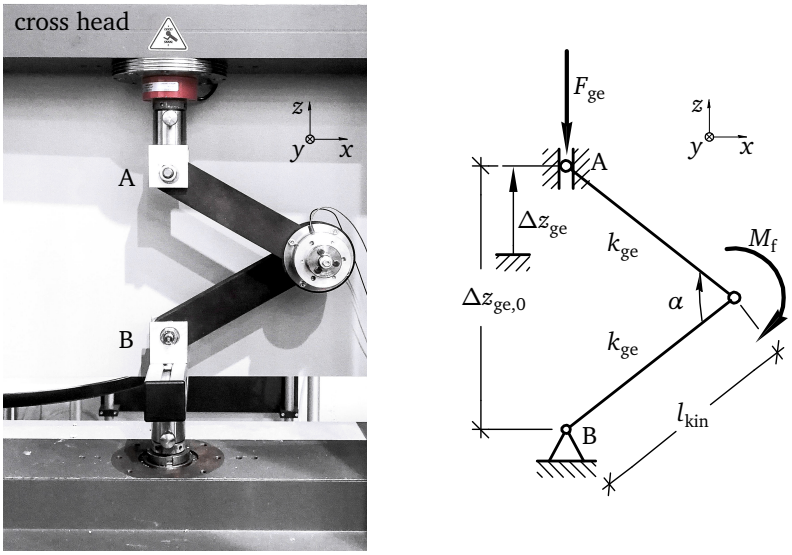

(a) **(b)**

Figure 5.5: Experimental data acquisition for the semi-active guidance elements: **(a)** UTM with semi-active guidance element and **(b)** mechanical concept of the UTM with semi-active guidance element, [46]

Figure 5.5 depicts the UTM with one mounted semi-active guidance element and the mechanical concept of the test setup. Even though the right semi-active

guidance elements is illustrated in figure 5.5(a), the findings in this section are valid for both sides left and right. For better readability, the subscripts L/R indicating left and right are omitted in this section. The mechanical concept is depicted in figure 5.5(b). The two kinematic links of the guidance element, see figure 4.3, are described by the length l_{kin} and the stiffness k_{ge} in z-direction, compare figure 3.5. The dependence of the stiffness k_{ge} on the angle α of the two kinematic links is neglected since only relatively small changes in α are expected. The initial distance between the connection points A and B in figure 5.5(b) is $\Delta z_{\mathrm{ge},0}$. The simplified 1-dimensional model with two degrees of freedom Δz_{ge} representing the machine displacement in z-direction, and z_α representing the displacement at the friction surfaces in z-direction, is similar to figure 3.5(c). The displacement at the friction surfaces z_α results from the angle between the kinematic links α according to equation (3.11). The guidance element force F_{ge} is applied by the UTM and measured by a load cell mounted between the guidance element's upper connection point A and the UTM's movable cross head, figure 5.5(a). The displacement Δz_{ge} is related to the UTM's movable cross head position and measured by the position sensor inside the motor moving the cross head. It is possible to perform experiments with controlled guidance element force F_{ge}, displacement Δz_{ge} and velocity $\Delta \dot{z}_{\mathrm{ge}}$.

As introduced in section 3.2.2 for the semi-active guidance element's model, the friction force F_{f} can be controlled via the electromagnetic normal force F_{a} according to equation (3.20) and equation (3.32). The electromagnetic normal force F_{a}, however, is induced by the voltage input u_{in} in the range 0 V to 24 V applied to the electromagnetic friction brake, figure 4.4. The voltage input u_{in} is provided by a laboratory power supply and, thus, limited to 0 V to 12 V for the experiments with the UTM. The voltage levels are kept constant during each experiment.

The LuGre friction model significantly contributes to the numerically simulated dynamic behavior of the semi-active guidance elements, section 5.3.2. The individual LuGre parameters describe different friction behavior, [38]. Therefore, two cases I and II with different experiments are conducted with the previously described experimental setup in figure 5.5, [4]. Case I is conducted in macro-slip scale for low velocity displacement cycles; case II is conducted in micro-slip scale using a presliding regime force cycles. Both cases I and II have different control parameters X_p. Control parameters represent the parameters that are varied in a controlled manner within predefined levels during the measurement campaign to cover the desired range of experiments. For the following cases I and II, the controlled parameters are the velocity $X_1 \mathrel{\widehat{=}} \Delta \dot{z}_{\mathrm{ge}}$, the voltage $X_2 \mathrel{\widehat{=}} u_{\mathrm{in}}$ and the maximum guidance element force $X_3 \mathrel{\widehat{=}} F_{\mathrm{ge,max}}$.

Table 5.4: Summary of control parameters and quantities of interest (QoI), [46]

experiment		controlled parameter	QoI
case I:	low velocity displacement cycle, macro-slip scale	X_1: velocity $\Delta\dot{z}_{\mathrm{ge}}$ X_2: voltage u_{in}	F_{ge}
case II:	preslide regime force cycle, micro-slip scale	X_3: max. force $F_{\mathrm{ge,max}}$	Δz_{ge}

The control parameters X_1,X_2 and X_3 are chosen since they are compatible with the UTM, i.e. X_1,X_3, and mainly responsible for the resulting friction force F_{f} in the semi-active guidance elements i.e. X_2. Table 5.4 summarizes the two cases I and II, their control parameters and the quantities of interest (QoI) F_{ge} and Δz_{ge}.

Case I: low velocity displacement cycle, macro-slip scale

In case I, a displacement controlled low velocity displacement cycle is applied by moving the UTM's cross head in z-direction. The displacement cycle starts at an initial distance of $\Delta z_{\mathrm{ge}}(t{=}0\,\mathrm{s}) = \Delta z_{\mathrm{ge},0} = 205\,\mathrm{mm}$, to $\Delta z_{\mathrm{ge}}(t_{\mathrm{half}}) = 125\,\mathrm{mm}$ and ends again at $\Delta z_{\mathrm{ge}}(t_{\mathrm{end}}) = \Delta z_{\mathrm{ge},0} = 205\,\mathrm{mm}$. The control parameters in case I are the velocity X_1 and the voltage X_2. The velocity X_1 is varied in three levels $X_1 = [80, 1000, 2000]\,\mathrm{mm/min}$ and the voltage X_2 is varied in 6 levels $X_2 = [2, 4, 6, 8, 10, 12]\,\mathrm{V}$. The levels are chosen to cover a wide range of possible application while keeping the experimental effort manageable. The time period for one cycle t_{end} depends on the velocities in X_1. The control parameter X_1 defines how fast the connection points A and B in figure 5.5 are moving relative to each other. With the controlled parameter X_2, the electromagnetic normal force F_{a} and thereby the friction force F_{f} can be varied according to equations (3.32) to (3.16). Hence, these two control parameters influence the measured machine force F_{ge} as the output of interest.

Figure 5.6 depicts the measurements for case I as part of the experimental data to calibrate the semi-active guidance elements. The measured machine force F_{ge} vs. time t is illustrated in figure 5.6(a) and vs. the controlled displacement Δz_{ge} in figure 5.6(b), each for three different exemplary voltage levels $X_2 = [4, 8, 12]\,\mathrm{V}$ and one representative velocity $X_1 = 2000\,\mathrm{mm/min}$. The measured machine force F_{ge} increases with increasing voltage level X_2. The sign of the machine force F_{ge} depends on the moving direction of the UTM's cross head.

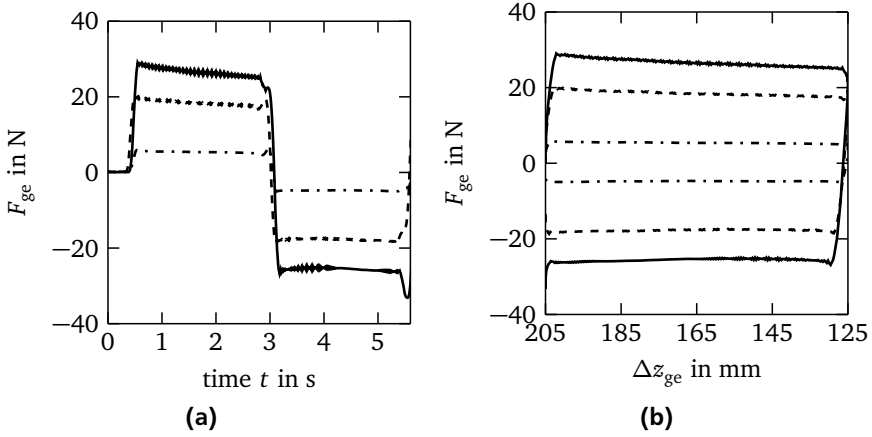

Figure 5.6: Measured machine force F_{ge} according to case I, exemplary for $X_1 = 2000\,\text{mm/min}$ and $X_2 = 4\,\text{V}$ (−·−), $8\,\text{V}$ (− −), and $12\,\text{V}$ (——) for one displacement cycle each **(a)** vs. time t and **(b)** vs. displacement Δz_{ge}, [46]

Case II: presliding regime force cycle, micro-slip scale

In case II, the guidance element is operated only in preslide regime which means that only micro slip and elastic deformation occur with displacements $\Delta z_{ge} \ll 1\,\text{mm}$ around $\Delta z_{ge,0}$. The electromagnetic brake in the guidance element is locked, meaning that the maximum possible friction force is higher than the actual guidance element force, $F_{f,max} > F_{ge}$ and stiction is present. A controlled machine force cycle is applied by pushing the UTM's cross head in z-direction according to figure 5.5. The load cycle for F_{ge} starts at an initial machine force $F_{ge} = F_{ge,0} = 0\,\text{N}$, increases to $F_{ge} = F_{ge,max}$, and ends again at $F_{ge,end} = 0\,\text{N}$. The control parameter is the maximum machine force X_3 and it is varied in five levels $X_3 = [4, 6, 8, 10, 12]\,\text{N}$. The levels are chosen to cover a wide range of possible application while keeping the experimental effort manageable. The controlled parameter X_3 influences the measured displacement Δz_{ge} in preslide regime. Preslide displacement occurs if stiction is present and a displacement is only possible because of elasticities between the interacting surfaces due to the bristle assumption in figure 3.7(c), superposed by elasticities of the flexible guidance element links k_{ge}, see figure 3.5, [46].

Figure 5.7 depicts the measurements for case II as part of the experimental data to calibrate the semi-active guidance elements. The displacement Δz_{ge} vs. time t is illustrated in figure 5.7(a) and vs. the controlled guidance element force F_{ge} in figure 5.7(b), each for three different exemplary maximum guidance element forces $X_3 = [4, 8, 12]\,\mathrm{N}$ and constant quasi static velocity $\Delta \dot{z}_{\mathrm{ge}} \approx 0\,\mathrm{m/s}$. The measured displacement Δz_{ge} increases linearly with increasing controlled guidance element force F_{ge}. The max. guidance element force X_3 determines the maximum displacement $\Delta z_{\mathrm{ge,max}}$.

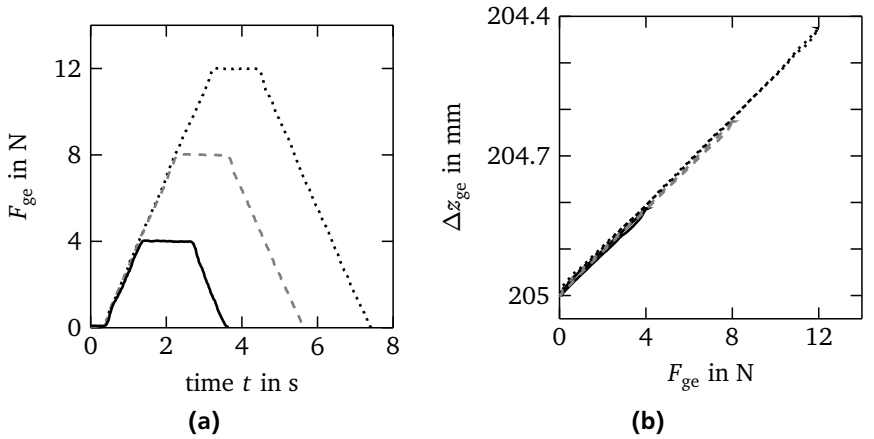

Figure 5.7: Measurements with blocked friction brake according to case II, exemplary for controlled machine forces $F_{\mathrm{ge,max}} = 4\,\mathrm{N}$ (——), $8\,\mathrm{N}$ (– –), and $12\,\mathrm{N}$ (- - -) **(a)** vs. time t and **(b)** preslide displacement Δz_{ge} vs. the exemplary controlled machine force F_{ge}, [46]

The introduced measurements for case I and II are used to derive the individual comparative features in the following section 5.3.2 and eventually to calibrate the model parameters of the semi-active guidance elements in section 5.3.3.

5.3.2 Parameter selection for calibration

The model parameters of the semi-active guidance element that need to be calibrated must be selected based upon both their uncertainty and sensitivity, see section 5.1 and figure 5.1. As in section 5.2.2, the parameter uncertainty might

result from missing manufacturer information, non-measurable model parameters resulting from simplifications or empirical models with non-physical parameters. Friction models, in this thesis in particular the LuGre model in section 3.2, need special attention because friction model parameters are typically a source of uncertainty, since they result from simplification and empirical modeling, [13, 18].

Table 5.5: Model parameters for semi-active guidance elements with electromagnetic friction brake, parameters with stated values are not subject for calibration, calibration candidate parameters are referenced to tables 5.6, 5.7 and 5.8

property	symbol	value	unit
geometric properties			
guidance element link length	l_{kin}	0.2	m
contact point	a	0.1	m
guidance element stiffness	k_{ge}	table 5.8	N/m
friction properties			
LuGre bristle stiffness	σ_0	table 5.8	m^{-1}
LuGre bristle damping	σ_1	tables 5.6, 5.7	s/m
LuGre viscous damping	σ_2	table 5.8	s/m
LuGre dynamic friction coefficient	μ_{d}	table 5.8	–
LuGre static friction coefficient	μ_{s}	tables 5.6, 5.7	–
LuGre Stribeck velocity	v_{S}	tables 5.6, 5.7	m/s
electromagnetic properties			
coil average radius	r_{c}	$2.4 \cdot 10^{-2}$	m
coil length	l_{c}	$8 \cdot 10^{-3}$	m
coil windings	N_{c}	450	–
coil inductance	L_{c}	$1.54 \cdot 10^{-2}$	H
coil resistance	R_{c}	50	Ω
magnetic circuit length in iron	l_{core}	0.124	m
area of magnetic flux	A_{core}	$3.244 \cdot 10^{-4}$	m^2

Table 5.5 introduces all model parameters related to the semi-active guidance elements. The model parameters related to the electromagnetic properties are not calibrated. These parameters are associated with the electromagnetic friction brake, see table 4.1 and figure 4.4, and are declared by the manufacturer or can be measured. The length l_{kin} of a guidance element link and the contact point distance a can also be measured directly. Therefore, these model parameters are

kept constant and are not subject for model parameter calibration since their uncertainty is assumed to be small compared to the calibration candidate parameters in table 5.5.

The friction properties in table 5.5 containing the LuGre friction model parameters are typically uncertain model parameters and cannot be observed directly. Additionally, the uncertain LuGre parameters are strongly dependent on the case of application, the actual system and the surface materials. Hence, the LuGre parameter values vary widely in literature, e.g. [17, 23, 38, 40, 89], leading to the lower and upper bounds for the R^2 sensitivity analysis results in tables 5.6 and 5.7. Additionally, the guidance element stiffness k_{ge} is unknown and, hence, assigned to the list of parameters to be calibrated with the experiments introduced in this section 5.3. The sensitivity of the LuGre parameters $\sigma_0, \sigma_1, \sigma_2, \mu_{\mathrm{s}}, \mu_{\mathrm{d}}, \nu_{\mathrm{S}}$ and the guidance element stiffness k_{ge} is calculated according to section 5.1 and equation (5.1) using individual comparative features for each case I and II. In the following, two individual comparative features $Y_{\mathrm{I}}^{\mathrm{M/E}}$ and $Y_{\mathrm{II}}^{\mathrm{M/E}}$ are introduced for each case I and II.

For case I, the high dimensionality of the time-history measurement of the guidance element force F_{ge} is reduced to a single value quantity of the work W_{ge} done by the guidance element force F_{ge} in one displacement cycle, thereby reducing the computational demand for the following model calibration procedure. The work W_{ge} done by the guidance element force F_{ge} in one displacement cycle represents the first comparative feature

$$Y_{\mathrm{I}}^{\mathrm{M/E}}(\boldsymbol{X}_n): \quad W_{\mathrm{ge}}(\boldsymbol{X}_n) = \int_{\Delta z_{\mathrm{ge},0}}^{\Delta z_{\mathrm{ge,end}}} F_{\mathrm{ge}}(\boldsymbol{X}_n)\,\mathrm{d}\Delta z_{\mathrm{ge}} \tag{5.10}$$

with dependency on the controlled parameters $\boldsymbol{X} = (X_1, X_2)_n$ of the nth measurement, compare equation (5.4) and table 5.4. The guidance element force F_{ge} is induced by the guidance element friction force F_{f}, as derived in equations (3.15), (3.16) and (3.20). Therefore, it is a suitable feature to infer the LuGre parameters, [46].

For case II, the maximum preslide displacement

$$Y_{\mathrm{II}}^{\mathrm{M/E}}(\boldsymbol{X}_n): \quad \Delta z_{\mathrm{ge,max}}(\boldsymbol{X}_n) = \max(\Delta z_{\mathrm{ge}}) \tag{5.11}$$

is the second comparative feature for calibration with dependency on controlled parameter $\boldsymbol{X}_n = X_{3,n}$ of the nth measurement. Both comparative features Y_{I} and Y_{II} are obtained from the experimental data $Y_{\mathrm{I}}^{\mathrm{E}}$ and $Y_{\mathrm{II}}^{\mathrm{E}}$, and the numerical simulations of the model $Y_{\mathrm{I}}^{\mathrm{M}}$ and $Y_{\mathrm{II}}^{\mathrm{M}}$ introduced in section 5.3.1 and section 3.2.2.

The R^2 sensitivity analysis results for case I according to equation (5.1) are listed in table 5.6 for each calibration candidate parameter, averaged for the min-max level combinations of the control parameter X_1 and X_2. A significant proportion of variability of $Y_{\mathrm{I}}^{\mathrm{M}}$ with 98.87% are explained by the viscous damping σ_2 and the dynamic friction coefficient μ_{s}. Thus, they are calibrated with experimental data obtained from case I. All the other parameters contribute less than 1% to the variability of $Y_{\mathrm{I}}^{\mathrm{M}}$ and are not subject for calibration with experimental data obtained from case I.

Table 5.6: R^2 statistics for the calibration candidate parameters and the parameter bounds for the sensitivity analysis for case I, R^2 values are scaled to 100 %, [46]

name	lower bound	upper bound	$\mathrm{R}^2_{\theta_p}$	calibrate?
σ_0	$1\,000\,\mathrm{m}^{-1}$	$100\,000\,\mathrm{m}^{-1}$	0.51 %	No
σ_1	$12.5\,\mathrm{s\,m}^{-1}$	$37.5\,\mathrm{s\,m}^{-1}$	0.08 %	No
σ_2	$0\,\mathrm{s\,m}^{-1}$	$5\,\mathrm{s\,m}^{-1}$	34.12 %	Yes
μ_{d}	0.3	0.9	64.75 %	Yes
μ_{s}	0.375	1.125	0.16 %	No
v_{S}	$5 \cdot 10^{-4}\,\mathrm{m\,s}^{-1}$	$1.5 \cdot 10^{-3}\,\mathrm{m\,s}^{-1}$	0.01 %	No
k_{ge}	$12\,000\,\mathrm{N\,m}^{-1}$	$43\,000\,\mathrm{N\,m}^{-1}$	0.37 %	No

The R^2 sensitivity analysis results for case II according to equation (5.1) are listed in table 5.7 for each calibration candidate parameter, averaged for min-max levels of the control parameter X_3. Almost the entire variability of $Y_{\mathrm{II}}^{\mathrm{M}}$ with $\mathrm{R}^2 = 99.99\%$ is associated with the bristle stiffness σ_0 and the guidance element stiffness k_{ge}. Thus, they are calibrated with experimental data obtained from case II. Compared to the guidance element stiffness k_{ge}, the bristle stiffness σ_0 is still small but with $\mathrm{R}^2 > 1\%$ it is reasonable to keep it for calibration. All the other parameters do not significantly contribute to the variability of $Y_{\mathrm{II}}^{\mathrm{M}}$ and are not subject for calibration with experimental data obtained from case II.

Table 5.7: R^2 statistics for the calibration candidate parameters and the parameter bounds for the sensitivity analysis for case II, R^2 values are scaled to 100 %, [46]

name	lower bound	upper bound	$R^2_{\theta_p}$	calibrate?
σ_0	$1\,000\,\mathrm{m}^{-1}$	$100\,000\,\mathrm{m}^{-1}$	2.96 %	Yes
σ_1	$12.5\,\mathrm{s\,m}^{-1}$	$37.5\,\mathrm{s\,m}^{-1}$	0.00 %	No
σ_2	$0\,\mathrm{s\,m}^{-1}$	$5\,\mathrm{s\,m}^{-1}$	0.00 %	No
μ_d	0.3	0.9	0.00 %	No
μ_s	0.375	1.125	0.01 %	No
v_S	$5 \cdot 10^{-4}\,\mathrm{m\,s}^{-1}$	$1.5 \cdot 10^{-3}\,\mathrm{m\,s}^{-1}$	0.00 %	No
k_ge	$12\,000\,\mathrm{N\,m}^{-1}$	$43\,000\,\mathrm{N\,m}^{-1}$	97.03 %	Yes

For the following BAYESIAN inference parameter calibration, the viscous damping σ_2 and the dynamic friction coefficient μ_s are calibrated with experimental data obtained from case I. The bristle stiffness σ_0 and the guidance element stiffness k_ge are calibrated with experimental data obtained from case II. This allocates the dynamic LUGRE parameters, see section 3.2.2, with macro-slip (case I) and the static LUGRE parameters with micro-slip (case II) experiments, which is consistent with the findings in [38]. The calibration parameters are summarized in the calibration parameter vector $\boldsymbol{\theta} = \left[\sigma_0, \sigma_2, \mu_\mathrm{s}, k_\mathrm{ge}\right]$ and are reduced from 16 parameters in table 5.5 to 4 calibration parameters to be calibrated via BAYESIAN inference with MCMC. The calibration candidate parameters, which are not selected for calibration, are chosen to be the mean value of the upper and lower bounds in table 5.6 and 5.7 for following numerical investigations.

5.3.3 BAYESIAN parameter inference and uncertainty quantification

In section 5.3.2 the sensitive and relevant parameters of the semi-active guidance elements for calibration were chosen based on foreknowledge and sensitivity analysis, tables 5.6 and 5.7. The BAYESIAN inference according to equation (5.4) to (5.8) with MCMC according to the 6 steps on page 60 is applied to these parameters for calibration and uncertainty quantification purpose, section 5.1 and figure 5.1. The prior distributions $P(\boldsymbol{\theta})$ in equation (5.5) for each parameter in $\boldsymbol{\theta}$ are assumed to

be uniform between the lower and upper bounds according to tables 5.6 and 5.7. This is common in case no further information is available, [7]. The posterior distribution $P(\boldsymbol{\theta}, Y^{\mathrm{M}}|Y^{\mathrm{E}})$ is formulated according to equation (5.8) and sampled with $M = 25\,000$ MCMC runs.

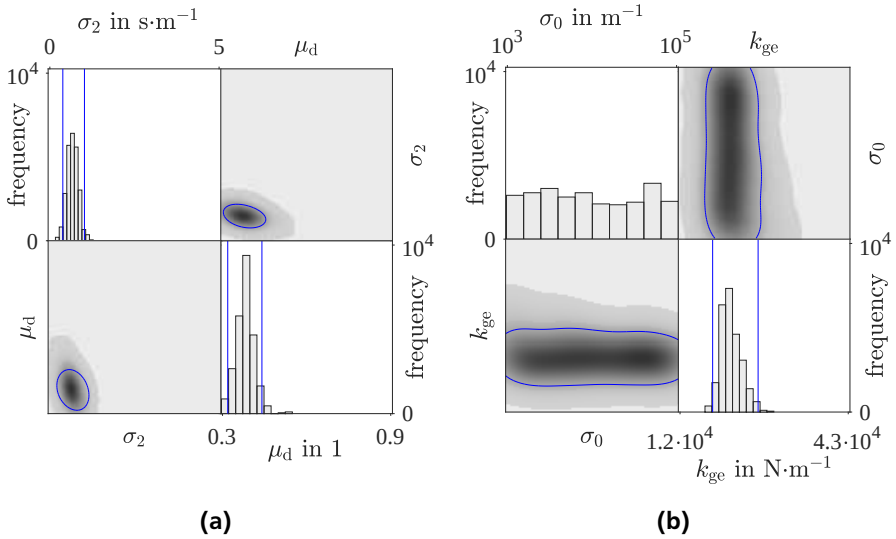

Figure 5.8: Posterior distribution with 95% interpercentile intervals (——) on the diagonals and bivariate joint distributions with 95% contour (⬭) on the off-diagonals for **(a)** case I the viscous damping σ_2 and the dynamic friction coefficient μ_{d} and **(b)** case II the bristle stiffness σ_0 and the guidance element stiffness k_{GE}, [46]; calculated with code based on [37, 84]

Figure 5.8 depicts the inferred results for the calibrated parameters σ_0, σ_2, μ_{s} and k_{ge} analogue to figure 5.3. On the diagonals, the parameter distributions are shown as histograms representing the posterior approximation by the MCMC samples with indicated 95% interpercentile intervals. The abscissas' limits are given by the model parameters' prior bounds. The off-diagonals depict distribution contour plots for the bivariate joint probability distribution pairs of the parameters indicating interactions between each pair of parameters.

The results for case I are shown in figure 5.8(a). For the viscous damping σ_2 and the dynamic friction coefficient μ_{d}, the likely parameter ranges that covers the 95% interpercentile intervals can be reduced by about 87% and by about 79%

compared to the parameters' prior bounds. The narrow histograms for the viscous damping σ_2 and the dynamic friction coefficient μ_d graphically depict the knowledge gain and the uncertainty reduction for the parameter ranges when comparing the prior parameter bounds and the posterior 95% interpercentile ranges.

The results for case II are shown in figure 5.8(b). For the guidance element stiffness k_{GE}, the likely parameter range that covers the 95 % interpercentile interval can be reduced by about 76 % compared to the parameters' prior bounds. The narrow histogram for the guidance element stiffness k_{GE} graphically depicts the knowledge gain and the uncertainty reduction for the parameter range when comparing the prior parameter bounds and the posterior 95% interpercentile range. For the bristle stiffness σ_0, the results are vague and the likely parameter range that covers the 95 % interpercentile interval can not be reduced. A possible reason for the unsuccessful calibration of the bristle stiffness σ_0 could be the fact that both parameters guidance element stiffness k_{GE} and bristle stiffness σ_0 represent stiffnesses that are connected in series. Presumably, the effective stiffness is dominated by the guidance element stiffness k_{GE} and, therefore, only k_{GE} can be calibrated successfully. This is consistent with the R^2 analysis results in table 5.7 for case II, showing significantly higher sensitivity values for the guidance element stiffness k_{GE} compared to the bristle stiffness σ_0.

Starting with an assumed uniform distribution, the parameter ranges and thus the uncertainty for the guidance element stiffness k_{GE}, the viscous damping σ_2 and the dynamic friction coefficient μ_d are reduced significantly. The reduction of parameter uncertainty is indicated by the reduced 95% interpercentile intervals compared to the parameters' prior bounds. The BAYESIAN inference results in figure 5.8 provide a best estimation, i.e. the modes, see section 2.2.2, in combination with the related uncertainty in form of histograms. The modes of the calibrated parameters are $\sigma_2 = 0.7\,\mathrm{s\,m^{-1}}$, $\mu_d = 0.29$ and $k_{ge} = 23\,275\,\mathrm{N\,m^{-1}}$. The calibration parameter σ_0 with vague calibration results is chosen to be the mean value of the upper and lower bounds in table 5.6 or 5.7 for the following numerical investigations in figure 5.9 and section 7.2, as it is the case for the calibration candidate parameters, which are not subject for calibration.

Table 5.8 summarizes the BAYESIAN inference results and provides the calibration candidate prior bounds and the 95% interpercentile intervals after parameter calibration. With respect to the chosen features $Y_I^{M/E}$ in equation (5.10) and $Y_{II}^{M/E}$ in equation (5.11) and the control parameters X_1, X_2 and X_3, it is possible to calibrate 2 out of 6 LUGRE parameters, the viscous damping σ_2 and the dynamic friction coefficient μ_d, as well as the structure parameter guidance element stiffness k_{GE}.

Table 5.8: Prior and posterior uncertainty in form of bounds and 95 % interpercentile intervals of the calibration parameters, [46]

	prior bounds		posterior 95 % interpercentile	
parameter	lower bound	upper bound	lower bound	upper bound
σ_0	$1\,000\,\mathrm{m}^{-1}$	$100\,000\,\mathrm{m}^{-1}$	–	–
σ_2	$0\,\mathrm{s\,m}^{-1}$	$5\,\mathrm{s\,m}^{-1}$	$0.388\,\mathrm{s\,m}^{-1}$	$1.034\,\mathrm{s\,m}^{-1}$
μ_d	0.3	0.9	0.242	0.338
k_ge	$12\,000\,\mathrm{N\,m}^{-1}$	$43\,000\,\mathrm{N\,m}^{-1}$	$19\,758\,\mathrm{N\,m}^{-1}$	$28\,550\,\mathrm{N\,m}^{-1}$

The effect of the calibrated parameters on the model prediction accuracy of the semi-active guidance element model is exemplarily shown in figure 5.9 providing measured (——) guidance element force F_ge as well as non-calibrated ( ) and calibrated ( ) simulation results as well as for case I, section 5.3.1.

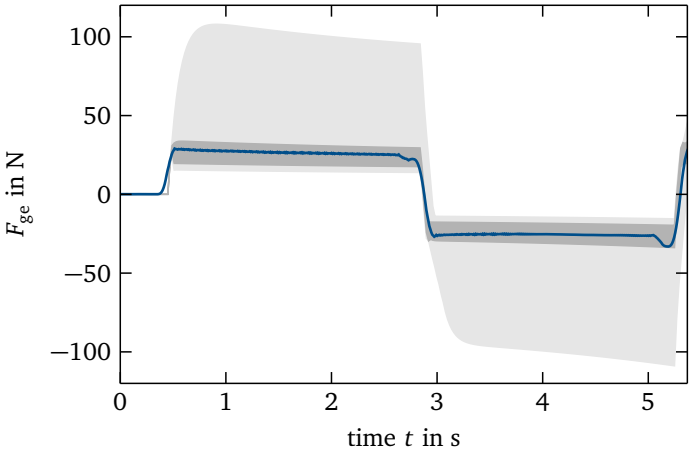

Figure 5.9: Guidance element force F_ge for $X_1 = 2\,000\,\mathrm{mm/min}$ and $X_2 = 12\,\mathrm{V}$ vs. time t, measured (——), non-calibrated ( ) and calibrated ( ) simulations of case I, compare figure 5.6(a)

For figure 5.9, the guidance element force F_ge during one displacement cycle is calculated for a fixed machine velocity and voltage levels at $X_1 = 2\,000\,\mathrm{mm/min}$ and $X_2 = 8\,\mathrm{V}$, compare figure 5.6(a). The envelopes of each 300 MC simulation runs for non-calibrated and calibrated parameter ranges are conducted and

compared to the related guidance element force measurement F_{ge} (——). The quantity of 300 MC simulation runs is enough to emphasize the difference between model predictions with non-calibrated and calibrated model parameters. As assumed for the parameter selection in section 5.3.2, the non-calibrated model parameter ranges are equal distributed between the lower and upper prior bounds in table 5.6. The calibrated model parameter ranges are distributed according to the histograms on the diagonals in figure 5.8 with the 95% interpercentiles in table 5.8. For the MC simulations in figure 5.9, the values of the model parameters, which are not selected for calibration or with no success in calibration, are assumed to be deterministic and chosen as the mean value of the upper and lower bounds in tables 5.6 and 5.7 or according to table 5.5. The simulations using calibrated model parameters tend to be closer to the measurement with smaller envelopes. Even though calibrated and non-calibrated simulation envelopes encompass the measurements of the guidance element force F_{ge}, the envelope area of the calibrated MC simulations is significantly reduced by about 85% compared to the envelope area of the non-calibrated MC simulations.

5.4 Summary and discussion of results

The model calibration is conducted for the two model parts load-bearing structure and semi-active guidance elements. For the load-bearing structure model, 3 of 4 calibration candidate parameters can be calibrated with uncertainty reduction from 82% to 84%. For the semi-active guidance element model, 3 of 7 calibration candidate parameters can be calibrated with uncertainty reduction from 76% to 87%.

The calibration candidate parameters for each model part are selected from all model parameters based on availability of information and related uncertainty. Additionally, a variance-based sensitivity analysis using the coefficient of determination R^2 is conducted to identify the most influential model parameters as calibration candidate parameters. Subsequently to the parameter selection, the BAYESIAN inference parameter calibration is performed. This approach correlates the model predictions with the experimental data statistically by solving an inverse problem. The experimental data for the model parameter calibration are obtained from the experimental test setup of the load-bearing structure and the UTM with a mounted semi-active guidance element. The calibration parameters uncertainty is reduced and simultaneously quantified by systematic inference of the posterior distribution using the BAYES' THEOREM. The posterior parameter distributions are approximated with MCMC sampling. When applying MCMC sampling, calibration

parameters with similar physical meaning, e.g. the two different kinds of damping b_S and F_μ, require careful choice of parameter starting points and proposal distribution for the evolution of the MARKOV CHAIN. Eventually, histograms quantify the uncertainty for each calibrated parameter. The quantified parameter uncertainty is valid with respect to the related mathematical (sub-)model.

Applying the calibrated model parameters in the models for numerical simulations, the model prediction uncertainty due to model parameter uncertainty is reduced by up to 56% for load-bearing structure simulations and by up to 85% for LUGRE model friction simulations.

6 Load redistribution control

This chapter specifies the load redistribution control for SHC as a semi-active approach to control uncertainty in a load-bearing structure. Uncertainty during operation of load-bearing structures may arise from damage or wear of supports, section 3.1, and leads to e.g. structural misalignment φ that is defined as malfunctions, section 3.2.1, or an inappropriate load path with the associated inappropriate support reaction forces F_{L} and F_{R}, section 2.2. These two possible malfunctions yield two control strategies with different control objectives. For both control strategies, potentially suitable controller are presented and compared, section 6.1. Finally, a controller for each strategy is selected and designed for numerical and experimental application of the semi-active load redistribution, section 6.2.

6.1 Control strategies for semi-active load redistribution

Load redistribution within the load-bearing structure means shifting load between the supports during operation, section 3.1. A damaged or weak support can be relieved by using the semi-active guidance elements as an additional load path. A support can also be relieved or loaded to achieve a load ratio among the two supports departing from the predetermined load ratio. For these two objectives of load redistribution control, the two control strategies I and II are defined and investigated.

6.1.1 Control strategy I: Misalignment reduction

Figure 6.1 depicts the schematic illustration of control strategy I for misalignment reduction. The controller calculates the output voltages $u_{\mathrm{a,L/R}}(t) \triangleq u_{\mathrm{a,L/R}}$ that are amplified and fed back to the load-bearing structure and induce the semi-active moment $M_{\mathrm{f,L/R}}$ (3.20) according to the detected misalignment $e_{\mathrm{I}}(t) \triangleq e_{\mathrm{I}}$ (6.1). By applying the semi-active moment $M_{\mathrm{f,L/R}}$, the misalignment e_{I} is reduced and the damaged support is relieved.

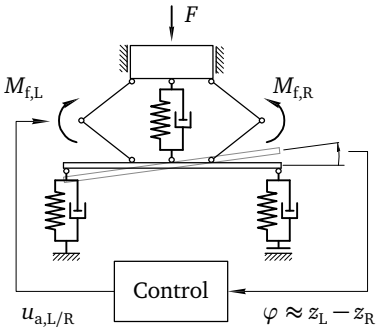

Figure 6.1: Schematic illustration of the load redistribution control strategy I: misalignment reduction

Load redistribution with control strategy I is used to reduce the structural misalignment φ resulting from decreased support stiffness of a weakened or damaged support. Control strategy I is applied if undesired displacements in form of misalignments are critical and when damage has already occurred. Redistributing the load away from the support with reduced stiffness towards the support with original stiffness reduces misalignment and, thus, undesired displacements. The time-dependent control deviation of control strategy I

$$e_I = z_L - z_R \stackrel{!}{=} 0 \tag{6.1}$$

represents the actual beam misalignment as difference of the support displacements z_L and z_R according to equation (3.1) and should be zero. The support displacements z_L and z_R for the numerical investigations are obtained from the mathematical model of the semi-active load-bearing structure according to equation (3.37) and for the experimental investigations are measured with laser-based displacement sensors, figure 4.1. Therefore, the misalignment is defined by the support displacement difference $z_L - z_R$ instead of the beam angle φ, see figure 3.4(a) and equation (3.1). The support displacement difference $z_L - z_R$ is almost identical to the beam angle φ, apart from a geometric constant, and is also easier to determine in measurements.

6.1.2 Control strategy II: Defined load ratio

Figure 6.2 depicts the schematic illustration of control strategy II for a defined load ratio. The controller calculates output voltages $u_{a,L/R}$ that are amplified and fed

back to the load-bearing structure and induce the semi-active moment $M_{\mathrm{f,L/R}}$ (3.20) according to the detected deviation from the defined load ratio $e_{\mathrm{II}}(t) \triangleq e_{\mathrm{II}}$ (6.2). By applying the semi-active moment $M_{\mathrm{f,L/R}}$, the load path and the support reaction force ratio are changed as specified.

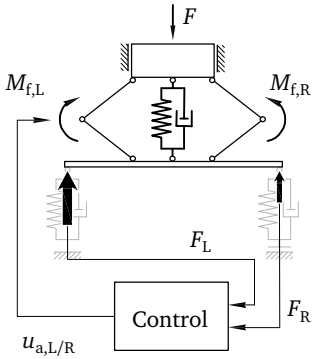

Figure 6.2: Schematic illustration of the load redistribution control strategy II: defined load split ratio

Load redistribution with control strategy II is used to achieve a defined load ratio between the support reaction forces F_{L} and F_{R} by shifting the load from one support towards the other. Both supports under investigation are assumed to be undamaged. Control strategy II is applied if the predetermined load ratio has become unsuitable for the load-bearing structure to work properly. Semi-active load redistribution to achieve a desired support load ratio may be used to prevent the structure from possible future failure by relieving a support precautionary. Also, if parts of a structure are known to be weak or damaged, it is reasonable to redistribute the load before it reaches the weak or damaged parts of the load-bearing structure. The time-dependent control deviation of control strategy II

$$e_{\mathrm{II}} = \kappa - \frac{|F_{\mathrm{L}}|}{|F_{\mathrm{R}}|} \stackrel{!}{=} 0 \tag{6.2}$$

represents the difference between the defined load ratio κ (set point) and the actual support reaction force ratio $|F_{\mathrm{L}}|/|F_{\mathrm{R}}|$, which should be zero. The defined load ratio κ describes how the load is supposed to be distributed between the supports. For example, the load at the left support L should be κ times the load at the right support R satisfying $F_{\mathrm{L}} = \kappa F_{\mathrm{R}}$. The desired support reaction force ratio $\kappa = 1$ requires equally loaded supports. The support reaction forces F_{L} and F_{R} for the nu-

merical investigations are obtained from the mathematical model of the semi-active load-bearing structure in equation (3.37) and for the experimental investigations are measured by load cell force sensors, figure 4.1.

6.2 Controller concepts

A reasonable and feasible controller concept is needed to redistribute the right amount of load according to the control deviations (6.1) and (6.2). The selection of a controller concept is based upon the control requirements, e.g. accuracy, and system properties, e.g. semi-active or active, as well as complexity restrictions, e.g. computational capability. Stability issues that are usually related to controlled systems do not need to be addressed in case of semi-active control systems. It is not possible to increase the total energy of the semi-active system and, hence, it is inherently stable, [25]. Thus, the semi-active behavior and the nonlinear friction, section 3.2.2, are the dominating system properties for controller selection, since the system is assumed to be parameter- and time-invariant. In the following, from a huge variety of controller concepts in literature, a selection of possible controller concepts is presented and their applicability to the semi-active load redistribution is discussed.

Gain-scheduled control is based on several independently tuned feedback controllers, e.g. proportional-integral-derivative (PID), model-based controllers or linear-quadratic regulator (LQR), for discrete and mostly linearized design points of the system. The controllers are tuned independently, and interpolate between the design points, [1, 102]. For the case study in this thesis, see section 7.1, there is no need for several design points because the operating points for each investigated case are known and fixed. For a more general application of load redistribution, the gain-scheduled control might be useful, but for a feasible control design in this thesis it is dismissed.

Feedback linearization control can be used to control nonlinear systems. This control concept aims to achieve a linear input-output mapping not by linearization of a discrete point but transformation of the nonlinear system into an equivalent linear system. Nonlinearities of the system are mathematically compensated and not linearized, [1]. Even though the feedback linearization concept in general seems to be feasible, the complexity of this concept is not reasonable to investigate load redistribution. In the particular case of this thesis, the concept faces issues regarding decoupling of outputs, equality of system input and output quantities and the semi-active system behavior. Therefore, the feedback linearization control is dismissed as well.

Clipped-optimal control considers semi-active system behavior and can be used to design linear controllers that provide proper control signals for semi-active approaches. For controller synthesis, the system is assumed to be active by neglecting the limitations of a semi-active system, such as the inability of an actuator to provide certain forces, actuator saturations and dissipativity constraints, [1, 27, 38, 112]. If the calculated control signal from the controller for the active system cannot be directly applied because otherwise violating limitations related to the semi-active system, the control signal is *clipped* and, thus, adapted to the ability of the semi-active system, [26, 38]. The clipped-optimal control approach can be combined with different linear controllers such as PID or LQR. In case of controlled friction forces in the scope of this thesis, the maximum applicable forces to influence the system behavior are dependent on actual local system conditions such as relative velocities $\Delta\dot{z}_{\mathrm{ge}}$, compare equation (3.12), between the connection points and the mass m_{A} and, therefore, are subjected to semi-active system limitations. That is, the control forces or friction forces can be applied only in the direction against the relative velocity Δz_{ge}, which can be considered in the clipped optimal control law. Therefore, the clipped-optimal control approach with an LQR controller for control strategy I, see section 6.2.1, and a PID controller for control strategy II, see section 6.2.2, is selected for semi-active load redistribution in this thesis.

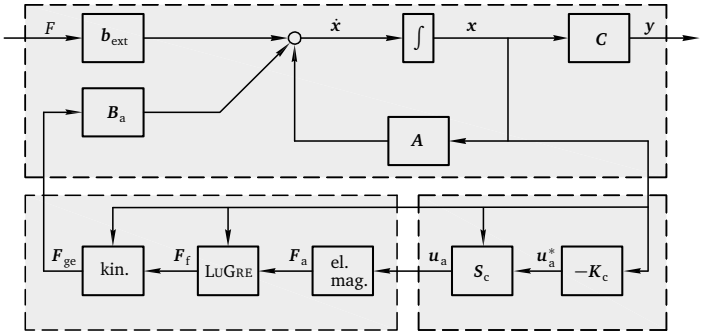

Figure 6.3: Block diagram for the closed loop model with clipped-optimal control principle and state feedback

The basic layout of the clipped-optimal control is depicted in figure 6.3. It comprises the control matrix $-\boldsymbol{K}_{\mathrm{c}}$ and its potential control input $\boldsymbol{u}_{\mathrm{a}}^{*}(t) \hat{=} \boldsymbol{u}_{\mathrm{a}}^{*} = [u_{\mathrm{a,L}}^{*}, u_{\mathrm{a,R}}^{*}]^{\mathrm{T}}$ that has to pass the control law $\boldsymbol{S}_{\mathrm{c}}$ (6.3) deciding if the potential control input $\boldsymbol{u}_{\mathrm{a}}^{*}$

can be applied to the electromagnetic friction brakes or if it needs to be clipped, [26, 38].

The control matrix $-\boldsymbol{K}_\mathrm{c}$ depends on the selected controller, i.e. LQR or PID, see section 6.2.1 and 6.2.2. The control law is defined as

$$\boldsymbol{S}_\mathrm{c} = \begin{cases} 1 & \text{for} \quad \operatorname{sgn}(\mu_{\mathrm{L/R}}(q, \dot{q}, \dot{z}_\alpha)) = \operatorname{sgn}(\boldsymbol{u}_\mathrm{a}^*) \\ 0 & \text{for} \quad \operatorname{sgn}(\mu_{\mathrm{L/R}}(q, \dot{q}, \dot{z}_\alpha)) \neq \operatorname{sgn}(\boldsymbol{u}_\mathrm{a}^*) \end{cases} \tag{6.3}$$

and compares the resulting friction force sign given by $\mu_{\mathrm{L/R}}(q, \dot{q}, \dot{z}_\alpha)$ (3.19) with the desired semi-active force according to the potential control input voltages $\boldsymbol{u}_\mathrm{a}^*$. The case analysis in the control law $\boldsymbol{S}_\mathrm{c}$ (6.3) is required to consider the semi-active limitations of the load redistribution via friction brakes in the guidance elements. That is, the sign of the friction forces $F_{\mathrm{f,L/R}}$ (3.16) resulting from the controlled brake forces $F_{\mathrm{a,L/R}}$ (3.32) and used for load redistribution depends on the relative translational displacement of the mass m_A and the two contact points at $x = a$ and $x = l - a$ of the guidance elements to the beam, figure 3.4(a). If the sign differs from the desired sign of the controller, the potential control input u_a^* needs to be clipped because the actual friction force would have an undesired sign. The input voltages

$$\boldsymbol{u}_\mathrm{a} = \boldsymbol{S}_\mathrm{c} \cdot \boldsymbol{u}_\mathrm{a}^* \tag{6.4}$$

after passing the control law $\boldsymbol{S}_\mathrm{c}$ (6.3) finally supplies the electromagnetic actuators after being amplified to become $\boldsymbol{u}_\mathrm{in} = [u_\mathrm{in,L}, u_\mathrm{in,R}]^\mathrm{T}$, see figure 4.7. For $\boldsymbol{S}_\mathrm{c} = 0$, the control input voltages $\boldsymbol{u}_\mathrm{a}$ are clipped because of the inability of the electromagnetic actuators to provide the desired friction forces from the controller. For $\boldsymbol{S}_\mathrm{c} = 1$, the control input voltages $\boldsymbol{u}_\mathrm{a}$ are applied to the electromagnetic actuators since no semi-active limitations are violated.

6.2.1 Clipped-optimal LQR for control strategy I

As presented in section 6.2, the clipped-optimal control can be combined with a state feedback LQR controller. In general, the LQR controller calculates the control input in a manner to optimally take the systems to the zero state with $\boldsymbol{x} = 0$, [105]. Therefore, the clipped-optimal LQR is used for control strategy I in this thesis according to section 6.1.1. For the clipped-optimal LQR controller synthesis, the system is assumed to be active and linear. Thus, the dynamic behavior of the electromagnetic actuator and the nonlinear friction are neglected, as described in

section 6.2. The potential control input that still has to pass the control law $\boldsymbol{S}_\mathrm{c}$ (6.3) is

$$\boldsymbol{u}_\mathrm{a}^* = -\boldsymbol{K}_\mathrm{LQR}\,\boldsymbol{x}, \tag{6.5}$$

with the control matrix $\boldsymbol{K}_\mathrm{LQR}$ to be determined and the $[6 \times 1]$ state vector $\boldsymbol{x}$ according to equation (3.33). The calculation of the control matrix $\boldsymbol{K}_\mathrm{LQR}$ is based on minimizing the cost function, [73, 105],

$$J = \int_0^\infty \left(\boldsymbol{x}^\mathrm{T}\boldsymbol{Q}\,\boldsymbol{x} + \boldsymbol{u}_\mathrm{a}^\mathrm{T}\boldsymbol{R}\,\boldsymbol{u}_\mathrm{a}\right)\mathrm{d}t \tag{6.6}$$

with the $[6 \times 6]$ state weighting matrix $\boldsymbol{Q}$ for the state vector $\boldsymbol{x}$ and the $[2 \times 2]$ control weighting matrix $\boldsymbol{R}$ for the control input $\boldsymbol{u}_\mathrm{a}$. Since the misalignment φ is to be reduced by control strategy I, the state weighting matrix $\boldsymbol{Q}$ is chosen to be a diagonal matrix with the largest weights accounting for the state vector entries φ and its derivative and results in

$$\boldsymbol{Q} = \begin{bmatrix} 1 & 0 & 0 & 0 & 0 & 0 \\ 0 & 1 & 0 & 0 & 0 & 0 \\ 0 & 0 & 5 \cdot 10^5 & 0 & 0 & 0 \\ 0 & 0 & 0 & 1 & 0 & 0 \\ 0 & 0 & 0 & 0 & 1 & 0 \\ 0 & 0 & 0 & 0 & 0 & 3 \cdot 10^3 \end{bmatrix}. \tag{6.7}$$

For the calculation of the control matrix $\boldsymbol{K}_\mathrm{LQR}$, the ratios of the weights in $\boldsymbol{Q}$ and $\boldsymbol{R}$ are more important than their absolute values, [31, 102]. The control weighting matrix $\boldsymbol{R}$ is chosen as identity matrix

$$\boldsymbol{R} = \begin{bmatrix} 1 & 0 \\ 0 & 1 \end{bmatrix}. \tag{6.8}$$

The $[1 \times 6]$ control matrix

$$\boldsymbol{K}_\mathrm{LQR} = \boldsymbol{R}^{-1}\boldsymbol{B}_\mathrm{a}^\mathrm{T}\boldsymbol{P} \tag{6.9}$$

results from solving the optimization problem by minimizing the cost function J (6.6) with the weighting matrix $\boldsymbol{R}$ (6.8) and the transposed input matrix $\boldsymbol{B}_\mathrm{a}^\mathrm{T}$ (3.35). The $[6 \times 6]$ matrix $\boldsymbol{P}$ is the solution of the continuous-time algebraic RICCATI equation

$$\boldsymbol{A}^\mathrm{T}\boldsymbol{P} + \boldsymbol{P}\boldsymbol{A} - \boldsymbol{P}\boldsymbol{B}_\mathrm{a}\boldsymbol{R}^{-1}\boldsymbol{B}_\mathrm{a}^\mathrm{T}\boldsymbol{P} + \boldsymbol{Q} = 0 \tag{6.10}$$

with the system matrix $\boldsymbol{A}$ in equation (3.33), [2, 105]. The procedure to calculate the control matrix $\boldsymbol{K}_{\mathrm{LQR}}$ (6.9) with the solution of the algebraic RICCATI equation (6.10) is a well known procedure and is also implemented in the MATLAB-function `lqr`. The numerical investigation of load redistribution using the introduced clipped-optimal LQR controller and control strategy I is presented in section 7.2.1.

Implementation to the experimental test setup

The LQR controller is a state feedback controller that calculates the potential control input $\boldsymbol{u}_{\mathrm{a}}^{*}$ (6.5) by means of the control matrix $\boldsymbol{K}_{\mathrm{LQR}}$ (6.9) and the state vector $\boldsymbol{x}$. In physical applications of technical systems it is commonly not possible to measure the complete state vector $\boldsymbol{x}$ of the system, as it is the case for the experimental test setup in this thesis, section 4. Alternatively, the state vector $\boldsymbol{x}$ can be calculated using an observer, e.g. a LUENBERGER observer [103], or reconstructed using the measured output vector $\boldsymbol{y}_{\mathrm{meas}}(t) \hat{=} \boldsymbol{y}_{\mathrm{meas}}$, [31]. For this thesis, the state vector $\boldsymbol{x}$ is reconstructed and the displacement x_{B} of the beam and the misalignment φ are obtained by means of the inverse of the reduced output matrix $\boldsymbol{C}_{\mathrm{red}}^{-1}$ and the displacement outputs $\boldsymbol{y}_{\mathrm{dis}}(t) \hat{=} \boldsymbol{y}_{\mathrm{dis}} = [z_{\mathrm{L}}, z_{\mathrm{R}}]^{T}$ that are measured by laser distance sensors, figure 4.1, to

$$\begin{bmatrix} z_{\mathrm{B}} \\ \varphi \end{bmatrix} = \boldsymbol{C}_{\mathrm{red}}^{-1} \boldsymbol{y}_{\mathrm{dis}} \quad \text{with} \quad \boldsymbol{C}_{\mathrm{red}}^{-1} = \begin{bmatrix} -\frac{1}{2} & \frac{1}{2} \\ \frac{1}{l_{\mathrm{B}}} & \frac{1}{l_{\mathrm{B}}} \end{bmatrix}. \tag{6.11}$$

The entries of the reduced output matrix $\boldsymbol{C}_{\mathrm{red}}$ are part of the output matrix $\boldsymbol{C}$ (3.36) with $\boldsymbol{C}_{\mathrm{red},11} = \boldsymbol{C}_{25}$, $\boldsymbol{C}_{\mathrm{red},12} = \boldsymbol{C}_{26}$, $\boldsymbol{C}_{\mathrm{red},21} = \boldsymbol{C}_{35}$ and $\boldsymbol{C}_{\mathrm{red},22} = \boldsymbol{C}_{36}$. The numerical indices indicate the matrix position of each entry.

The time derivatives of z_{B} and φ are approximated with a first-order BUTTERWORTH highpass filter, [102]. The displacement z_{A} of the mass m_{A} and velocity $\dot{z}_{\mathrm{A}}$ are approximated by integrating the measured acceleration $\ddot{z}_{\mathrm{A}}$ once and twice, respectively, and filtering with a first-order BUTTERWORTH highpass filters. The highpass filters reduce the drift caused by the integration of signals with offset. The assembled state vector $\boldsymbol{x} = [z_{\mathrm{A}}, z_{\mathrm{B}}, \varphi, \dot{z}_{\mathrm{A}}, \dot{z}_{\mathrm{B}}, \dot{\varphi}]^{\mathrm{T}}$ is fed into the controller (6.5) and (6.12).

Figure 6.4 depicts the block diagram for the clipped-optimal control application with LQR state feedback controller. The mathematical model, see section 3.2.3, is shaded in gray since it is substituted by the physical system with the measured

output vector $\boldsymbol{y}_{\text{meas}} = [z_{\text{R}}, z_{\text{L}}, \ddot{z}_{\text{A}}]^{\text{T}}$, compare figure 6.3. The measured output from vector $\boldsymbol{y}_{\text{meas}}$ consists of the displacements $\boldsymbol{y}_{\text{dis}} = [z_{\text{R}}, z_{\text{L}}]^{\text{T}}$ and the acceleration $\ddot{z}_{\text{A}}$ of the mass m_{A}.

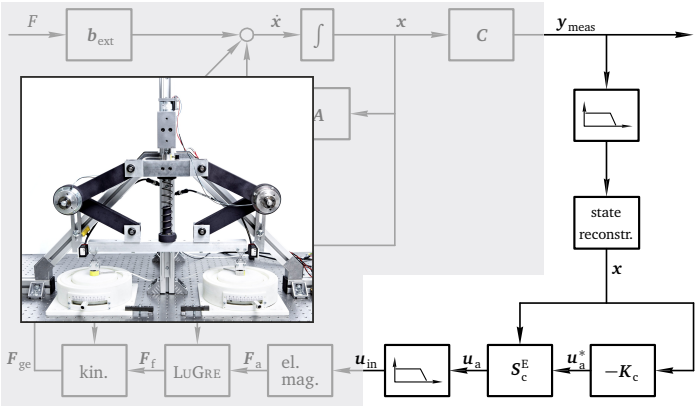

Figure 6.4: Block diagram for the clipped-optimal control application with LQR state feedback controller and the model ( ) substituted by the physical system

Equation (6.11) and integrating $\ddot{z}_{\text{A}}$ once and twice eventually lead to the reconstructed complete state space vector $\boldsymbol{x}$. The state reconstruction for the state vector $\boldsymbol{x}$ is detailed in figure 6.5.

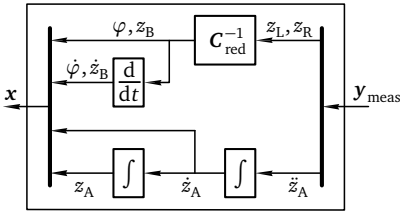

Figure 6.5: State reconstruction block to provide the complete state vector $\boldsymbol{x}$ for the LQR state feedback controller

For the experimental implementation, the control law is defined as

$$\boldsymbol{S}_{\mathrm{c}}^{\mathrm{E}} = \begin{cases} 1 & \text{for} \quad \operatorname{sgn}(\Delta \dot{z}_{\mathrm{L/R}}) = \operatorname{sgn}(\boldsymbol{u}_{\mathrm{a}}^{*}) \\ 0 & \text{for} \quad \operatorname{sgn}(\Delta \dot{z}_{\mathrm{L/R}}) \neq \operatorname{sgn}(\boldsymbol{u}_{\mathrm{a}}^{*}). \end{cases} \tag{6.12}$$

and compares the sign of the relative translational displacement of the two supports and the mass m_{A} defined by $\Delta \dot{z}_{\mathrm{L/R}} = \dot{z}_{\mathrm{L/R}} - \dot{z}_{\mathrm{A}}$, compare figure 3.4(a), with the sign of the desired semi-active forces corresponding to the potential input voltages $\boldsymbol{u}_{\mathrm{a}}^{*}$ (6.5). The control law $\boldsymbol{S}_{\mathrm{c}}^{\mathrm{E}}$ (6.12) differs from $\boldsymbol{S}_{\mathrm{c}}$ (6.3) for the sake of measurability of the compared quantities. The resulting input voltages $\boldsymbol{u}_{\mathrm{a}}$ (6.4) are lowpass filtered and smoothed by analogue 6th-order elliptic reconstruction filters before being amplified and applied to the electromagnetic brakes in the guidance elements, see section 4.4. The experimental investigation of load redistribution using the introduced clipped-optimal LQR controller and control strategy I is presented in section 7.3.1.

6.2.2 Clipped-optimal PID for control strategy II

The clipped-optimal control can be combined with a signal-based PID controller. The PID controller uses the measured sensor signals to calculate the potential control input $\boldsymbol{u}_{\mathrm{a}}^{*}$. It does not need the state vector $\boldsymbol{x}$. Also, it is simple to apply a non-zero set point, which is possible for the LQR controller only with an additional pre-filter. Therefore, the clipped-optimal PID controller is used for control strategy II in this thesis according to section 6.1.2. The potential control inputs of the PID controller is calculated by

$$u_{\mathrm{a,L}}^{*} = \quad K_{\mathrm{P}}\, e_{\mathrm{II}} + K_{\mathrm{I}} \int e_{\mathrm{II}}\, \mathrm{d}t + K_{\mathrm{D}}\, \frac{\mathrm{d}\, e_{\mathrm{II}}}{\mathrm{d}t} \tag{6.13a}$$

$$u_{\mathrm{a,R}}^{*} = -K_{\mathrm{P}}\, e_{\mathrm{II}} - K_{\mathrm{I}} \int e_{\mathrm{II}}\, \mathrm{d}t - K_{\mathrm{D}}\, \frac{\mathrm{d}\, e_{\mathrm{II}}}{\mathrm{d}t} \tag{6.13b}$$

with the control deviation e_{II} (6.2). In equation (6.13), K_{P} is the gain of the proportional control element, K_{I} is the gain of the integral control element and K_{D} is the gain of the derivative control element. K_{P}, K_{I} and K_{D} are the tunable elements of the PID controller. They are predetermined by the ZIEGLER-NICHOLS tuning method and from that base fine-tuned empirically, [115, 120]. The numerical investigation of load redistribution using the introduced clipped-optimal PID controller and control strategy II is presented in section 7.2.2.

Implementation to the experimental test setup

The PID controller is a signal-based feedback controller that calculates the potential control inputs $\boldsymbol{u}_{\mathrm{a}}^{*}$ (6.13) based on the control deviation e_{II} (6.2). In order to calculate the control deviation e_{II} (6.2), the two support reaction forces F_{L} and F_{R} are needed. These are obtained directly from the measured outputs $\boldsymbol{y}_{\mathrm{meas}} = [F_{\mathrm{L}}, F_{\mathrm{R}}]^{\mathrm{T}}$.

Figure 6.6 depicts the block diagram for the clipped-optimal control application with PID feedback controller. The mathematical model, see section 3.2.3, is shaded in gray since it is substituted by the physical system with the measured output vector $\boldsymbol{y}_{\mathrm{meas}}$, compare figure 6.3. The state reconstruction as in section 6.2.1 and figure 6.4 is not needed since the output vector $\boldsymbol{y}_{\mathrm{meas}}$ directly contains the support reaction forces F_{L} and F_{R} to calculate the control deviation e_{II} (6.2) with the defined load ratio κ as set point for the controller, see section 6.1.2.

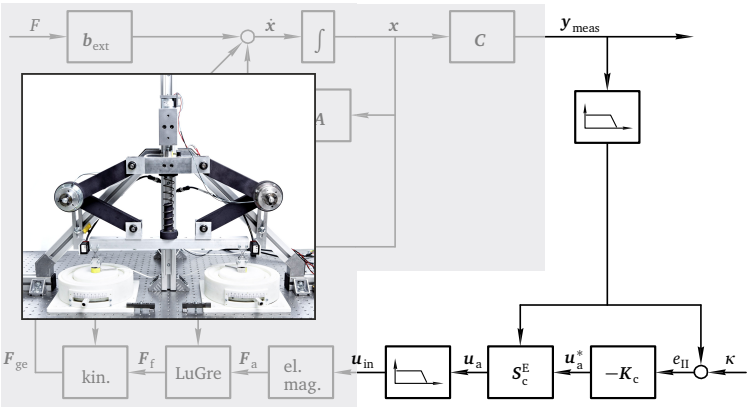

Figure 6.6: Block diagram for the clipped-optimal control application with PID feedback controller and the model ( ) substituted by the physical system

The control law $\boldsymbol{S}_{\mathrm{c}}^{\mathrm{E}}$ (6.12) is applied to the potential control input voltages $\boldsymbol{u}_{\mathrm{a}}^{*}$ (6.13) to obtain the control input voltages $\boldsymbol{u}_{\mathrm{a}}$ (6.4) similar to section 6.2.1. The control input voltages $\boldsymbol{u}_{\mathrm{a}}(t)$ (6.4) are lowpass filtered and smoothed by analogue 6th-order elliptic reconstruction filters before being amplified and applied to the electromagnetic brakes in the guidance elements, see section 4.4. The experimental investigation of load redistribution using the introduced clipped-optimal PID controller and control strategy II is presented in section 7.3.2.

7 Numerical and experimental investigation of load redistribution

This chapter presents the numerical and experimental results of semi-active load redistribution in the load-bearing structure as part of SHC, section 1.1. The mathematical model for numerical investigation was introduced in section 3.2 and the experimental test setup in chapter 4. First, a case study comprising different cases regarding control strategy and support health condition is introduced in section 7.1. Subsequently, the cases are used to numerically investigate the load redistribution capability of the semi-active guidance elements in the load-bearing structure in section 7.2. In section 7.3, the numerical results are proved by experimental investigation of the case study. Finally, the results of the numerical and experimental load redistribution are summarized and discussed in section 7.4.

7.1 Deliberate insertion of uncertainty: a case study

The deliberate insertion of uncertainty is defined by the systematic variation of the support stiffness to simulate damage or wear of the supports. The stiffness variation is achieved via the adjustable supports (1L) and (1R), section 4.3. Varying support stiffness causes uncertain dynamic behavior, i.e. beam misalignment $z_L - z_R$ and undesired support reaction forces ratio, compare section 6.1. The uncertainty is supposed to be reduced by means of semi-active load redistribution. In order to investigate the of semi-active load redistribution capability, 4 cases comprising the different control strategies I and II and different severities of damage are introduced:

Case 1: The system is undamaged and both supports (1L) and (1R) have equal stiffness $k_L = k_R = 40\,000\,\mathrm{N/m}$. The control is disabled and the system is assumed to be passive without the function of the semi-active guidance elements. The case 1 serves as reference case for both control strategies I, section 6.1.1, and II, section 6.1.2 and is used to compare and evaluate the cases 2, 3 and 4.

Case 2: The system is assumed to be moderately damaged with 50% reduced stiffness $k_R = 20\,000\,\mathrm{N/m}$ of the right support (1R) compared to case 1. The left

support (1L) is unchanged with $k_L = 40\,000\,\mathrm{N/m}$. Case 2 is divided into two subcases 2a and 2b. In subcase 2a, the control is disabled and the system is assumed to be passive without the function of the semi-active guidance elements. In subcase 2b, the control is enabled and the system is assumed to be with the function of the semi-active guidance elements to redistribute the load. Control strategy I is applied.

Case 3: The system is assumed to be severely damaged with 75% reduced stiffness $k_R = 10\,000\,\mathrm{N/m}$ of the right support (1R) compared to case 1 and again 50% compared to case 2. The left support (1L) is unchanged with $k_L = 40\,000\,\mathrm{N/m}$. Case 3 is divided into two subcases 3a and 3b. In subcase 3a, the control is disabled and the system is assumed to be passive without the function of the semi-active guidance elements. In subcase 3b, the control is enabled and the system is assumed to be with the function of the semi-active guidance elements to redistribute the load. Control strategy I is applied.

Case 4: The system is undamaged and both supports (1L) and (1R) have equal stiffness $k_L = k_R = 40\,000\,\mathrm{N/m}$. The control is enabled and the system is assumed to be with the function of the semi-active guidance elements to redistribute the load. Control strategy II is applied.

Table 7.1 summarize the introduced cases and presents the support stiffnesses, severity of support damage and control status as well as the applied control strategy. The cases are investigated numerically and experimentally in the following sections.

Table 7.1: Cases to investigate load redistribution with semi-active guidance elements

case	(1L)	(1R)	damage	control	strategy
1	40 000 N/m	40 000 N/m	none	off	I/II
2a	40 000 N/m	20 000 N/m	moderate	off	I
2b	40 000 N/m	20 000 N/m	moderate	on	I
3a	40 000 N/m	10 000 N/m	severe	off	I
3b	40 000 N/m	10 000 N/m	severe	on	I
4	40 000 N/m	40 000 N/m	none	on	II

7.2 Numerical investigation of load redistribution

This section presents the numerical investigation of the case study summarized in table 7.1. For that, a time series of 2 seconds is simulated and analyzed regarding the load path and dynamic behavior, i.e. overshoots, oscillations and steady state, with and without semi-active control. The load-bearing structure is excited by a step load according to equation (3.7) applied to the mass m_A. The mathematical model introduced in section 3.2 is used for simulations with the calibrated parameter ranges according to section 5.2 with table 5.3 and section 5.3 with table 5.8. The calibrated parameter ranges are used to conduct MC simulations to consider the remaining model prediction uncertainty. The most likely model predictions are obtained with the modes of the calibrated parameters, compare figure 2.5. Instead of ignoring the uncertainty by stating only one deterministic curve, the uncertainty in the model prediction caused by the remaining parameter uncertainty is indicated by shaded areas. The two different semi-active control strategies I and II introduced in section 6.1 organize the following subsections.

7.2.1 Misalignment reduction: cases 1, 2 and 3

For the cases 1, 2 and 3 from table 7.1, the control strategy I from section 6.1.1 is applied with the semi-active guidance elements to counteract the decreasing support stiffness by redistributing the loads towards the undamaged support and thereby reducing the misalignment $x_R - x_L$ of the beam m_B, figure 3.4(a). In order to evaluate the load redistribution capability of the semi-active guidance elements, first the misalignment $x_R - x_L$ and second the load path represented by the support reaction forces F_L and F_R are analyzed.

Misalignment analysis

Figure 7.1 depicts the beam's misalignment $x_R - x_L$ due to the external force excitation according to equation (3.7) for case 2, figure 7.1(a), and for case 3, figure 7.1(b). Case 1 serves in both subplots as reference with misalignment $x_R - x_L = 0$ for the entire simulation time $t = 0\,\mathrm{s}$ to $t = 2\,\mathrm{s}$. The simulation results for case 2 with the modes of the calibrated parameter are indicated with dashed lines, case 2a in blue and case 2b in red, and solid lines for case 3, case 3a in blue and case 3b in red. The shaded area around the lines envelopes the results of 300 MC simulations with varying model parameters representing the remaining

parameter uncertainty according to the calibration result in chapter 5 to consider the model prediction uncertainty.

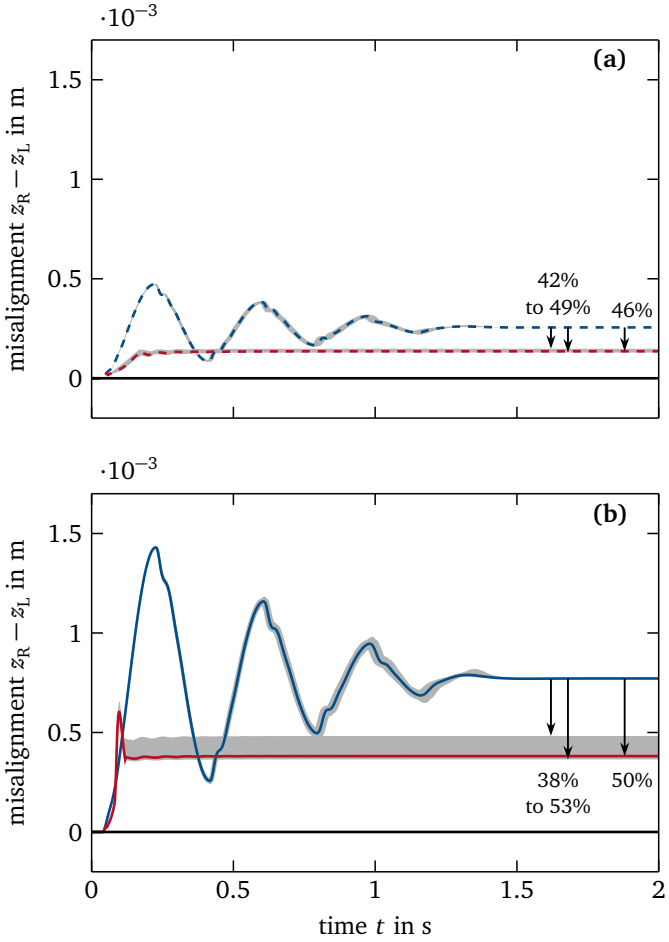

Figure 7.1: Simulated beam misalignment $z_R - z_L$ with the corresponding uncertainty ranges ( ) due to model parameter uncertainty according to chapter 5 and misalignment reduction, compare table 7.2, for **(a)** cases 1 (——), 2a (– –), and 2b (– –), and **(b)** cases 1 (——), 3a (——) and 3b (——)

In figure 7.1(a), after an overshoot at around 0.22 s and misalignment oscillations from time $0.04 \leq t \leq 1.4$ s, the steady state misalignment ensues at around $0.255 \cdot 10^{-3}$ m for case 2a. Approximately no overshoot and no oscillations are observed for case 2b with control on. Hence, the misalignment peaks are reduced significantly comparing case 2a without control and case 2b with control. The steady state misalignment for case 2b from around $t = 0.4$ s ensues between 0.129 to $0.148 \cdot 10^{-3}$ m. The steady state misalignment reduction is found to be 46 % for the mode simulations. The minimum steady state misalignment reduction is found to be 42 %. Minimum reduction describes the comparison between the shaded area's lower bound for case 2a and the shaded area's upper bound for case 2b. The maximum steady state misalignment reduction is found to be 49 %. Maximum reduction describes the comparison between the shaded area's upper bound for case 2a and the shaded area's lower bound for case 2b.

In figure 7.1(b), after an overshoot at around 0.22 s and misalignment oscillations from time $0.04 \leq t \leq 1.45$ s, the steady state misalignment ensues at around $0.772 \cdot 10^{-3}$ m for case 3a. A small overshoot at $t = 0.09$ s and approximately no oscillations are observed for case 3b. Hence, the misalignment peaks are reduced significantly comparing case 3a without control and case 3b with control. The steady state misalignment from around $t = 0.35$ s ensues between 0.365 to $0.482 \cdot 10^{-3}$ m. The steady state misalignment reduction is found to be 50 % for the mode simulations. The minimum steady state misalignment reduction is found to be 38 %. Minimum reduction describes the comparison between the shaded area's lower bound for case 3a and the shaded area's upper bound for case 3b. The maximum steady state misalignment reduction is found to be 53 %. Maximum reduction describes the comparison between the shaded area's upper bound for case 3a and the shaded area's lower bound for case 3b. Since the controller from section 6.2.1 is tuned to the mode parameter values, deviations from these values result in reduced load redistribution capability and explains why the mode simulation, solid red line, is close to the shaded area's lower bound.

The semi-active load redistribution in cases 2b and 3b results in a misalignment reduction as compared to the corresponding passive cases 2a and 3a, but there remains a steady state misalignment of the beam. The semi-active guidance elements cannot increase the restoring forces in steady state to further reduce the misalignment because of limitations associated to the semi-activity of the guidance elements, see section 6.2. Beside the steady state reduction, the overshoots are reduced in case 2 as well as case 3. The misalignment oscillations are almost entirely damped for the semi-active systems. Table 7.2 summarizes the simulation results for cases 1, 2 and 3.

Table 7.2: Simulated steady state (sts.) misalignment reduction considering model parameter uncertainty for cases 1, 2 and 3

	sts. misalignment $x_R - x_L$ in m			sts. reduction in %		
case	mode	min.	max.	mode	min.	max.
1	$0.000 \cdot 10^{-3}$	$0.000 \cdot 10^{-3}$	$0.000 \cdot 10^{-3}$	–	–	–
2a	$0.255 \cdot 10^{-3}$	$0.255 \cdot 10^{-3}$	$0.256 \cdot 10^{-3}$	–	–	–
2b	$0.136 \cdot 10^{-3}$	$0.129 \cdot 10^{-3}$	$0.148 \cdot 10^{-3}$	46	42	49
3a	$0.771 \cdot 10^{-3}$	$0.771 \cdot 10^{-3}$	$0.772 \cdot 10^{-3}$	–	–	–
3b	$0.381 \cdot 10^{-3}$	$0.365 \cdot 10^{-3}$	$0.482 \cdot 10^{-3}$	50	38	53

Load path analysis

Additional to the misalignment in figure 7.1, the corresponding load paths are investigated. The load path of the load-bearing structures is represented by the support reaction forces F_L and F_R according to (3.5) and indicate how the excitation load F is distributed within the structure.

Figure 7.2 depicts the load path of the load-bearing structure due to the external force excitation according to equation (3.7) for case 2 and case 3. Case 1 is in both subplots covered by the passive system responses for case 2a and 3a for the entire simulation time $t = 0\,\mathrm{s}$ to $t = 2\,\mathrm{s}$. The simulation results for case 2 with the modes of the calibrated parameter are indicated with dashed lines and solid lines for case 3. The shaded area around the lines indicates the results of 300 MC simulations with varying model parameters representing the remaining parameter uncertainty according to the calibration result in chapter 5 to consider the model prediction uncertainty.

In figure 7.2(a), after an overshoot at around 0.22 s and force oscillations from time $0.04 \leq t \leq 1.4\,\mathrm{s}$, the excitation load is equally distributed to $F_L = F_R = 12\,\mathrm{N}$ in the steady state at $t > 1.4\,\mathrm{s}$ for case 2a. Even though, the misalignment for case 2a is $x_R - x_L \neq 0$, see figure 7.1. In case 2b, the support reaction forces are $F_L \geq F_R$ for almost the entire simulation time $t = 0\,\mathrm{s}$ to $t = 2\,\mathrm{s}$ accept a small range around $t = 0.2\,\mathrm{s}$. The excitation load is no longer equally distributed to the supports L and R, but depending on the support stiffness. The load redistribution results from the semi-active guidance elements with control strategy I and, consequently, results in a misalignment reduction. The steady state relief of the damaged support R is found to be 14 % for the mode simulations and minimum 13 %. Minimum relief

describes the comparison between the shaded area's lower bound for case 2a and the shaded area's upper bound for F_R in case 2b.

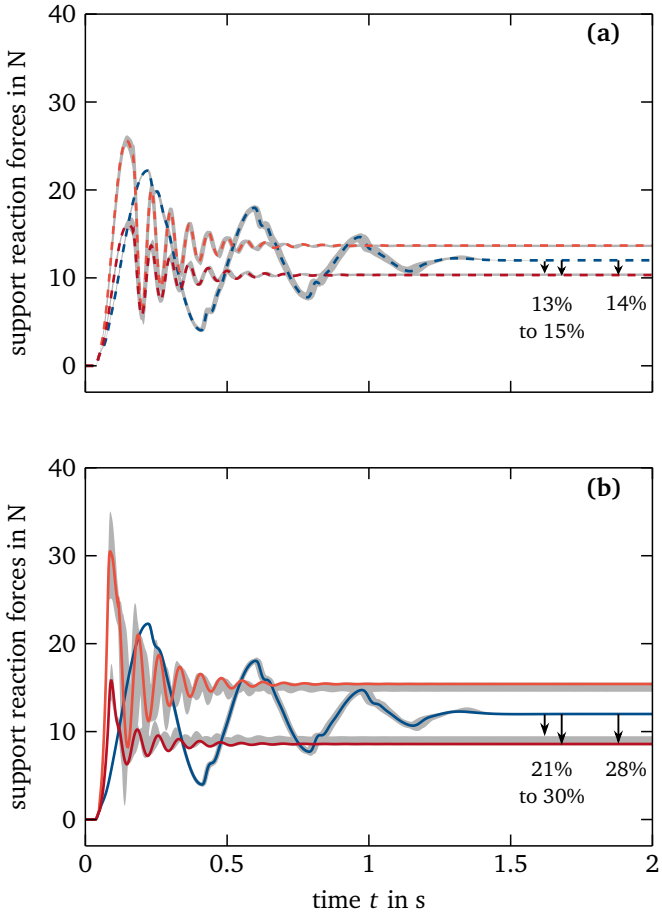

Figure 7.2: Simulated support reaction forces with the corresponding uncertainty ranges ( ) due to model parameter uncertainty according to chapter 5 and relief of support R, compare table 7.3, for **(a)** case 2a with F_R (– –) and covered F_L (– –), and case 2b with F_R (– –) and F_L (– –), and **(b)** case 3a with F_R (——) and covered F_L (——), and case 3b with F_R (——) and F_L (——)

In figure 7.2(b), after an overshoot at around 0.22 s and force oscillations from time $0.04 \leq t \leq 1.4$ s, the excitation load is equally distributed to $F_L = F_R = 12$ N in the steady state at $t > 1.4$ s for case 3a. Even though, the misalignment for case 3a is $x_R - x_L \neq 0$, see figure 7.1. In case 3b, the support reaction forces are $F_L \geq F_R$ for wide ranges ot the simulation time $t = 0$ s to $t = 2$ s accept between $t = 0.1$ s to $t = 0.23$ s. The excitation load is no longer equally distributed to the supports L and R, but depending on the support stiffness. The load redistribution results from the semi-active guidance elements with control strategy I and, consequently, results in a misalignment reduction. The steady state relief of the damaged support R is found to be 28 % for the mode simulations and minimum 21 %. Minimum relief describes the comparison between the shaded area's lower bound for case 3a and the shaded area's upper bound for F_R in case 3b. Since the controller from section 6.2.1 is tuned to the mode parameter values, deviations from these values result in reduced load redistribution capability and explains why the mode simulation results for F_L is close to the shaded area's upper bound and F_R is close to the shaded area's lower bound, compare figure 7.1(b). Table 7.3 summarizes the simulation results for cases 1, 2 and 3.

Table 7.3: Simulated steady state (sts.) support reaction forces (load) for mode parameter simulation and support relief and considering model parameter uncertainty for cases 1, 2 and 3

	sts. load in N		support R relief in %		
case	support L	support R	mode	min.	max.
1	12	12	–	–	–
2b	13.68	10.32	14	13	15
3b	15.41	8.59	28	21	30

According to the objective for the semi-active guidance elements with control strategy I, the load is redistributed from support R to support L to reduce the misalignment $x_R - x_L$ caused by the deliberate introduced uncertainty by means of varying support stiffness. In the passive cases 1, 2a and 3a, the load is equally distributed to both supports through the predetermined load path via the spring-damper only, figure 3.2. With the semi-active controlled guidance elements, an additional load path through the guidance elements is provided in cases 2b and 3b that redistributes a portions of the load as may be required by varying support stiffness.

7.2.2 Defined load ratio: cases 1 and 4

For cases 1 and 4 from table 7.1, the control strategy II from section 6.1.2 is applied with the semi-active guidance elements to achieve a desired load ratio κ by redistributing the loads from support R to support L if $\kappa > 1$ and from support L to support R if $\kappa < 1$. Equal loads at the supports L and R require $\kappa = 1$. In case 4, the load ratio set point is chosen to be $\kappa = 2$ for the following investigation, that is, the support L is supposed to bear twice the load compared to support R. In order to evaluate the load redistribution capability of the semi-active guidance elements, first the support reaction force ratio and second the load path represented by the support reaction forces F_{L} and F_{R} are analyzed.

Support reaction force ratio analysis

Figure 7.3 depicts the support reaction force ratio $|F_{\mathrm{L}}|/|F_{\mathrm{R}}|$ due to the external excitation according to equation (3.7) for case 1 and case 4. Case 1 serves as reference with the reaction force ratio $|F_{\mathrm{L}}|/|F_{\mathrm{R}}| = 1$ for the entire simulation time $t = 0\,\mathrm{s}$ to $t = 2\,\mathrm{s}$. The simulation results for case 4 with the modes of the calibrated parameter are indicated with a solid red line. The shaded area around the line indicates the results of 300 MC simulations with varying model parameters representing the remaining parameter uncertainty according to the calibration result in chapter 5 to consider the model prediction uncertainty. The ordinate is scaled logarithmic to capture the fact that the ratio $\kappa = 2$ and $\kappa = 0.5$ represent the same load ratio with just different directions, e.g. right to left and left to right.

In figure 7.3, after oscillations from time $0.13 \leq t \leq 0.9\,\mathrm{s}$, the steady state support reaction force ratio $|F_{\mathrm{L}}|/|F_{\mathrm{R}}|$ ensues between 1.76 to 1.85 for case 4. For the mode simulations, the steady state support reaction force ratio $|F_{\mathrm{L}}|/|F_{\mathrm{R}}|$ ensues at 1.83 for $t > 0.9\,\mathrm{s}$. Since the controller from section 6.2.2 is tuned to the mode parameter values, deviations from these values result in reduced load redistribution capability and explains why the mode simulation, solid red line, is close to the shaded area's upper bound. Table 7.4 summarizes the simulation results for cases 1 and 4.

The semi-active load redistribution in case 4 results in an approximation to the defined load ratio $\kappa = 2$, but there remains a steady state control deviation. The load is redistributed from support R towards support L to reach the defined load ratio $\kappa = 2$ as close as possible subjected to limitations associated to the semi-activity of the guidance elements, section 6.2. The semi-active guidance elements cannot further redistribute loads in steady state.

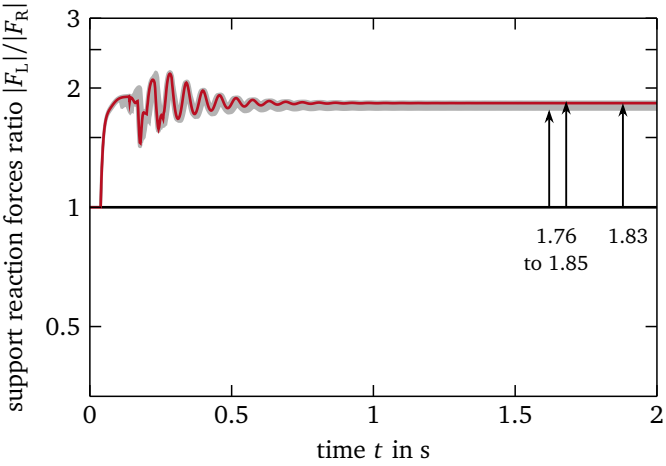

Figure 7.3: Simulated support reaction force ratio, compare table 7.4, with the corresponding uncertainty range ( ) due to model parameter uncertainty according to chapter 5 for cases 1 (——) and 4 (——), logarithmic scaled ordinate

Table 7.4: Simulated steady state (sts.) support reaction force ratio for mode parameter simulation and considering model parameter uncertainty for cases 1 and 4

	sts. support reaction force ratio		
case	mode	min.	max.
1	1	1	1
4	1.83	1.76	1.85

Load path analysis

Figure 7.4 depicts the load path of the load-bearing structure due to the external excitation according to equation (3.7) for cases 1 and 4 corresponding to the supports' reaction force ratio in figure 7.3. The simulation results for case 4 with the modes of the calibrated parameter are indicated with solid lines. The shaded areas around the lines indicate the results of 300 MC simulations with varying model parameters representing the remaining parameter uncertainty according to the calibration result in chapter 5 to consider the model prediction uncertainty.

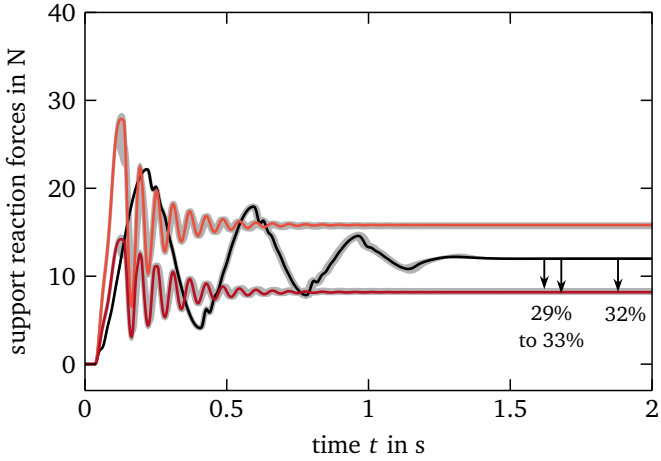

Figure 7.4: Simulated support reaction forces with the corresponding uncertainty ranges ( ) due to model parameter uncertainty according to chapter 5 and relief of support R, compare table 7.5, for case 1 with F_R(——) and identical and covered F_L(——), and case 4 with F_R (——) and F_L(——)

In case 4, the support reaction forces are $F_L \geq F_R$ for wide ranges of the simulation time $t = 0\,\text{s}$ to $t = 2\,\text{s}$ accept between $t = 0.15\,\text{s}$ to $t = 0.24\,\text{s}$. The excitation load is not equally distributed to the supports L and R anymore. The load redistribution results from the semi-active guidance elements with control strategy II and, consequently, results in an approximation to the defined load ration $\kappa = 2$. The steady state relief of the support R is found to be 32 % for the mode simulations and minimum 29 %. Since the controller from section 6.2.2 is tuned to the mode parameter values, deviations from these values result in reduced load redistribution capability and explains why the mode simulation results for F_L is close to the shaded area's upper bound and F_R is close to the shaded area's lower bound, compare figure 7.3. Table 7.5 summarizes the simulation results for cases 1 and 4.

According to the objective for the semi-active guidance elements with control strategy II, the load is redistributed from support R towards support L in order to change the predetermined load path and achieve a defined load ratio κ and, thus, reduce the uncertainty of an inappropriate load path by future damage. In the passive case 1, the load is equally distributed to both supports through the

predetermined load path via the spring-damper only, figure 3.2. With the semi-active controlled guidance elements, an additional load path through the guidance elements is provided in case 4 that redistributes a portion of the load as may be required to change the load ratio. Both control strategies I and II in cases 2b, 3b and 4 result in similar support reaction forces F_L and F_R, see figures 7.2 and 7.4, since in both control strategies the right support R is supposed to be relieved in order to reduce the control deviation (6.1) and (6.2), respectively.

Table 7.5: Simulated steady state (sts.) support reaction forces (load) and support relief for mode parameter simulation and considering model parameter uncertainty for cases 1 and 4

	sts. load in N		support R relief in %		
case	support L	support R	mode	min.	max.
1	12	12	–	–	–
4	15.82	8.18	32	29	33

7.3 Experimental investigation of load redistribution

This section presents the experimental investigation of the case study summarized in table 7.1. A time series of 2 seconds is measured and analyzed regarding the load path and dynamic behavior, i.e. overshoots, oscillations and steady state, with and without semi-active control. All presented experimental results are based on the averaging of 10 measurement repetitions. All sensors are reset to zero before starting each measurement. Thus, the static mass of the experimental test setup is neglected so that only the excitation caused by the load mass ⑩, figure 4.1, is measured and subjected to potential load redistribution. The load mass ⑩ excites the load-bearing structure with a step load. The experimental test setup of the simplified load-bearing structure introduced in section 4 is used to conduct the experimental case study according to table 7.1. The experimental test setup is assumed to be deterministic and no parts of the test rig setup are changed during measurements in order to avoid further uncertainty which is not addressed in this thesis, e.g. manufacturing tolerances and assembly variations. The experimental results are compared to the model predictions obtained from MC simulations in

section 7.2 to evaluate the model prediction accuracy. The two different semi-active control strategies I and II introduced in section 6.1 organize the following subsections.

7.3.1 Misalignment compensation: cases 1, 2 and 3

For the cases 1, 2 and 3 from table 7.1, control strategy I from section 6.1.1 is applied with the semi-active guidance elements to counteract the reduced support stiffness by redistributing the loads towards the undamaged support (1L) in figure 4.1 and thereby reducing the measured misalignment $x_R - x_L$ of the beam (3). For the experimental investigation, the support stiffnesses (1L) and (1R) can be adjusted for the cases 2 and 3, figure 4.6. In order to evaluate the load redistribution capability of the semi-active guidance elements, first the measured misalignment $x_R - x_L$ and second the load path represented by the measured support reaction forces F_L and F_R are analyzed and compared to the numerical MC simulations from section 7.2.1.

Misalignment analysis

Figure 7.5 depicts the measured beam misalignment $x_R - x_L$ due to the excitation via load mass (10) for case 2, figure 7.5(a), and case 3, figure 7.5(b). Case 1 serves in both subplots as reference with misalignment $x_R - x_L \approx 0$ for the entire measurement time $t = 0\,\mathrm{s}$ to $t = 2\,\mathrm{s}$. The experimental results for case 2 are indicated with dashed lines, case 2a in blue and case 2b in red, and solid lines for case 3, case 3a in blue and case 3b in red. The shaded areas in figure 7.5 originate from the numerical MC simulations in figure 7.1.

In figure 7.5(a), after an overshoot at around 0.21 s and misalignment oscillations from time $0.04\,\mathrm{s} \leq t \leq 1.25\,\mathrm{s}$, the steady state misalignment ensues at $0.243 \cdot 10^{-3}\,\mathrm{m}$ for case 2a. One short overshoot and higher frequency oscillations are observed for case 2b. The steady state misalignment from around $t = 0.5\,\mathrm{s}$ ensues at $0.119 \cdot 10^{-3}\,\mathrm{m}$. Due to the short overshoot for case 2b, the measured peak misalignment reduction is insignificant, unlike the mere simulation results in figure 7.1(a). The measured steady state misalignment reduction is found to be 51 %. The shaded area of the model prediction for case 2a shows similar dynamic behavior for the entire time scale and widely encompasses the experimental results. For case 2b, the model prediction does not capture the overshoot and higher frequency oscillations from time $0.04\,\mathrm{s} \leq t \leq 0.5\,\mathrm{s}$. The steady state misalignment reduction is slightly underestimated in the simulations.

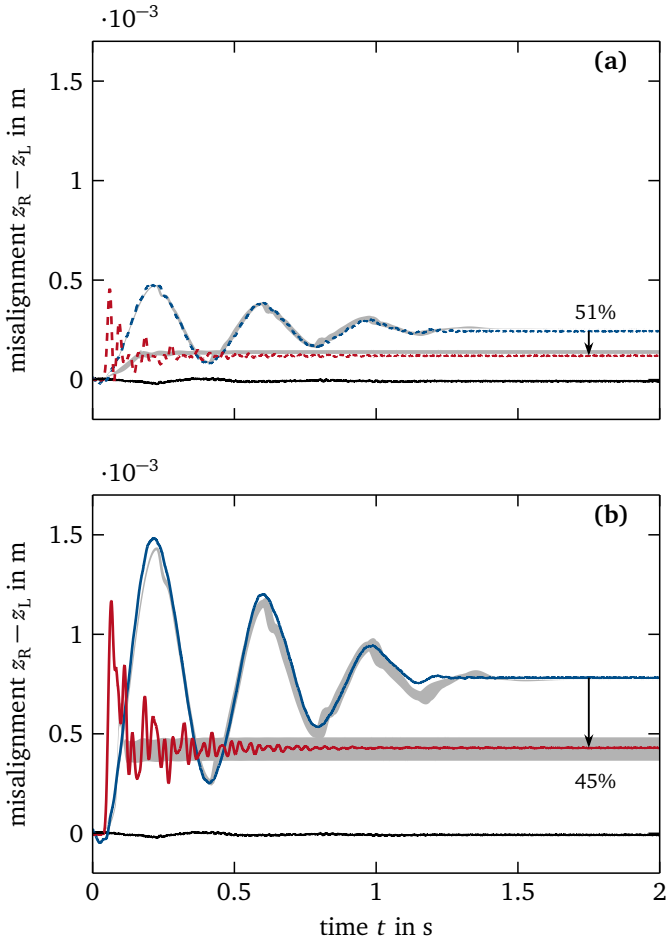

Figure 7.5: Measured beam misalignment $z_R - z_L$ with the simulated uncertainty ranges ( ) due to model parameter uncertainty from figure 7.1 and sts. misalignment reduction, compare table 7.6, for **(a)** cases 1 (——), 2a (– –), and 2b (– –), and **(b)** cases 1 (——), 3a (——) and 3b (——)

In figure 7.5(b), after an overshoot at around 0.21 s and misalignment oscillations from time $0.04\,\mathrm{s} \leq t \leq 1.3\,\mathrm{s}$, the steady state misalignment ensues at around $0.782 \cdot 10^{-3}\,\mathrm{m}$ for case 3a. An overshoot at $t = 0.06\,\mathrm{s}$ and higher frequency os-

cillations are observed for case 3b. The steady state misalignment from around $t = 0.8\,\mathrm{s}$ ensues at $0.429 \cdot 10^{-3}\,\mathrm{m}$. The measured peak misalignment reduction is still significant but less than the mere simulation results in figure 7.1(b). The measured steady state misalignment reduction is found to be 45 %. The shaded area of the model prediction for case 3a shows similar dynamic behavior for the entire time scale and partly encompass the experimental results. The misalignment peaks are underestimated. For case 3b, the model prediction does not capture the overshoot and higher frequency oscillations for the time $0.04\,\mathrm{s} \leq t \leq 0.4\,\mathrm{s}$. The steady state misalignment reduction is completely encompassed by the model prediction. Since the controller from section 6.2.1 is derived and tuned with the mathematical model according to chapter 3.2, unmodeled dynamic causes undesired oscillation observed for cases 2b and 3b for the time $0.04 \leq t \leq 0.6\,\mathrm{s}$. As an example for unmodeled dynamic, the adjustable supports are supposed to enable only vertical displacements in z-direction. Due to the inevitable clearance among the components of the adjustable supports to achieve adjustability, the adjustable supports tend to oscillations. This dynamic behavior of the the adjustable supports is not considered in the mathematical model from section 3.2 and, thus, not observable in the numerical simulations but in the experiments and can be assigned to model uncertainty, section 2.2.1.

Table 7.6: Measured steady state (sts.) misalignment and reduction for cases 1, 2 and 3, compare table 7.6

case	sts. misalignment $x_\mathrm{R} - x_\mathrm{L}$ in m	sts. reduction in %
1	$-0.008 \cdot 10^{-3}$	–
2a	$0.243 \cdot 10^{-3}$	–
2b	$0.119 \cdot 10^{-3}$	51
3a	$0.782 \cdot 10^{-3}$	–
3b	$0.429 \cdot 10^{-3}$	45

The semi-active load redistribution in case 2b and case 3b results in a misalignment reduction in comparison to the corresponding passive cases 2a and 3a, but there remains a steady state misalignment of the beam, figure 7.5. Beside the steady state reduction, the overshoots are slightly reduced in case 2 as well as case 3. The low frequency misalignment oscillations caused by the relative

displacement of the mass ⑩ and the beam ③ in z-direction, figure 4.1, are almost completely damped for the semi-active system but high frequency oscillations are induced. The load redistribution capability is predicted sufficiently accurate using the calibrated mathematical model from section 3.2 when considering the remaining parameter uncertainty according to chapter 5. The MC simulation results widely encompass the experimental results for both cases 2 and 3. Table 7.6 summarizes the experimental results for cases 1, 2 and 3.

Load path analysis

Additional to the misalignment in figure 7.5, the corresponding load paths are investigated. The load path of the load-bearing structure is represented by the support reaction forces F_{L} and F_{R} that are measured with the two load cells ④L and ④R and indicate how the excitation load F induced by the load mass ⑩ is distributed within the structure, figure 4.1.

Figure 7.6 depicts the load path of the load-bearing structure represented by the measured support reaction forces F_{L} and F_{R} for case 2 and case 3. Case 1 is similar to both passive cases 2a and 3a for the entire measurement time $t = 0\,\mathrm{s}$ to $t = 2\,\mathrm{s}$ and, thus, not depicted in figure 7.6. The experimental results for case 2 are indicated with dashed lines, for case 3 with solid lines. The shaded areas in figure 7.6 originate from the numerical MC simulations in figure 7.2.

In figure 7.6(a), after an overshoot at around 0.21 s and force oscillations for the time $0.04\,\mathrm{s} \leq t \leq 1.25\,\mathrm{s}$, the excitation load is approximately equally distributed to $F_{\mathrm{L}} \approx F_{\mathrm{R}} \approx 12\,\mathrm{N}$ in the steady state at $t > 1.2\,\mathrm{s}$ for case 2a. Even though, the misalignment is $x_{\mathrm{R}} - x_{\mathrm{L}} \neq 0$ for case 2a, see figure 7.5. In case 2b, the support reaction forces are $F_{\mathrm{L}} \geq F_{\mathrm{R}}$ for almost the entire simulation time $t = 0.1\,\mathrm{s}$ to $t = 2\,\mathrm{s}$. The excitation load is no longer equally distributed to the supports ①L and ①R, but depending on the support stiffness. The load redistribution results from the semi-active guidance elements with control strategy I and, consequently, results in a misalignment reduction. The steady state relief of the damaged support ①R is found to be 14 %. The shaded area of the model prediction for case 2a shows similar dynamic behavior for the entire time scale and widely encompasses the experimental results for both F_{L} and F_{R}. For case 2b, the model prediction from time $0.04\,\mathrm{s} \leq t \leq 0.5\,\mathrm{s}$ is less damped compared to the experimental results. Hence, the experimental results are not well encompassed by the shaded area. For $t > 0.5\,\mathrm{s}$, the measured steady state support reaction forces F_{L} is slightly underestimated and F_{R} is within the model prediction.

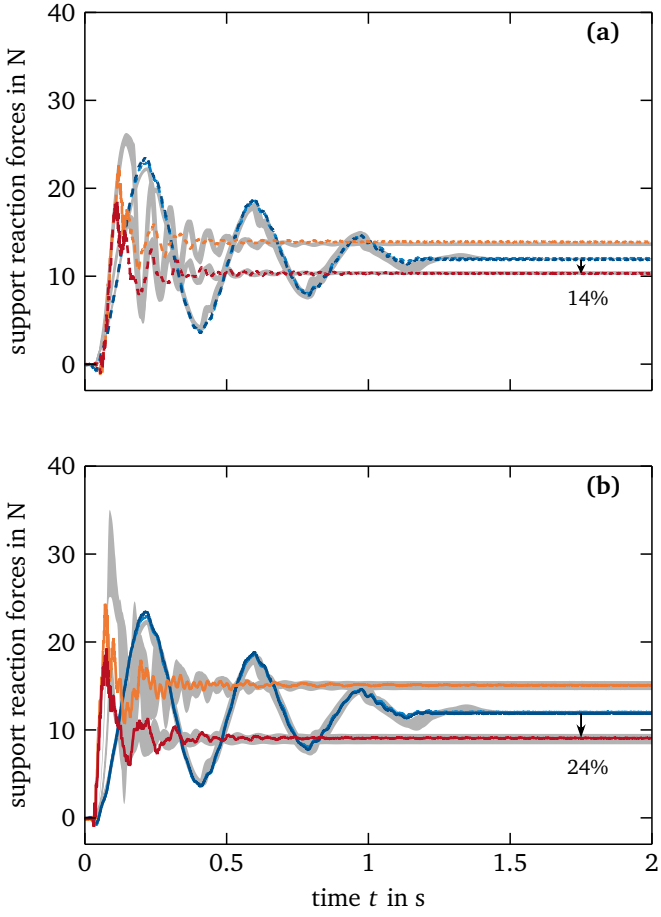

Figure 7.6: Measured support reaction forces with the simulated uncertainty ranges ( ) due to model parameter uncertainty from figure 7.2 and relief of support R, compare table 7.7, for **(a)** case 2a with F_R (– –) and F_L (– –), and case 2b with F_R (– –) and F_L (– –), and **(b)** case 3a with F_R (——) and covered F_L (——), and case 3b with F_R (——) and F_L (——)

In figure 7.6(b), after an overshoot at around 0.21 s and force oscillations from time $0.04\,\text{s} \leq t \leq 1.25\,\text{s}$, the excitation load is equally distributed to $F_L \approx F_R \approx 12\,\text{N}$

in the steady state at $t > 1.25\,\mathrm{s}$ for case 3a. Even though, the misalignment for case 3a is $x_\mathrm{R} - x_\mathrm{L} \neq 0$, see figure 7.5. In case 3b, the support reaction forces are $F_\mathrm{L} \geq F_\mathrm{R}$ for the entire time $t = 0\,\mathrm{s}$ to $t = 2\,\mathrm{s}$. The excitation load is no longer equally distributed to the supports (1L) and (1R), but depending on the support stiffness. The load redistribution results from the semi-active guidance elements with control strategy I and, consequently, results in a misalignment reduction. The steady state relief of the damaged support (1R) is found to be 24 %. The shaded area of the model prediction for case 3a shows similar dynamic behavior for the entire time scale and widely encompass the experimental results for both F_L and F_R. For case 3b, the model prediction from time $0.04\,\mathrm{s} \leq t \leq 0.4\,\mathrm{s}$ is less damped and the experimental results are widely outside the shaded area. For $t > 0.4\,\mathrm{s}$, the measured steady state support reaction forces F_L and F_R are within the model prediction. Taking into account the overall time scale, the load redistribution capability is predicted sufficiently accurate using the calibrated mathematical model from section 3.2 and considering the remaining parameter uncertainty according to chapter 5. The MC simulation results widely encompass the experimental results for both cases 2 and 3, especially for the steady state. Table 7.7 summarizes the experimental results for cases 1, 2 and 3.

Table 7.7: Measured steady state (sts.) support reaction forces (load) and support relief for cases 1, 2 and 3, compare table 7.3

	sts. load in N		
case	support (1L)	support (1R)	support (1R) relief in %
1	12.05	11.92	–
2b	13.89	10.29	14
3b	15.05	9.07	24

According to the objective for the semi-active guidance elements with control strategy I, the load is redistributed from support (1R) towards support (1L) to reduce the measured misalignment $x_\mathrm{R} - x_\mathrm{L}$ caused by the deliberate introduced uncertainty by means of the adjustable support stiffness, figure 4.5. In the passive cases 1, 2a and 3a, the load is approximately equally distributed to both supports through the predetermined load path via the spring-damper (7) only, figure 4.1. With the semi-active controlled guidance elements (8), an additional load path through the

guidance elements is technologically provided in the cases 2b and 3b that redistributes a portions of the load as may be required by varying support stiffness. Experimental and numerical results prove the capability of load redistribution for SHC via the semi-active guidance elements to reduce misalignment in cases with a damaged support.

7.3.2 Defined load ratio: cases 1 and 4

As numerically investigated in section 7.2.2 for the cases 1 and 4 from table 7.1, the control strategy II from section 6.1.2 is applied with the semi-active guidance elements to achieve a desired load ratio κ by redistributing the loads from support (1R) to support (1L) in the experimental test setup, figure 4.1. In case 4, the load ratio set point is chosen to be $\kappa = 2$ for the following experimental investigation, that is, the support (1L) is supposed to bear twice the load compared to support (1R). In order to evaluate the load redistribution capability of the semi-active guidance elements, first the support reaction force ratio and second the load path represented by the support reaction forces F_L and F_R are analyzed and compared to the numerical MC simulations from section 7.2.2.

Support reaction force ratio analysis

Figure 7.7 depicts the measured support reaction force ratio $|F_\mathrm{L}|/|F_\mathrm{R}|$ due to the excitation via the load mass (10), figure 4.1, for cases 1 and 4. Case 1 serves as reference with a support reaction force ratio $|F_\mathrm{L}|/|F_\mathrm{R}| \approx 1$ for the entire measurement time $t = 0\,\mathrm{s}$ to $t = 2\,\mathrm{s}$. The shaded area in figure 7.7 originate from the numerical MC simulations in figure 7.3. The ordinate is scaled logarithmic to capture the fact that the ratio $\kappa = 2$ and $\kappa = 0.5$ represent the same load ratio with different directions, i.e. right to left and left to right.

In figure 7.7, after oscillations from time $0.0 \leq t \leq 1.2\,\mathrm{s}$, the steady state support reaction force ratio $|F_\mathrm{L}|/|F_\mathrm{R}|$ ensues at 1.78 for case 4. Since the controller from section 6.2.2 is derived and tuned with the mathematical model according to chapter 3.2, unmodeled dynamic causes undesired oscillations observed for case 1 and case 4 for the time $0.0 \leq t \leq 1.2\,\mathrm{s}$, similar to cases 2b and 3b in section 7.3.1. Also, the calculation of the reaction force ratio $|F_\mathrm{L}|/|F_\mathrm{R}|$ is sensitive to zero crossings of $|F_\mathrm{R}|$ since $|F_\mathrm{R}|$ represents the denominator when calculating the reaction force ratio. Measurement noise can lead to zero crossings and, thus, to noise in the calculated reaction force ratio $|F_\mathrm{L}|/|F_\mathrm{R}|$ as observed in the experimental results for case 1 in particular for the time $0.0 \leq t \leq 0.7\,\mathrm{s}$ before and during the load

mass ⑩ is released. The shaded area of the model prediction for case 4 shows similar dynamic behavior for the entire time scale. Even though, oscillations for the time $0.13 \leq t \leq 0.9\,\mathrm{s}$ appear in the model predictions but are not observed experimentally. Hence, the experimental results are outside the shaded area of the model prediction for the time $0.13 \leq t \leq 0.9\,\mathrm{s}$. For $t > 1\,\mathrm{s}$, the measured steady state support reaction force ratio $|F_\mathrm{L}|/|F_\mathrm{R}|$ is again encompassed by the model prediction.

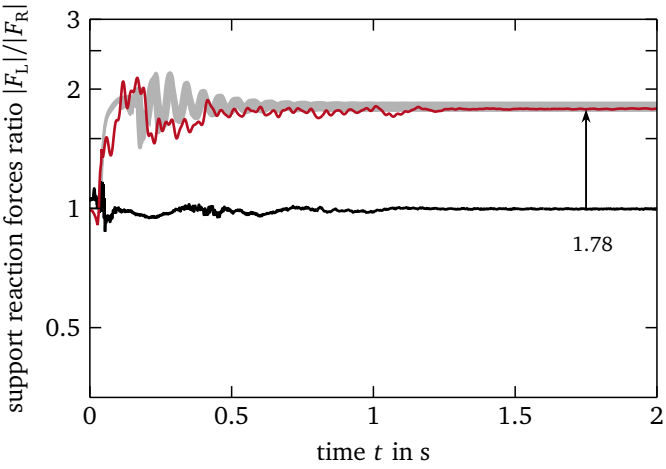

Figure 7.7: Measured support reaction force ratio, compare table 7.8, with the simulated uncertainty range ( ) due to model parameter uncertainty from figure 7.3 for case 1 (——) and case 4 (——), logarithmic ordinate

The semi-active load redistribution in case 4 results in an approximation to the defined load ratio $\kappa = 2$, but there remains a steady state control deviation. The load is redistributed from support ⑴R towards support ⑴L to reach the defined load ratio $\kappa = 2$ as close as possible subjected to limitations associated to the semi-activity of the guidance elements, section 6.2.

The load redistribution capability is predicted sufficiently accurate using the calibrated mathematical model from section 3.2 and considering the remaining parameter uncertainty according to chapter 5. The MC simulation results widely encompass the experimental results for case 4 and $t \leq 0.4\,\mathrm{s}$. Table 7.8 summarizes the experimental results for cases 1 and 4.

Table 7.8: Measured steady state (sts.) support reaction force ratio for cases 1 and 4, compare figure 7.5

case	sts. support reaction force ratio
1	0.99
4	1.78

Load path analysis

Figure 7.8 depicts the load path of the load-bearing structure for cases 1 and 4 corresponding to the support reaction force ratio $|F_L|/|F_R|$ in figure 7.7. The shaded areas in figure 7.8 originate from the numerical MC simulations in figure 7.2. In case 4, the support reaction forces are $F_L \geq F_R$ for the entire measurement time $0\,s \leq t \leq 2\,s$. The support (1L) has to bear additional load and the support (1R) is relieved. The load redistribution results from the semi-active guidance elements with control strategy II and, consequently, result in an approximation to the desired load ration $\kappa = 2$. The steady state relief of the support (1R) is found to be 29 %.

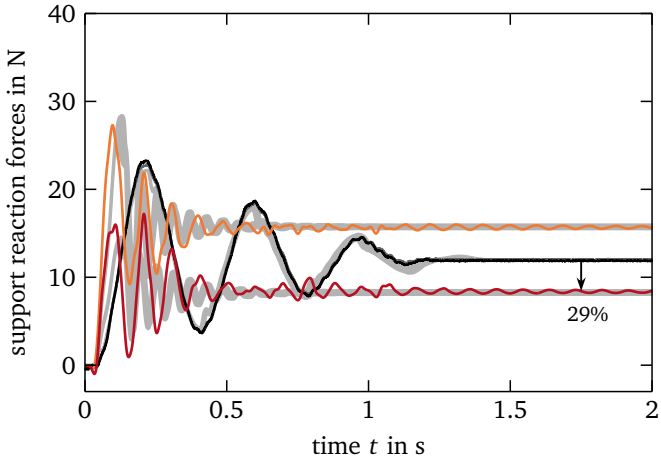

Figure 7.8: Measured support reaction forces with the simulated uncertainty ranges ( ) due to model parameter uncertainty from figure 7.4 and relief of support R, compare table 7.5, for case 1 with almost identical F_R (——) and F_L (——), and case 4 with F_R (——) and F_L (——)

In figure 7.8, the shaded area of the model prediction for case 1 shows similar dynamic behavior for the entire time scale and widely encompasses the experimental results for both reaction forces F_L and F_R. For case 4, the shaded areas of the model prediction generally exhibits similar dynamic behavior but with deviations in the peak values and a 0.04 s phase lag for the time $0.05\,\text{s} \leq t \leq 0.5\,\text{s}$. For $t > 0.5\,\text{s}$, the measured steady state support reaction forces F_L and F_R are widely encompassed by the model prediction even though oscillating in contrast to the model predictions. Table 7.9 summarizes the experimental results for cases 1 and 4.

Table 7.9: Measured steady state (sts.) support reaction forces (load) and support relief for cases 1 and 4, compare table 7.5

	sts. load in N		
case	support (1L)	support (1R)	support (1R) relief in %
1	12.05	11.88	–
4	15.63	8.42	29

According to the objective for the semi-active guidance elements with control strategy II, the load is redistributed from support (1R) towards support (1L) in order to change the predetermined load path and achieve the defined load ratio κ, section 6.1.2, and, thus, reduce the uncertainty of an inappropriate load path by future damage. In the passive case 1, the load is equally distributed to both supports (1L) and (1R) through the predetermined load path via the spring-damper (7) only, figure 4.1. With the semi-active controlled guidance elements (7) in case 4, an additional load path through the guidance elements is provided that redistributes a portion of the load as may be required to change the support reaction force ratio $|F_L|/|F_R|$. Experimental and numerical results prove the capability of load redistribution for SHC via the semi-active guidance elements in order to precautionary change the load path and to achieve the defined load ratio.

Both control strategies I and II result in similar changes in the support reaction forces F_L and F_R since in both control strategies the right support (1R) is supposed to be relieved in order to reduce the control deviations (6.1) and (6.2), respectively. Also, the numerically calculated shaded uncertainty areas of the model prediction widely encompass the experimental results or at least exhibit quite similar behavior between simulations and measurements for both control strategies I and II.

7.4 Summary and discussion of results

This chapter presents a case study with 4 cases, table 7.1, in order to investigate the load redistribution capability for SHC numerically by means of the calibrated mathematical model, section 3.2 and chapter 5, and experimentally by means of the experimental test setup, section 4. The cases differ in severity of support damage and the applied control strategy.

Control strategy I aims to reduce the beam misalignment that is defined as malfunction in the scope of this thesis. The beam misalignment is caused by a damaged support with reduced stiffness. Control strategy I is applied to cases 1, 2 and 3 with increasing severity of support damage from case 1 to 3. The case 1 serves as undamaged reference. The relative misalignment reduction is similar for different severities of damage. Numerically, the misalignment reduction is found to be between 42% and 49% for case 2 and between 38% and 53% for case 3 comparing semi-active and passive systems. Experimentally, the misalignment reduction is 51% for case 2 and 45% for case 3 comparing semi-active and passive systems. The load path is evaluated by means of the support reaction forces F_{L} and F_{R} and is similar in both cases 2 and 3. The load is redistributed towards the undamaged support and the damaged support is relieved. Nevertheless, it remains a steady state control deviation in both cases 2 and 3 for the simulation results and the experimental results. This is most probably due to the limitations of the semi-active approach, which cannot contribute energy into the structure via the friction brakes to completely eliminate the control deviation, compare section 6.2. Additionally, the geometric limitations, i.e. the position of guidance elements connection points, figure 3.4(a), prevent higher load redistribution capability.

Control strategy II aims to achieve a desired load ratio among the supports by changing the predetermined load path and is applied to cases 1 and 4. The case 1 serves as uncontrolled reference whereas in case 4 the load path is supposed to be changed to achieve a desired load ratio. Numerically, the steady state load ratio ensues between 1.76 and 1.85 for the set point load ratio $\kappa = 2$. Experimentally, the steady state load ratio is 1.78. It remains a steady state control deviation for the simulation results and the experimental results. This is, again, caused by the limitations of the semi-active approach. However, the load path in case 4 is similar to the load paths of cases 2 and 3 since the load is redistributed to match the desired load ratio $\kappa = 2$.

Both control strategies I and II numerically and experimentally prove their capability of load redistribution in the case study. The experimental results ex-

hibit basically a similar behavior as simulation results. Remaining partly differences between simulation and experiment are attributed to model discrepancy or model uncertainty, section 2.2.1, and cannot be further reduced via parameter calibration according to section 5.1. Nevertheless, the mathematical model with calibrated model parameters exhibits a reasonable prediction accuracy with uncertainty bounds widely encompassing the experimental results.

8 Conclusion and outlook

In this thesis, uncertainty in a novel semi-active concept for load redistribution in a load-bearing structure and in the numerical prediction of the load redistribution capability of the concept has been investigated and evaluated numerically and experimentally. The necessity for redistributing loads arises if parts of the load-bearing structure become weak or suffer damage, e.g. due to deterioration or overload, and, hence, the load-bearing capacity of a load path becomes uncertain. The proposed concept augments existing guidance elements of the load-bearing structure with friction brakes to provide additional load paths and enables load redistribution for Structural Health Control (SHC). Clipped-optimal controllers were successfully applied to adapt the load path to changed load-bearing capacity. Furthermore, uncertainty quantification and reduction in numerical model predictions was achieved via statistical measures for parameter calibration. In particular, the parameters of the mathematical model of the load-bearing structure were calibrated and their uncertainty was quantified with the BAYESIAN inference approach to allow the evaluation of the numerically predicted load redistribution capability and a comparison to experimental results.

Transmitting loads through a predetermined load path to structural supports with simultaneously enabling specified displacement trajectories of structural components are typical features of load-bearing systems, e.g. an airplane's landing gear. A comprehensive literature review showed that most previous studies focus on enhancing the vibration behavior or increasing the load-bearing capacity by means of semi-active or active adaptive measures. In the design process, optimizing structural components or the load path in general according to expected loads is a commonly applied passive approach to ensure functional performance. Load redistribution to relieve weak or damaged parts of load-bearing structures during operation has not been addressed in either case.

Variability in the model predictions caused by parameter uncertainty needs to be quantified and reduced to increase the model's credibility and its usability for designing load-bearing structures and for controller synthesis. Although a wide variety of measures for uncertainty quantification and reduction in model predictions is found in literature, parameter uncertainty quantification and reduction for a model of a load-bearing structure with semi-active load redistribution has not been considered so far.

The investigated load-bearing structure in this thesis is based on the load-bearing structure developed within the SFB 805 and consists of a translational moving mass connected to a rigid beam by a spring-damper system and two semi-active guidance elements with the ability to redistribute loads according to the proposed concept. The beam is supported at its ends by two supports. The stiffness characteristic of the supports can be adjusted to simulate structural damage with reduced support stiffness. The semi-active guidance elements can provide additional load paths to relieve the damaged parts of the structure. This load-bearing structure was used to numerically and experimentally evaluate the load redistribution capability with semi-active friction brakes in the guidance elements to provide additional load paths. An experimental test setup of the load-bearing structure was designed to investigate the load redistribution capability based on measured data. A step-like dynamic load was applied to the load-bearing structure as excitation. In order to redistribute the load between the two supports via the semi-active guidance elements, two different control strategies were tested. Combined with a clipped-optimal linear-quadratic regulator (LQR), control strategy I aims to reduce undesired beam misalignment that is defined as malfunction and is caused by a damaged support. Combined with a clipped-optimal PID controller, control strategy II aims to precautionary achieve a desired load ratio between the supports before a damage occurs. Additionally, the load path was analyzed and evaluated by means of the resulting support reaction forces.

For controller design and to predict the dynamic behavior, the mathematical model of the load-bearing structure with semi-active guidance elements is derived. It consists of two models parts, i.e. the model of the load-bearing structure comprising the mechanical components like the translational moving mass and the beam and the model of the semi-active guidance elements comprising the electromagnetic actuators and the LuGre-friction model. The derived mathematical models contain model parameters that need to be calibrated utilizing experimental data. Therefore, the Bayesian inference based calibration procedure was used to increase the model prediction accuracy and to adjust the model parameters to the actual loading conditions. After selecting the most influential model parameters for calibration according to their sensitivity and uncertainty, the model parameter uncertainty was quantified and reduced by systematic inference of the posterior distribution. The posterior parameter distributions were approximated by means of Markov Chain Monte Carlo (MCMC) sampling resulting in histograms with quantified and reduced uncertainty for each calibrated model parameter. The model prediction variation due to parameter uncertainty is reduced up to 56% for the mathematical model of the load-bearing structure and up to 85% for the LuGre-friction model. The clipped-optimal LQR and PID controllers for semi-active load redistribution were eventually tuned by means of the mathematical model with

calibrated parameters and finally applied in the numerical and experimental investigations.

The load redistribution capability of the semi-active guidance elements was investigated and evaluated by means of a case study. The considered cases differ in the assumed severity of the support damage, represented by an appropriate stiffness reduction of the affected support, and the applied control strategy. Comparing simulations and measurements of passive and semi-active systems in the time domain, control strategy I reduces the steady state misalignment of the beam between 38% and 53% numerically and between 45% and 51% experimentally. The evaluation of the load path exhibits a redistribution of the load towards the undamaged support according to the control strategy I. The load ratio among the two supports is changed by applying control strategy II. A desired set point load ratio of 2 leads to steady state load ratios between 1.76 and 1.85 numerically and a load ratio of 1.78 experimentally. The evaluation of the load path exhibits a redistribution of the load between the two support to achieve the desired load ratio.

In summary, the load redistribution capability was proven numerically and experimentally in all cases considered of the case study. The load was successfully redistributed according to the applied control strategy. Parts of the load-bearing structure could be relieved whereas other parts had to bear the additional loading. Furthermore, basically the same behavior for numerical and experimental results were observed. Due to the model parameter calibration via BAYESIAN inference and the considered parameter uncertainty in the numerical MONTE CARO (MC) simulations, the uncertainty bounds of the numerical results widely encompass the experimental results. Hence, the mathematical model with calibrated parameters exhibits a reasonable prediction accuracy for the load redistribution capability.

Future objectives based on findings in this thesis arise regarding the application limitations, the controller improvement and uncertainty quantification methods. The results for the semi-active load redistribution presented in this thesis are limited to the investigated planar load-bearing structure. Therefore, a future objective is the implementation of the semi-active guidance elements into a spatial load-bearing structure to prove and evaluate the load redistribution capability in such a structure. The controller may be improved regarding the performance and the considered excitation loads. The used controller type may be augmented for performance improvements, e.g. to a linear-quadratic-GAUSSIAN (LQG) control with integrated observer for the friction states. It may also be worth to consider different excitation load types, such as stochastic or harmonic loads, in future control design. Furthermore, the remaining model discrepancy after model parameter calibration may be used to develop a metric for model uncertainty quantification and to identify missing physics or oversimplifications in the model.

References

[1] Adamy, J. *Nichtlineare Systeme und Regelungen*. Berlin, Heidelberg: Springer Berlin Heidelberg, 2014.

[2] Adamy, J. *Systemdynamik und Regelungstechnik II*. 4. Aufl. Berichte aus der Steuerungs- und Regelungstechnik. Aachen: Shaker, 2013.

[3] Albrecht, H. *Adaptive Verbindungselemente im Leichtbau*. Dissertation. Stuttgart: Universität Stuttgart, 2005.

[4] Altpeter, F. *Friction Modeling, Identification and Compensation*. PhD thesis. Lusanne: École Polytechnique Fédéral de Lausanne, 1999.

[5] Anderson, J. R. and Ferri, A. A. *Behavior of a single-degree-of-freedom system with a generalized friction law*. In: *Journal of Sound and Vibration* 140.2 (1990), pp. 287–304.

[6] *Assessing the reliability of complex models: Mathematical and statistical foundations of verification, validation, and uncertainty quantification*. Washington, D.C: National Academies Press, 2012.

[7] Atamturktur, S., Hemez, F. M., and Laman, J. A. *Uncertainty quantification in model verification and validation as applied to large scale historic masonry monuments*. In: *Engineering Structures* 43 (2012), pp. 221–234.

[8] Atamturktur, S. et al. *A forecasting metric for predictive modeling*. In: *Computers & Structures* 89.23-24 (2011), pp. 2377–2387.

[9] Bayes, T. *An essay towards solving a problem in the doctrine of chances. By the late Rev. Mr. Bayes, F. R. S. communicated by Mr. Price, in a letter to John Canton, A. M. F. R. S*. In: *Philosophical Transactions of the Royal Society of London* 53 (1763), pp. 370–418.

[10] Becker, F. B. *Aktive Wälzlagerung zur Reduktion von Rotorschwingungen*. Dissertation. Darmstadt: Technische Universität Darmstadt, 2017.

[11] Bedarff, T. *Grundlagen der Entwicklung und Untersuchung einer aktiven Luftfeder für Personenkraftwagen*. Dissertation. Darmstadt: Technische Universität Darmstadt, 2016.

[12] Bendsøe, M. P., Ben-Tal, A., and Zowe, J. *Optimization methods for truss geometry and topology design*. In: *Structural optimization* 7 (1994), pp. 141–159.

[13] Berger, E. J. *Friction modeling for dynamic system simulation*. In: *Applied Mechanics Reviews* 55.6 (2002), p. 535.

[14] Birkhofer, H. and Nordmann, R. *Maschinenelemente und Mechatronik*. 3., überarb. Aufl. Vorlesungen Mechatronik & Maschinenakustik. Aachen: Shaker, 2003.

[15] Birkhofer, H. and Nordmann, R. *Maschinenelemente und Mechatronik II*. 3. überarb. Aufl. Skripte. Aachen: Shaker, 2008.

[16] Bleuler, H. et al. *Application of digital signal processors for industrial magnetic bearings*. In: *IEEE Transactions on Control Systems Technology* 2.4 (1994), pp. 280–289.

[17] Canudas de Wit, C. and Lischinsky, P. *Adaptive friction compensation with partially known dynamic friction model*. In: *International Journal of Adaptive Control and Signal Processing* 11.1 (1997), pp. 65–80.

[18] Canudas de Wit, C. et al. *A new model for control of systems with friction*. In: *IEEE Transactions on Automatic Control* 40.3 (1995), pp. 419–425.

[19] Choi, S.-K., Grandhi, R. V., and Canfield, R. A. *Reliability-based Structural Design*. London: Springer-Verlag, 2007.

[20] Christie, M. A. et al. *Error Analysis and Simulations of Complex Phenomena*. In: *Los Alamos Science* 29 (2005), pp. 6–25.

[21] DIN Deutsches Institut für Normung e. V. *Allgemeine Leitsätze für das sicherheitsgerechte Gestalten von Produkten (engl.: General principles for the safe design of products)*. 01.04.2017.

[22] Do, A. L. et al. *An LPV control approach for comfort and suspension travel improvements of semi-active suspension systems: (CDC) ; 15 - 17 Dec. 2010*. Piscataway, NJ: IEEE, 2010.

[23] Do, N. B., Ferri, A. A., and Bauchau, O. A. *Efficient Simulation of a Dynamic System with LuGre Friction*. In: *Journal of Computational and Nonlinear Dynamics* 2.4 (2007), p. 281.

[24] Dodge, Y., ed. *The concise encyclopedia of statistics*. [Updated ed.] Springer reference. New York, NY: Springer, 2010.

[25] Dyke, S. J. *Acceleration Feedback Control Strategies for Active and Semi-active Control Systems: Modeling, Algorithm development, and experimental verification*. Dissertation. Indiana, USA: University of Notre Dame, 1996.

[26] Dyke, S. J. et al. *An experimental study of MR dampers for seismic protection*. In: *Smart Materials and Structures* 7.5 (1998), pp. 693–703.

[27] Dyke, S. J. et al. *Modeling and control of magnetorheological dampers for seismic response reduction*. In: *Smart Materials and Structures* 5.5 (1996), pp. 565–575.

[28] Eck, V. G. et al. *A guide to uncertainty quantification and sensitivity analysis for cardiovascular applications*. In: *International journal for numerical methods in biomedical engineering* 32.8 (2016).

[29] Eifler, T. et al. *Approach for a Consistent Description of Uncertainty in Process Chains of Load Carrying Mechanical Systems*. In: *Applied Mechanics and Materials* 104 (2011), pp. 133–144.

[30] Engelhardt, R. A. et al. *A Model to Categorise Uncertainty in Load-Carrying Systems*. In: *Proceedings of the 1st International Conference on Modelling and Management of Engineering Processes (MMEP 2010)*. Ed. by Heisig, P., Clarkson, P. J., and Vajna, S. Cambridge/UK: Springer-Verlag London, 2010, pp. 53–64.

[31] Enss, G. C. *Beherrschung von Unsicherheit am Beispiel eines aktiv gegen Knicken stabilisierten Systems*. Dissertation. Darmstadt: Technische Universität Darmstadt, 2016.

[32] Enss, G. C. et al. *Device for bearing design elements in lightweight structures (Festkörperlager)*. DE 10 2015 101 084 A1.

[33] Enss, G. C. et al. *Device for optimal load transmission and load distribution in lightweight structures (Kraftübertragungsvorrichtung)*. DE 10 2014 106 858 A1.

[34] Farajpour, I. *Constrained optimization of structures with displacement constraints under various loading conditions*. In: *Advances in Engineering Software* 41 (2010), pp. 580–589.

[35] Fonseca, J., Mares, C. F. M., and Mottershead, J. E. *Review of Parameter Uncertainty Propagation Methods in Structural Dynamic Analysis*. In: *ISMA 27, Leuven, Belgium*. Ed. by Sas, P. and van Hal, B. 2002.

[36] Freund, T. *Konstruktionshinweise zur Konstruktionshinweise zur Beherrschung von Unsicherheit in technischen Systemen*. Dissertation. Darmstadt: Technische Universität Darmstadt, 2018.

[37] Gattiker, J. R. *Gaussian Process Models for Simulation Analysis (GPM/SA): Command, Function, and Data Structure Reference: LA-UR-08-08057*. 2008.

[38] Gaul, L., Albrecht, H., and Wirnitzer, J. *Semi-Active Friction Damping of Large Space Truss Structures*. In: *Shock and Vibration* 11.3-4 (2004), pp. 173–186.

[39] Gaul, L. and Nitsche, R. *Friction Control for Vibration Suppression*. In: *Mechanical Systems and Signal Processing* 14.2 (2000), pp. 139–150.

[40] Gaul, L. and Nitsche, R. *The Role of Friction in Mechanical Joints*. In: *Applied Mechanics Reviews* 54.2 (2001), p. 93.

[41] Gaul, L. et al. *Enhanced damping of lightweight structures by semi-active joints*. In: *Acta Mechanica* 195.1-4 (2008), pp. 249–261.

[42] Gehb, C. M., Platz, R., and Melz, T. *Active load path adaption in a simple kinematic load-bearing structure due to stiffness change in the structure's supports*. In: *Journal of Physics: Conference Series* 744.1 (2016), p. 012168.

[43] Gehb, C. M., Platz, R., and Melz, T. *Approach to prevent locking in a spring-damper system by adaptive load redistribution in auxiliary kinematic guidance elements*. In: *Proc. SPIE 9433, Industrial and Commercial Applications of Smart Structures Technologies 2015*. Vol. 9433. San Diego, USA, 2015, 94330G-94330G-9.

[44] Gehb, C. M., Platz, R., and Melz, T. *Global Load Path Adaption in a Simple Kinematic Load-Bearing Structure to Compensate Uncertainty of Misalignment Due to Changing Stiffness Conditions of the Structure's Supports*. In: *Model Validation and Uncertainty Quantification, Volume 3*. Ed. by Barthorpe Robert J. et al. Conference proceedings of the Society for Experimental Mechanics series. Cham: Springer International Publishing, 2017, pp. 133–144.

[45] Gehb, C. M., Platz, R., and Melz, T. *Two control strategies for semi-active load path redistribution in a load-bearing structure*. In: *Mechanical Systems and Signal Processing* 118 (2019), pp. 195–208.

[46] Gehb, C. M. et al. *Bayesian inference based parameter calibration of the LuGre-friction model*. In: *Experimental Techniques* (2019), in press.

[47] Götz, B. *Evaluation of uncertainty in the vibration attenuation with shunted piezoelectric transducers integrated in a beam-column support*. Dissertation. Darmstadt: Technische Universität Darmstadt, 2018.

[48] Götz, B. et al. *Optimal tuning of shunt parameters for lateral beam vibration attenuation with three collocated piezoelectric stack transducers*. In: *6th European Conference on Structural Control*. 2016, p. 12.

[49] Graham, C. and Talay, D. *Stochastic Simulation and Monte Carlo Methods: Mathematical Foundations of Stochastic Simulation*. Vol. 68. Stochastic Modelling and Applied Probability. Berlin, Heidelberg and s.l.: Springer Berlin Heidelberg, 2013.

[50] Green, P. L. and Worden, K. *Modelling Friction in a Nonlinear Dynamic System via Bayesian Inference*. In: *Special Topics in Structural Dynamics, Volume 6*. Ed. by Allemang, R. et al. New York, NY: Springer New York, 2013, pp. 543–553.

[51] Hagedorn, P. *Technische Mechanik Band 3: Dynamik*. 3., überarb. und erw. Aufl. Harri Deutsch, 2006.

[52] Hanselka, H. and Platz, R. *Ansätze und Maßnahmen zur Beherrschung von Unsicherheit in lasttragenden Systemen des Maschinenbaus: Controlling Uncertainties in Load Carrying Systems*. In: *VDI-Zeitschrift Konstruktion* 11/12-2010 (2010), pp. 55–62.

[53] Hansmann, J. et al. *Einstellbares Federelement für Adaptierbaren Schwingungstilger*. In: *ATZ - Automobiltechnische Zeitschrift* 114.3 (2012), pp. 242–247.

[54] Hedrich, P. et al. *Comparison of a New Passive and Active Technology for Vibration Reduction of a Vehicle under Uncertain Load*. In: *Applied Mechanics and Materials* 807 (2015), pp. 57–66.

[55] Heo, Y. *Bayesian calibration of building energy models for energy retrofit decision-making under uncertainty*. Dissertation. Georgia Institute of Technology, 2011.

[56] Herold, S., Jungblut, T., and Kurch, M. *A Systematic Approach to Simulate Active Mechanical Structures*. In: *Multi-Disciplinary Simulations - The Future of Virtual Product Development*. 2009.

[57] Higdon, D. et al. *Computer Model Calibration Using High-Dimensional Output*. In: *Journal of the American Statistical Association* 103.482 (2008), pp. 570–583.

[58] Hurlebaus, S. and Gaul, L. *Smart structure dynamics*. In: *Mechanical Systems and Signal Processing* 20.2 (2006), pp. 255–281.

[59] Isermann, R. *Mechatronische Systeme: Grundlagen*. 2., vollst. neu bearb. Aufl. Berlin: Springer-Verlag Berlin Heidelberg and Springer, 2008.

[60] Jansen, L. M. and Dyke, S. J. *Semiactive Control Strategies for MR Dampers: Comparative Study*. In: *Journal of Engineering Mechanics* 126.8 (2000), pp. 795–803.

[61] Joghataie, A. *Active Control of Trusses Under Heavy Static Loads*. In: *Neural Network World* 11.3 (2001), pp. 285–292.

[62] Kallenbach, E. et al. *Elektromagnete: Grundlagen, Berechnung, Entwurf und Anwendung*. 5. Auflage. Wiesbaden: Springer Vieweg, 2018.

[63] Kennedy, M. C. and O'Hagan, A. *Bayesian calibration of computer models*. In: *Journal of the Royal Statistical Society: Series B (Statistical Methodology)* 63.3 (2001), pp. 425–464.

[64] Kikuuwe, R. et al. *Fixed-step friction simulation: from classical Coulomb model to modern continuous models*. In: *IEEE/RSJ International Conference on Intelligent Robots and Systems*. 2005, pp. 1009–1016.

[65] Knetsch, T. *Unsicherheiten in Ingenieurberechnungen*. PhD thesis. Otto-von-Guericke-Universität Magdeburg, 2004.

[66] Kraus, R. et al. *Development of Active Engine Mounts Based on Piezo Actuators*. In: *ATZ worldwide* 116.1 (2014), pp. 46–51.

[67] Kuypers, F. *Klassische Mechanik*. Wiley, 2016.

[68] Lemaire, M. *Mechanics and uncertainty*. Mechanical engineering and solid mechanics series. Hoboken, NJ and London: Wiley and ISTE, 2014.

[69] Lemaitre, C. *Topologieoptimierung von adaptiven Stabwerken*. Dissertaion. Stuttgart: Universität Stuttgart, 2008.

[70] Li, S. and Platz, R. *Observations by Evaluating the Uncertainty of Stress Distribution in Truss Structures Based on Probabilistic and Possibilistic Methods*. In: *Journal of Verification, Validation and Uncertainty Quantification* 2.3 (2017), p. 031006.

[71] Li, W. et al. *Integrating Bayesian Calibration, Bias Correction, and Machine Learning for the 2014 Sandia Verification and Validation Challenge Problem*. In: *Journal of Verification, Validation and Uncertainty Quantification* 1.1 (2016), p. 2375.

[72] Liu, D.-P. *Parameter Identification for LuGre Friction Model using Genetic Algorithms*. In: *Proceedings of 2006 International Conference on Machine Learning and Cybernetics*. Piscataway NJ: IEEE, 2006.

[73] Lunze, J. *Regelungstechnik 2: Mehrgrößensysteme, digitale Regelung*. 5., neu bearbeitete Aufl. Springer-Lehrbuch. Berlin: Springer-Verlag Berlin Heidelberg, 2008.

[74] Mace, B. R., Vandepitte, D. V. H., and Lardeur, P. *Uncertainty in structural dynamics*. In: *Finite Elements in Analysis and Design* 47.1 (2011), pp. 1–3.

[75] Mallapur, S. and Platz, R. *Quantification and Evaluation of Uncertainty in the Mathematical Modelling of a Suspension Strut Using Bayesian Model Validation Approach*. In: *Model Validation and Uncertainty Quantification, Volume 3*. Ed. by Barthorpe Robert J. et al. Conference proceedings of the Society for Experimental Mechanics series. Cham: Springer International Publishing, 2017, pp. 113–124.

[76] Marelli, S. and Sudret, B. *UQLAB: a framework for Uncertainty Quantification in MATLAB*. In: *Vulnerability, Uncertainty, and Risk*. Ed. by Beer, M., Au, S.-K., and Hall, J. W. American Society of Civil Engineers, 2014, pp. 2554–2563.

[77] Marhadi, K. S., Venkataraman, S., and Wong, S. A. *Load redistribution mechanism in damage tolerant and redundant truss structure*. In: *Structural and Multidisciplinary Optimization* 44.2 (2011), pp. 213–233.

[78] Markert, R. *Strukturdynamik*. Mechanik. Aachen: Shaker, 2013.

[79] Maslen, E. H. and Schweitzer, G. *Magnetic Bearings: Theory, Design, and Application to Rotating Machinery*. Berlin, Heidelberg: Springer-Verlag Berlin Heidelberg, 2009.

[80] Matthew Riddle and Ralph T. Muehleisen. *A Guide to Bayesian Calibration of Building Energy Models*. In: *ASHRAE/IBPSA-USA*. 2014.

[81] Melz, T., Hanselka, H., and Matthias, M. *Adaptronische Systeme für automotive Anwendungen am Beispiel eines modularen, aktiven Strukturinterfaces (Smart Structures for Automotive Applications with the Example of a Modular Active Interface)*. In: *at - Automatisierungstechnik* 54.6/2006 (2006).

[82] Mitiguy, P. C. and Banerjee, A. K. *Efficient Simulation of Motions Involving Coulomb Friction*. In: *Journal of Guidance, Control, and Dynamics* 22.1 (1999), pp. 78–86.

[83] Mollineaux, M. G. et al. *Simulating the dynamics of wind turbine blades: Part I, model development and verification*. In: *Wind Energy* 16.5 (2013), pp. 694–710.

[84] Myers, K. et al. *A detailed example of using the GPM/SA code*. 2012.

[85] Nagel, J. B. *Bayesian techniques for inverse uncertainty quantification*. Dissertation. Zürich: ETH Zürich, 2017.

[86] Nordmann, R. *Mechatronische Systeme im Maschinenbau I*. Vorlesungen Mechatronik & Maschinenakustik. Aachen: Shaker, 2001.

[87] Oberkampf, W. L., Trucano, T. G., and Hirsch, C. *Verification, Validation, and Predictive Capability in Computational Engineering and Physics*. In: (2002).

[88] Oberkampf, W. L. et al. *Error and uncertainty in modeling and simulation*. In: *Reliability Engineering and System Safety* 75 (2002), pp. 333–357.

[89] Olsson, H. et al. *Friction Models and Friction Compensation*. In: *European Journal of Control* 4.3 (1998), pp. 176–195.

[90] Pahl, G. et al. *Konstruktionslehre: Grundlagen erfolgreicher Produktentwicklung Methoden und Anwendung*. 6. Aufl. Springer-Lehrbuch. Berlin and Heidelberg: Springer-Verlag Berlin Heidelberg, 2005.

[91] Palazzolo, A. B. et al. *Piezoelectric Pushers for Active Vibration Control of Rotating Machinery*. In: *Journal of Vibration and Acoustics* 111.3 (1989), pp. 298–305.

[92] Pauly, D. E. *Power Supply Magnetics: Part I: Selecting Transformer/Inductor Core Material*. In: *PCIM Magazine* (1996).

[93] Piatkowski, T. *Dahl and LuGre dynamic friction models — The analysis of selected properties*. In: *Mechanism and Machine Theory* 73 (2014), pp. 91–100.

[94] Pilotto, R. et al. *Use of Magnetic Bearings in Vibration Control of a Steam Turbine with Oil-Film Bearings*. In: *International Congress on Sound and Vibration*. 2017, pp. 1–8.

[95] Platz, R., Stapp, C., and Hanselka, H. *Statistical approach to evaluating active reduction of crack propagation in aluminum panels with piezoelectric actuator patches*. In: *Smart Materials and Structures* 20.8 (2011), p. 085009.

[96] Preumont, A. and Seto, K. *Active control of structures*. Chichester, U.K: John Wiley, 2008.

[97] Rajan, S. *Sizing, Shape, and Topology Design Optimization of Trusses Using Genetic Algorithm*. In: *Journal of Structural Engineering* 121 (1995), pp. 1480–1487.

[98] Roy, C. J. and Oberkampf, W. L. *A Complete Framework for Verification, Validation, and Uncertainty Quantification in Scientific Computing (Invited)*. In: *48th AIAA Aerospace Sciences Meeting Including the New Horizons Forum and Aerospace Exposition, Orlando, Florida*. 2010.

[99] Roy, C. J. and Oberkampf, W. L. *A comprehensive framework for verification, validation, and uncertainty quantification in scientific computing*. In: *Computer Methods in Applied Mechanics and Engineering* 200.25-28 (2011), pp. 2131–2144.

[100] Saltelli, A. *Global sensitivity analysis: The primer*. Chichester, England and Hoboken, NJ: John Wiley, 2008.

[101] Schaeffner, M. *Quantification and evaluation of uncertainty in active buckling control of a beam-column subject to dynamic axial loads*. Dissertation. Darmstadt: Technische Universität Darmstadt, 2019.

[102] Schaeffner, M., Götz, B., and Platz, R. *Active buckling control of a beam-column with circular cross-section using piezo-elastic supports and integral LQR control*. In: *Smart Materials and Structures* 25.6 (2016), pp. 1–10.

[103] Schaeffner, M., Platz, R., and Melz, T. *Active buckling control of an axially loaded beam-column with circular cross-section by active supports with integrated piezoelectric actuators*. In: *Proceedings of SMART2015*. Ponta Delgada, Azores, 2015.

[104] Short, T. A. *Electric power distribution handbook*. Electric power engineering series. Boca Raton, FL: CRC Press, 2004.

[105] Skogestad, S. and Postlethwaite, I. *Multivariable feedback control*. Chichester: John Wiley & Sons, 2001.

[106] Smith, R. C. *Uncertainty quantification: Theory, implementation, and applications*. Vol. 12. Computational science & engineering. Philadelphia, Pa.: Soc. for Industrial and Applied Mathematics, 2014.

[107] Soize, C. *Uncertainty quantification: An accelerated course with advanced applications in computational engineering*. Vol. Volume 47. Interdisciplinary applied mathematics. Cham: Springer, 2017.

[108] Tamm, C. et al. *Methodisches Vorgehen zur Auslegung des vibro-akustischen Verhaltens eines Fahrzeugs*. In: *Smarte Strukturen und Systeme*. Ed. by Wiedemann, M., Misol, M., and Melz, T. Berlin, Boston: De Gruyter Oldenbourg, 2016, pp. 95–106.

[109] Teuffel, P. *Entwerfen adaptiver Strukturen*. Dissertaion. Stuttgart: Universität Stuttgart, 2004.

[110] Thomaier, M. *Optimierung der NVH-Eigenschaften von Pkw-Fahrwerkstrukturen mittels Active-Vibration-Control*. Dissertation. Darmstadt: Technische Universität Darmstadt, 16.06.2008.

[111] Trucano, T. G. et al. *Calibration, validation, and sensitivity analysis: What's what*. In: *Reliability Engineering & System Safety* 91.10-11 (2006), pp. 1331–1357.

[112] Unger, A. *Serientaugliche quadratisch optimale Regelung für semiaktive Pkw-Fahrwerke*. 1st ed. Vol. v.66. Audi Dissertationsreihe. Göttingen: Cuvillier Verlag, 2012.

[113] van Buren, K. L. et al. *Simulating the dynamics of wind turbine blades: Part II, model validation and uncertainty quantification*. In: *Wind Energy* 16.5 (2013), pp. 741–758.

[114] VDI Verein Deutscher Ingenieure. *Aktive Schwingungsisolierung: Active vibration isolation*. Berlin, 2010.

[115] Visioli, A. *Practical PID Control*. Advances in Industrial Control. London: Springer and Springer-Verlag London Limited, 2006.

[116] Wang, X., Lin, S., and Wang, S. *Dynamic Friction Parameter Identification Method with LuGre Model for Direct-Drive Rotary Torque Motor*. In: *Mathematical Problems in Engineering* 2016 (2016), pp. 1–8.

[117] Wenjing, Z. *Parameter Identification of LuGre Friction Model in Servo System Based on Improved Particle Swarm Optimization Algorithm*. In: (2007), pp. 135–139.

[118] Worden, K. and Hensman, J. J. *Parameter estimation and model selection for a class of hysteretic systems using Bayesian inference*. In: *Mechanical Systems and Signal Processing* 32 (2012), pp. 153–169.

[119] Wu, N. and Wang, Q. *An experimental study on the repair of a notched beam subjected to dynamic loading with piezoelectric patches*. In: *Smart Materials and Structures* 20.11 (2011), p. 115023.

[120] Ziegler, J. G. and Nichols, N. B. *Optimum Settings for Automatic Controllers*. In: *Transactions of the ASME* (1942), pp. 759–768.

List of Figures

List of Tables

Nomenclature

Acronyms

A/D	analog-digital conversion
AC	alternating current
ANOVA	analysis of variance
D/A	digital-analog conversion
DC	direct current
DOE	design of experiments
IC	integrated circuit
LQR	linear-quadratic regulator
LuGre	Lund-Grenoble
MAFDS	Modular Active Spring Damper System
MC	Monte Carlo
MCMC	Markov Chain Monte Carlo
MOSFET	metal-oxide-semiconductor field-effect transistor
PCB	printed circuit board
PID	proportional–integral–derivative controller
PWM	pulse width modulation
QoI	quantity of interest
SAM	Research group System Reliability, Adaptive Structures, and Machine Acoustics SAM
SFB	Sonderforschungsbereich (Collaborative Research Center)
SHC	Structural health control
SSE	sum of squares error
SST	sum of squares total
sts	steady state
TU	Technische Universität
UTM	universal testing machine

Latin Letters

A	cross-section area in m^2
A_{core}	core cross-section area in m^2
A_{gap}	gap cross-section area in m^2
$\boldsymbol{A}$	state space system matrix
a	contact point of beam and guidance element in m
B	magnetic flux density in T
B_{core}	core magnetic flux density in T
B_{gap}	gap magnetic flux density in T
B_{sat}	saturated magnetic flux density in T
$\boldsymbol{B}_{\mathrm{a}}$	state space control input matrix
$\boldsymbol{B}_{\mathrm{a,0}}$	control input matrix
b_{L}	left support damping coefficient in Ns/m
b_{R}	right support damping coefficient in Ns/m
b_{S}	spring-damper damping coefficient in Ns/m
$\boldsymbol{b}_{\mathrm{ext}}$	state space excitation input vector
$\boldsymbol{b}_{\mathrm{ext,0}}$	excitation input vector
$\boldsymbol{C}$	state space output matrix
$\boldsymbol{C}_{\mathrm{red}}$	reduced output matrix
$\boldsymbol{D}$	damping matrix
$E_{\mathrm{n}}()$	error function
e_{I}	control deviation for control strategy I in m
e_{II}	control deviation for control strategy II in N/N
F	excitation force in N
$\widehat{F}$	step excitation force in N
F_{a}	brake force in N
$F_{\mathrm{b,L}}$	left support damping force in N
$F_{\mathrm{b,R}}$	right support damping force in N
$F_{\mathrm{b,S}}$	damping force in N
F_{δ}	dissipative force in N
F_{f}	friction force in N
$F_{\mathrm{ge,L}}$	left guidance element force in N
$F_{\mathrm{ge,R}}$	right guidance element force in N
$F_{\mathrm{k_{ge},L}}$	left guidance element elastic deformation force in N
$F_{\mathrm{k_{ge},R}}$	right guidance element elastic deformation force in N
$F_{\mathrm{k,L}}$	left support elasitc force in N
$F_{\mathrm{k,R}}$	right support elasitc force in N
$F_{\mathrm{k,S}}$	elastic force in N
F_{L}	left support reaction force in N

F_μ	friction induced force in N
F_R	right support reaction force in N
F_S	spring-damping force in N
$\boldsymbol{F}$	force vector
f	sampling frequency in Hz
H	magnetic field strength in A/m
H_core	core magnetic field strength in A/m
H_gap	gap magnetic field strength in A/m
I	current in A
J	cost functional
$\boldsymbol{K}$	stiffness matrix
$\boldsymbol{K}_\mathrm{c}$	control matrix
$\boldsymbol{K}_\mathrm{LQR}$	LQR control matrix
$\boldsymbol{K}_\mathrm{D}$	PID derivative gain
$\boldsymbol{K}_\mathrm{I}$	PID integral gain
$\boldsymbol{K}_\mathrm{P}$	PID proportional gain
k_ge	guidance element stiffness in N/m
k_L	left support stiffness coefficient in N/m
k_R	right support stiffness coefficient in N/m
k_S	spring-damper stiffness coefficient in N/m
L	left support
$L()$	likelyhood function
L	number of factor levels
L_c	coil inductance in H
l_B	length of the beam in m
l_c	coil length in m
l_core	magnetic field path in core material in m
l_gap	magnetic field path in air gap in m
l_kin	length of a guidance element arm in m
l_mag	closed magnetic field path in m
M	number of MARKOV CHAIN elements
$M_\mathrm{f,L}$	left friction moment in Nm
$M_\mathrm{f,R}$	right friction moment in Nm
$\boldsymbol{M}$	mass matrix
m	index of MARKOV CHAIN elements
m_A	mass in kg
m_B	beam mass in kg
N	number of measurements
N_c	coil windings

n	index of measurements
P	number of parameters
$P(\,)$	propability distribution
p	index of parameters
q	LuGre-model state variable in m
$Q_{2.5}$	2.5% quantile
$Q_{97.5}$	97.5% quantile
$\boldsymbol{Q}$	state weighting matrix
R	right support
R^2	coefficient of determination
R^2_θ	coefficient of determination of parameter θ
R_{95}	95% interpercentile range
R_c	coil resistance in Ω
$\boldsymbol{R}$	control weighting matrix
r_brake	average brake disc radius in m
r_c	average coil radius in m
$\boldsymbol{r}$	displacement vector
$\boldsymbol{S}_\mathrm{c}$	clipping control law
t	time in s
$u^*_\mathrm{a,L}$	left potential control input voltage in V
$u^*_\mathrm{a,R}$	right potential control input voltage in V
u_α	sample from uniform distribution
$u_\mathrm{a,L}$	left control input voltage in V
$u_\mathrm{a,R}$	right control input voltage in V
$u_\mathrm{in,L}$	left amplified input voltage in V
$u_\mathrm{in,R}$	right amplified input voltage in V
$\boldsymbol{u}$	state space input vector
$\boldsymbol{u}_\mathrm{a}$	control input voltage vector
V	volume in m^3
V_core	core volume in m^3
V_gap	gap volume in m^3
v_0	velocity in m/s
v_S	Stribeck velocity in m/s
W_ge	work done by the guidance elements in J
X	random variable
X_p	control parameter
$\boldsymbol{X}_n$	control parameter input vector
x	x-direction
$\boldsymbol{x}$	state space state vector

$Y()$	function output
$Y^{\mathrm{E}}()$	experimental output
$Y_{\mathrm{I}}()$	comparative feature for case I
$Y_{\mathrm{I}}^{\mathrm{E}}()$	comparative feature for case I obtained from experiments
$Y_{\mathrm{II}}()$	comparative feature for case II
$Y_{\mathrm{II}}^{\mathrm{E}}()$	comparative feature for case II obtained from experiments
$Y_{\mathrm{II}}^{\mathrm{M}}()$	comparative feature for case II obtained from model output
$Y_{\mathrm{I}}^{\mathrm{M}}()$	comparative feature for case I obtained from model output
$Y^{\mathrm{M}}()$	model output
$\overline{Y}^{\mathrm{M}}$	model output mean value
$\widehat{Y}_{\theta}^{\mathrm{M}}$	model output mean value for parameter θ
y	y-direction
$\boldsymbol{y}$	state space output vector
$\boldsymbol{y}_{\mathrm{dis}}$	displacement output vector
$\boldsymbol{y}_{\mathrm{meas}}$	measured output vector
z	z-direction
z_{A}	displacement of mass m_{A} in z-direction in m
z_{α}	transformed guidance element displacement in z-direction in m
z_{B}	displacement of mass m_{B} in z-direction in m
$z_{\Delta \mathrm{ge,0}}$	initial relative displacement in z-direction in m
$z_{\Delta \mathrm{ge,L}}$	left relative displacement in z-direction in m
$z_{\Delta \mathrm{ge,R}}$	right relative displacement in z-direction in m
$z_{\Delta \mathrm{L}}$	left support relative displacement in z-direction in m
$z_{\Delta \mathrm{R}}$	right support relative displacement in z-direction in m
$z_{\mathrm{ge,L}}$	displacement of the beam at the left guidance element connection points in z-direction in m
$z_{\mathrm{ge,R}}$	displacement of the beam at the right guidance element connection points in z-direction in m
z_{L}	displacement of the left support in z-direction in m
z_{R}	displacement of the right support in z-direction in m

Greek Letters

α	angle of guidance elements in ∘
$\varepsilon()$	measurement error
γ	angle of adjustable support lever in ∘
κ	support reaction force ratio in N/N
μ	magnetic permeability in H/m
μ_0	magnetic permeability of free space in H/m

μ_{core}	magnetic permeability of core material in H/m
μ_{d}	LuGre-model dynamic friction coefficient
$\mu()$	LuGre-model state dependent friction coefficient
μ_{s}	LuGre-model static friction coefficient
Φ	magnetic flux in Wb
φ	rotation / angle of the beam in ∘
Φ_{core}	core magnetic flux in Wb
Φ_{gap}	gap magnetic flux in Wb
Σ	mode
σ	standard deviation of the measurement error
σ_0	LuGre-model bristle stiffness in 1/m
σ_1	LuGre-model bristle damping in s/m
σ_2	LuGre-model viscous damping in s/m
$\boldsymbol{\theta}_{\text{M}}$	posterior parameter vector samples
Θ	magnetomotive force in A
Θ_{B}	moment of inertia of the beam in kg·m^2
θ	uncertain parameter
$\Delta\theta$	proposal distribution variance
$\boldsymbol{\theta}$	uncertain parameter vector
$\boldsymbol{\theta}^*$	Markov Chain proposed parameter vector
$\boldsymbol{\theta}_0$	Markov Chain start point for uncertain parameter vector

Other mathematical symbols

$\mathcal{N}()$	normal probability density fuction
$\mathcal{U}()$	uniform probability density fuction
$\mathbf{0}$	zero matrix
$\boldsymbol{I}$	identity matrix
$\dot{()}$	first derivative with respect to time ($= \frac{d}{dt}$)
$\ddot{()}$	second derivative with respect to time ($= \frac{d^2}{dt^2}$)
$()^{\text{T}}$	transposed vector or matrix